Structure of Many-Body Quantum Dynamics: Full Counting Statistics, Fragmentation and Integrability

Riccardo Senese
Mansfield College
University of Oxford

A thesis submitted for the degree of
Doctor of Philosophy in Theoretical Physics
Trinity 2025

Abstract

This thesis investigates the dynamics of quantum many-body systems in isolation, in three different setups.

We start by considering a paradigmatic quantum chaotic model of magnetism, the Heisenberg antiferromagnet in 2 and 3 spatial dimensions. The focus is on obtaining approximations for the full counting statistics (FCS) of a subsystem order parameter, the staggered magnetization, both in and out of equilibrium (following quantum quenches). We employ mappings of spin variables to bosonic ones, together with self-consistent time-dependent mean-field schemes, to compute the FCS via Gaussian techniques. In particular, we introduce a formula for the FCS of any subsystem observable that is at most quadratic in the bosons. We obtain results both in the presence and absence of long-range magnetic order.

We then turn to the first of two ergodicity-breaking scenarios, by considering Hilbert space fragmentation (HSF) in charge- and dipole-conserving quantum chains. We determine the critical charge density at which a "freezing" phase transition from weak to strong fragmentation takes place, for any on-site Hilbert space dimension. To characterize the degree of dynamical connectivity in the system, we introduce a novel framework that enables us to obtain analytic results for the strongly fragmented phase, and numerically explore the weakly fragmented one. We derive some critical exponents, and show that the entanglement entropy of typical eigenstates in the strongly fragmented phase obeys an area law. We also uncover the existence of rare eigenstates whose entropy appears to scale beyond any area law.

Finally, we investigate dynamical correlators in the Lieb-Liniger gas, one of the simplest interacting integrable theories solvable by Bethe ansatz. We employ Markov chain Monte Carlo methods to sample matrix elements (form factors) that appear in the Lehmann representation of the finite-temperature single-particle bosonic Green's function. In the physical regimes we consider, sampling is necessary because a full summation of the relevant form factors is computationally intractable. We benchmark our results against exact solutions available in specific limits, and find them to be very accurate.

Acknowledgements

I would like to thank my supervisor, Fabian Essler, for his inspiring enthusiasm, dedication, and constant availability for discussion. I have learned a great deal from trying to replicate his approach to physics.

This thesis has benefited enormously from the help of my collaborators and fellow physicists. First and foremost, I wish to thank Jonathan and Jacob, with whom I spent countless hours grappling with the challenges of daily research. Many thanks to Abhi for his many valuable insights and his kindness, and to Luisa and Saraswat for our chats in the office. I am grateful to Alessio Lerose, Sascha Gehrmann, John Chalker, Lev Vidmar and Curt von Keyserlingk for stimulating discussions. I would also like to thank my examiners, Steve Simon and Bruno Bertini, for their insightful comments, which helped to improve this thesis.

My years in Oxford were made truly memorable by a few people I was lucky enough to meet, and I owe a huge debt of gratitude to all of them. To Disha and Gregorio (della Pizza), for the countless moments of pure fun; when I think of Oxford, you are the first image that comes to mind. To my other "8 Western siblings" – Fien, Liam, Ludo, and Noelia – for surviving our kitchen together, and for the many game and movie nights. To Ale, for being "un fratello", and for always teaching me something, from music to plasma physics. To Chris, Amir, Shanthi, Imogen, Gavin, Ada, Caroline, Nikhil, Ghita, Arnaud, Ryan, Eylül, Gala, Arunima, Thizi, Julian, Meghana, Caroline, and Lucas, for the wonderful memories over the years. To Bianca, Carlo, Stefano and Giuliano, because Italian vibes are important in life.

I also wish to extend my heartfelt thanks to my friends back home. To Dibbi, Bizzi, Mat, Sofi, Virgi, Cecia and Giuli, for always making me feel that little has changed, despite the distance. To my undergraduate team – Sciottolo, Gio, Drago, Ali, Ems, Cla, Barbavita, Rob, Jacopo and Spelvio – for the fun and many memorable trips together.

I sincerely thank my family for their unwavering support throughout my life. In particular, I thank my parents for the freedom they have always granted me and for encouraging me to follow my passions, wherever they might lead.

Finally, I would like to thank Ceci, aka Limone9, for constantly filling me with unconditional happiness.

Publications

This thesis is based on the following three works:

- R. Senese, J.H. Robertson, F.H.L. Essler, *Out-of-equilibrium full counting statistics in Gaussian theories of quantum magnets.*
  SciPost Phys. 17, 139 (2024).
- J. Classen-Howes*, R. Senese*, A. Prakash, *Universal freezing transitions of dipole-conserving chains.*
  Phys. Rev. B 112, 125148 (2025).
- R. Senese, F.H.L. Essler, *Finite temperature single-particle Green's function in the Lieb-Liniger model.*
  arXiv:2508.17908 (2025).

During my DPhil, I also worked on other related topics:

- J.H. Robertson, R. Senese, F.H.L. Essler, *A simple theory for quantum quenches in the ANNNI model.*
  SciPost Phys. 15, 032 (2023).
- J.H. Robertson, R. Senese, F.H.L. Essler, *Decay of long-lived oscillations after quantum quenches in gapped interacting quantum systems.*
  Phys. Rev. A 109, 032208 (2024).

Authors marked by * contributed equally.

Contents

Appendices

1

Introduction

The world around us is made up of an astonishingly high number[1] of elementary particles that arrange themselves into atoms, which in turn give rise to all the different phases of matter. The physical laws that govern the behaviour of these elementary constituents are those of quantum mechanics, and this entails many odd facts that easily defy our intuition. The majority of natural phenomena one might classify as "interesting" ultimately emerge from the complex quantum dynamics induced by the interactions between these very many constituents. Unfortunately, despite the goal of theoretical physics being to predict, or simulate, these phenomena, their underlying mathematical description generally results in tasks that possess an exponential complexity of some sort. But not everything is lost, for at least three (related) reasons: (i) we are usually not interested in capturing all the details of a physical process; (ii) the very large number of elementary constituents involved can, counter-intuitively, lead to significant simplifications of the problem; (iii) approximate descriptions might suffice to capture the essence of a given phenomenon.

This thesis presents progress on different methods to describe dynamics in simple models[2] of many interacting quantum-mechanical degrees of freedom. Most of the

---

[1] One might think of an order of 10^{28}–10^{30}, in their immediate surroundings.

[2] These models are stripped of the usual complexity of real-world scenarios, and retain only what we believe to be crucial ingredients to describe the emergence of important physical properties from the interactions between the elementary quantum constituents.

focus will not be on the experimental or technological applicability of the findings, but on the possibility of learning general features of the (mathematical) structure behind quantum dynamics, in different contexts [1–3].

1.1 Quantum dynamics

In the past few decades, several advances in experimental platforms that enable the control of quantum degrees of freedom and the simulation of their dynamics [4–12] have sparked significant interest in the theoretical description of quantum time evolution in many-body systems. The essence of quantum dynamics within an isolated system is fully encoded in the time-dependent Schrödinger equation

$$\frac{d}{dt}\left|\psi(t)\right\rangle = H\left|\psi(t)\right\rangle \qquad \longrightarrow \qquad \left|\psi(t)\right\rangle = e^{-iHt}\left|\psi(0)\right\rangle \ , \tag{1.1}$$

where $|\psi(t)\rangle$ is a normalized time-dependent quantum state[3] and H denotes the Hamiltonian governing the dynamics of the system [13]. One is usually interested in the time evolution of the expectation value of some physical observable O (a Hermitian operator) in the state $|\psi(t)\rangle$

$$\langle\psi(t)|O|\psi(t)\rangle \ , \tag{1.2}$$

or of some of its higher moments $O^2, O^3, \ldots$. Given that the Hamiltonian is itself Hermitian, there exists a complete orthonormal basis of the global Hilbert space which is composed of eigenstates $|n\rangle$ of H, each associated with an energy eigenvalue E_n. Combining this with Eq. (1.1), we see that (1.2) can be expressed via the following Lehmann representation

$$\langle\psi(t)|O|\psi(t)\rangle = \sum_{m,n} e^{it(E_m-E_n)}\left\langle\psi(0)|m\right\rangle\left\langle m|O|n\right\rangle\left\langle n|\psi(0)\right\rangle \ , \tag{1.3}$$

where we have made use twice of the resolution of the identity $\sum_n |n\rangle\langle n| = 1$. The theoretical and experimental protocol for which one considers or prepares some simple (i.e. weakly entangled) state $|\psi(0)\rangle$ and then lets it time evolve according to a Hamiltonian H, whose action is suddenly switched on at time $t = 0$, goes under

---

[3] That is, a vector of unit norm in some (separable) Hilbert space.

the name of *quantum quench* [14, 15]. The requirement of $|\psi(0)\rangle$ being simple stems from our desire to understand how complex quantum correlations, for example defined by some entanglement measure [16], arise over time as a consequence of the unitary evolution (1.1), and hence we want to exclude their presence in the initial state[4]. Often, $|\psi(0)\rangle$ is chosen to be the ground state[5] of a different "pre-quench" Hamiltonian H_0. In the following, we will only be concerned with quantum systems of extended size, e.g. occupying a large volume V of space, that possess a finite density N/V of interacting degrees of freedom, as required to model real-world scenarios. This implies that in the limit of large V the subregion of the spectrum relevant for dynamical observables like (1.3) lies at a finite energy *density* above the ground state of H. Indeed, one generally has

$$\langle\psi(0)|H|\psi(0)\rangle - E_{\mathrm{GS}} \propto V \ , \tag{1.4}$$

$$\frac{\sqrt{\langle\psi(0)|H^2|\psi(0)\rangle - \langle\psi(0)|H|\psi(0)\rangle^2}}{\langle\psi(0)|H|\psi(0)\rangle} = o(V^0) \ . \tag{1.5}$$

The first equation states that the average energy in the system after a quantum quench is extensively larger than the ground state energy of H. The second equation, which can be derived on very general grounds only by invoking the cluster decomposition principle [18], states that fluctuations around this average are subextensive [19]. This helps us contextualize the intrinsic complexity behind unitary time evolution in extended systems: there is an exponentially large (in volume V) number of eigenstates that meaningfully contribute to (1.3), and these all lie very far away from the ground state sector, in a region of the spectrum where even the approximate determination of an eigenstate $|n\rangle$ is itself an exponentially hard problem, due to the volume-law entanglement that typically characterizes such states (see, e.g., [19–22], or Section 1.2). Given our interest in the dynamics of physical observables, it is often standard practice to work in the Heisenberg picture [13]

$$O(t) = e^{iHt} O e^{-iHt} \ . \tag{1.6}$$

---

[4] Requiring $|\psi(0)\rangle$ to be simple also generally guarantees a nonzero overlap $\langle\psi(0)|m\rangle$ with exponentially many (in the size of the system) eigenstates, in turn implying nontrivial dynamics.

[5] Ground states of Hamiltonians with local densities are, in fact, characterized by a low degree of entanglement [17].

While quantum quenches describe proper *out-of-equilibrium* protocols, in this thesis we will also be concerned with dynamical properties in *equilibrium*, that is, within the framework of quantum statistical mechanics [23]. In particular, we will consider the following type of dynamical correlation functions

$$\mathrm{Tr}[\rho\, O(t)\, O] = \sum_{m,n} e^{it(E_m - E_n)}\, \rho_m \,|\, \langle m|O|n\rangle \,|^2 \ , \tag{1.7}$$

where ρ denotes the density matrix associated with a thermodynamic ensemble, e.g. the microcanonical or canonical ones[6] [23]. On the right-hand side of (1.7) we have reported the associated Lehmann representation, where, due to the fact that ρ is diagonal in the eigenstates of H, the thermal weight ρ_m coincides simply with the eigenvalue of ρ for $|m\rangle$. Unlike (1.2), correlators of the form of (1.7) are not associated with experimental quantities directly obtainable by projective measurements of the observable O. However, they are the primary objects entering Kubo's linear response theory [26, 27], and hence can be easily related to measurements performed on systems in equilibrium after they have been weakly perturbed. Whenever ρ is associated with a finite temperature (in the language of the canonical ensemble), the weights ρ_m and the density of states along the spectrum imply that only a subextensive subregion in energy space, which is extensively far from the ground state, meaningfully contributes to (1.7), similarly to what happens in the quench case due to Eqs. (1.4) and (1.5). Therefore, the same conclusions as before about the exponential complexity of reconstructing the time evolution apply also here.

1.2 Eigenstate thermalization and quantum chaos

Classical systems of many interacting degrees of freedom are generally chaotic [28, 29]. This means that vanishingly small perturbations in their initial conditions produce very strong effects on their dynamical evolution at later times, the famous

---

[6] In the limit of large volumes V, all thermodynamic ensembles are equivalent from the point of view of characterizing local properties of physical observables, including those time evolved in the Heisenberg picture (which, even if not clear a priori, retain a strong degree of locality [24, 25]).

"butterfly effect". Chaotic systems are also typically ergodic[7], i.e. they explore all the phase space available over sufficiently long periods of time. In quantum systems, there is no analogue of the butterfly effect at the level of the time-evolving state $|\psi(t)\rangle$, for the very simple reason that Schrödinger equation (1.1) is linear[8] in $|\psi(t)\rangle$. Therefore, defining quantum chaos [30] by simple generalizations of concepts from classical chaos theory is not in general possible.

Building on the work of Wigner [31, 32] and Dyson [33], it was eventually realized [34–38] that quantum chaos can be defined on the basis of similarities between the energy-level statistics in the spectra of quantum systems with classically chaotic counterparts and those of large random matrices [39]. Importantly, this definition naturally extends to systems without a classical counterpart, and has been generalized to other spectral probes. These include the eigenstate delocalization in a given basis [19, 40, 41], entanglement entropy [42–44], and, famously, the scaling and statistics of matrix elements, described by the *eigenstate thermalization hypothesis* (ETH). Pioneered by early works of Deutsch [45] and Srednicki [46], ETH is a conjecture on the structure of matrix elements $\langle m|O|n\rangle$ of a physical (e.g. local) observable O in the basis of eigenstates of an interacting quantum-chaotic Hamiltonian. These are the same type of matrix elements entering Eqs. (1.3) and (1.7). For a Hamiltonian H without a block diagonal structure (no symmetries), the ETH ansatz states that $\langle m|O|n\rangle$ has the following universal form [19, 47, 48]

$$\langle m|O|n\rangle = O(\bar{e})\delta_{m,n} + e^{-S(\bar{e}V)/2} f_O(\bar{e},\omega) R_{mn} \ , \tag{1.8}$$

where $\bar{e} = (E_m + E_n)/(2V)$ is the mean energy density, $\omega = E_m - E_n$, $S(E)$ is the thermodynamic entropy at energy E, and R_{mn} are complex numbers that vary erratically with m and n, and it can be helpful to think of them as random variables with zero mean and unit variance[9]. Crucially, $O(e)$ and $f_O(e,\omega)$ are smooth

---

[7] And mixing, a closely related but different concept.

[8] This implies that the state $|\tilde{\psi}(t)\rangle = e^{-iHt}(|\psi\rangle + \epsilon\,|\phi\rangle)$, where ϵ is small and $|\psi\rangle$ and $|\phi\rangle$ are arbitrary states, remains close to $|\psi(t)\rangle = e^{-iHt}\,|\psi\rangle$ at all times.

[9] The variance is 1 for off-diagonal matrix elements, i.e. for $m \neq n$, while it can be higher but still $\mathcal{O}(V^0)$ for the diagonal elements ($m = n$). For example, R_{mm} has variance 2 in the Gaussian orthogonal ensemble of random matrix theory.

functions of their arguments. ETH provides a remarkably simple explanation for how isolated quantum systems locally thermalize [47, 49] (see also the reviews [19, 50–53]). To see this, it is convenient to start by considering infinite-time averages of the time-dependent expectation value (1.2)

$$\overline{C} = \lim_{t^*\to\infty} \frac{1}{t^*}\int_0^{t^*} dt\, C(t) \qquad\qquad C(t) = \langle\psi(t)|O|\psi(t)\rangle \ . \tag{1.9}$$

From (1.3) we obtain

$$\overline{C} = \sum_m |\,\langle\psi(0)|m\rangle\,|^2\,\langle m|O|m\rangle = O(e) + o(V^0) \ , \tag{1.10}$$

where $O(e)$ is the smooth function entering the diagonal ETH and e is equal to $\langle\psi(0)|H|\psi(0)\rangle/V$, *cf.* Eq. (1.4). To obtain the first equality in (1.10) we have assumed a nondegenerate spectrum, which is reasonable given the absence of symmetries of H. The second equality follows, in the limit of large V, from the use of Eq. (1.5) together with the ETH ansatz (1.8) and $\sum_m |\,\langle\psi(0)|m\rangle\,|^2 = 1$. Given that $O(e)$ is a smooth function of the energy density, it is easy to see from the structure of (1.8) that, for large system sizes, $O(e)$ also coincides with the thermal expectation value of the observable O at energy density e. Employing the canonical ensemble, this means that

$$\lim_{V\to\infty}\overline{C} = \lim_{V\to\infty}\frac{1}{Z_\beta}\mathrm{Tr}[e^{-\beta H}O] \ , \tag{1.11}$$

where β is the inverse temperature that fixes an average energy density of e. The remarkable prediction of Eqs. (1.10) and (1.11) is that, for large V, the infinite-time average of $C(t)$ equals the thermal expectation value of O, *irrespective* of the details of the initial state $|\psi(0)\rangle$. In other words, expectation values of physical observables after quantum quenches thermalize at late times, and the system loses any local memory of its initial state[10]. It is also elementary to prove that the infinite-time average of the instantaneous deviations of $C(t)$ from $\overline{C}$ are exponentially suppressed in V

$$\lim_{t^*\to\infty}\frac{1}{t^*}\int_0^{t^*} dt\,(C(t)-\overline{C})^2 \propto \exp(-aV) \qquad\quad a>0 \ . \tag{1.12}$$

---

[10] Aside, possibly, for the one relative to the conserved energy density.

This is a consequence of the off-diagonal ETH in (1.8) [47]. The previous equation suggests that the use of infinite-time averages, which makes the statements above precise at any finite V, is not necessary in the thermodynamic limit. Indeed, in infinitely large systems expectation values like $C(t)$ *relax* to a stationary value at late times. This is expected on very general grounds as a consequence of the dephasing over time of the infinitely many (for $V \to \infty$) off-diagonal phases in (1.3), which is sufficient to argue that the finite-time deviations of $C(t)$ from its asymptotic value decay to zero at least polynomially with t. Therefore, it is generally expected that the statement (1.11) can be replaced by one that involves no averaging[11] [50]

$$\lim_{t\to\infty}\lim_{V\to\infty} C(t) = \lim_{V\to\infty}\frac{1}{Z_\beta}\mathrm{Tr}[e^{-\beta H}O] \ . \tag{1.13}$$

Note that the order of limits is crucial to ensure that the $t \to \infty$ limit exists.

Another feature of the eigenstate thermalization phenomenon is related to the entanglement entropy (EE) of single eigenstates. Consider a system that is in a pure state $\rho = |\psi\rangle\langle\psi|$, and imagine bipartitioning it into a subsystem A and its complement B. The von Neumann EE S_{vN} associated with this spatial bipartition is defined as [16]

$$S_{\mathrm{vN}} = -\mathrm{Tr}_A(\rho_A \ln \rho_A) \qquad\qquad \rho_A = \mathrm{Tr}_B(\rho) \ . \tag{1.14}$$

Here Tr_A denotes a partial trace over the degrees of freedom in A (and analogously for B). S_{vN} represents a meaningful measure of entanglement in $|\psi\rangle$, and is said to follow a volume-law scaling if $S_{\mathrm{vN}} \propto |A|$, where $|A|$ is the volume of A. If we identify $|\psi\rangle$ with an eigenstate of a quantum chaotic model at finite energy density e (above the ground state), then $S_{\mathrm{vN}}/|A|$ coincides, up to finite-size corrections, with the thermodynamic entropy density $s(e) = \lim_{V\to\infty} S(eV)/V$ [19–22, 42–44, 54, 55]. This means that eigenstates of quantum chaotic models away from the ground state sector possess volume-law EE, i.e. $S_{\mathrm{vN}} \propto V$ for any extensive subsystem A, and hence they are highly complex quantum states. The phenomenon of thermalization after quantum quenches, summarized at the level of expectation values by (1.13),

---

[11] We stress that, mathematically, Eq. (1.13) does not directly follow from ETH, due to the order of limits on the left-hand side.

has a counterpart at the level of EE. Indeed, if we initialize a system in a state $|\psi(0)\rangle$ with zero or very low EE, and let it time evolve as in Eq. (1.1), its EE S_{vN} (associated with a subsystem A) grows linearly with time, i.e. $S_{\mathrm{vN}} \propto t$, until it saturates at the thermal value $s(e)|A|$ [14, 56–65]. This, together with (1.13), suggests that at late times the pure state $|\psi(t)\rangle$ becomes *locally* indistinguishable from a thermal ensemble as a consequence of the build-up over time of complex quantum correlations between its subparts. The ballistic growth of entanglement $S_{\mathrm{vN}} \propto t$ is the major source of limitations in the attempt to classically simulate unitary evolution up to late times, e.g. via numerical tensor network methods [66–68].

If H possesses a few symmetries, the ETH ansatz applies only within its irreducible symmetry sectors. Indeed, if symmetries are not resolved, standard indicators of quantum chaos like energy-level statistics fail to distinguish ergodicity-breaking systems (see Section 1.3) from quantum-chaotic ones [41]. The structure of ETH has also been found to depend on the type of symmetries present, and in particular on their degree of locality, see e.g. [69] and references therein. For example, in lattice systems discrete symmetries like lattice translation, which are nonlocal, can give rise to identical diagonal matrix elements even in different sectors, while this is not expected to be the case in the presence of $U(1)$ symmetries associated with local conserved charges[12]. The need to resolve symmetry sectors is even more apparent for off-diagonal matrix elements, which vanish if the observable O does not break the symmetries of H. Very recently, due to growing interest in fundamental questions regarding the nature of thermal equilibrium in systems with non-commuting charges [70–72], the ETH ansatz has been generalized to account for the presence of non-Abelian symmetries [73–76]. Furthermore, ETH has been extended to address higher-order correlations between matrix elements, yielding a “full ETH” ansatz [77–81]. These correlations are closely related to known features of higher-point dynamical functions of observables.

---

[12] In such cases, the diagonal matrix elements entering the ETH ansatz are expected to feature a smooth dependence, in addition to the one on the energy density, on the intensive values of the charge in each sector.

In Chapter 2 we will be concerned with the equilibrium and out-of-equilibrium properties of some specific quantum chaotic models. We will introduce an approximate method to calculate *every* moment of a subsystem observable O, i.e. $\langle O^r \rangle$ for $r = 1, 2, \ldots$, where $\langle \cdot \rangle$ indicates either thermal average or average in a quantum state that is evolving after a quantum quench, like in Eq. (1.2). Knowledge of all these moments is equivalent to determining (approximately within our method) the full probability distribution of the outcomes of projective measurements of O in the system's quantum state.

1.3 Quantum ergodicity breaking

Not all quantum many-body systems are chaotic, in the sense defined in the previous section. Violations of ETH and other indicators of quantum chaos are usually associated with the existence of a high number of symmetries of H, which strongly constrain dynamics and can significantly reduce the quantum complexity of eigenstates. In Chapters 3 and 4 we will be concerned with two different mechanisms for quantum ergodicity breaking: *Hilbert space fragmentation* and *integrability*. We briefly introduce them here, and highlight some major differences compared to features seen in the previous section. Further details on these two phenomena will be discussed in their respective chapters.

It is worth mentioning that there are other very well-known mechanisms for ergodicity breaking in a quantum many-body setup, most notably many-body localization (MBL) [82, 83] and quantum many-body scars (QMBS) [84–87]. In MBL systems, the combination of strong disorder and interactions leads to the emergence of integrals of motion (symmetries) with a highly local nature, which in turn imply the existence of localized[13] eigenstates throughout the spectrum. MBL represents a robust mechanism for strong ergodicity breaking (e.g. full violation of ETH), in that it does not rely on fine-tuning of the model. However, its stability in the limit of large system sizes V has still not been properly established[14] [90–92].

---

[13] Here "localized" means that when an eigenstate is expanded in a simple computational basis, only a small fraction of the basis states contribute to it.

[14] See, however, [88, 89] for progress in this direction.

QMBS represent rare ETH-violating[15] eigenstates in the spectrum of otherwise chaotic Hamiltonians. Hence, systems hosting QMBS feature only a very weak violation of quantum-ergodic behaviour, given that QMBS represent a measure-zero set of all eigenstates (for $V \to \infty$). Quantum scarring is not robust to generic perturbations, i.e. it is a fine-tuned phenomenon, and can be understood as a consequence of the Hamiltonian acquiring an approximate or exact block diagonal structure (not emerging from any conventional symmetry) which separates the sector where QMBS live from the rest of the spectrum [84].

1.3.1 Integrability

A classical Hamiltonian H_c with a $2n$-dimensional phase space is Liouville-integrable if there exist n independent quantities $Q_c^{(i)}$, $i = 1, \dots, n$, such that

$$\{H_c, Q_c^{(i)}\} = 0 \qquad \forall\, i \qquad\qquad \{Q_c^{(i)}, Q_c^{(j)}\} = 0 \qquad \forall\, i, j \ , \tag{1.15}$$

where $\{\cdot\}$ denotes a Poisson bracket. The first of these conditions implies that all the $Q_c^{(i)}$ are integrals of motion for the dynamical system. Therefore, the dynamical exploration of the global phase space available is strongly restricted, for example at a fixed energy. Furthermore, Eq. (1.15) enables one to perform a canonical transformation to action-angle variables that trivially solve the full dynamics. Hence, these systems are said to be classically solvable.

The quantum analogue of classically integrable systems are those governed by a quantum many-body Hamiltonian H that possesses an *extensive* number of Abelian symmetries, i.e. operators $Q^{(i)}$ (with local densities[16]) such that

$$[H, Q^{(i)}] = 0 \qquad \forall\, i \qquad\qquad [Q^{(i)}, Q^{(j)}] = 0 \qquad \forall\, i, j \ . \tag{1.16}$$

Such systems, which usually exist in one spatial dimension, are solvable in the sense that their spectrum and all (simultaneous) eigenstates of H and the other charges can be determined explicitly, via the celebrated Bethe ansatz [93, 94]. In particular,

---

[15] With this we also mean that they exhibit violations of the volume-law EE scaling expected in a chaotic spectrum, which is replaced by an area-law scaling.

[16] This means that the charges $Q^{(i)}$ can be expressed as extensive sums or integrals over operators whose action is (almost entirely) limited to a finite region of space.

the mathematical origin of the symmetries $Q^{(i)}$ is understood within a powerful algebraic framework known as algebraic Bethe ansatz [94, 95]. Importantly, there is a family of charges $Q^{(i)}$ that are ultra-local. This means that they can be expressed, e.g. for lattice models, as extensive sums of operators that have a finite[17] spatial support. Given the existence of an extensive number of conservation laws, it is not surprising that spectral properties of quantum integrable models differ considerably from those that characterize chaotic ones. For example, integrable spectra do not feature level repulsion [19] and the statistics of matrix elements associated with local operators possesses a richer structure than the one associated with ETH, see e.g. [43, 98–100]. For example, the diagonal ETH is modified by the appearance of a smooth dependence on all the intensive charges, and the logarithm of off-diagonal matrix elements can be proportional to V^2 [98], instead of being "merely" extensive as in the ETH case of (1.8). The entanglement entropy of finite-energy-density eigenstates, despite being extensive, features a volume-law coefficient that is smaller [43] than the thermodynamic entropy density that characterizes the volume-law scaling in the chaotic case. At the level of thermalization (after a quantum quench with an integrable Hamiltonian H), Eq. (1.13) is replaced by a local relaxation to a generalized Gibbs ensemble (GGE) [50, 101]

$$\rho_{\text{GGE}} = \frac{e^{-\beta H - \sum_i \gamma_i Q^{(i)}}}{Z_{\beta,\gamma}} \ , \tag{1.17}$$

where the Lagrange multipliers γ_i set the expectation values of the conserved charges equal to those that characterize the initial state $|\psi(0)\rangle$. Integrability is not a robust form of ergodicity breaking, in that generic perturbations to H restore chaos and ETH. For sufficiently weak perturbations, features of integrability can survive on prethermal scales [102, 103]. However, we note that even perturbation strengths exponentially small in V are believed to be sufficient to induce an onset of chaotic behaviour [19, 104–106].

---

[17] Note that in certain physically relevant integrable systems also families of "quasilocal" charges, where the finite support condition is replaced by, e.g., an exponential localization in space, play an important role [96, 97].

In Chapter 4, we will consider dynamical correlation functions like (1.7) in the interacting Lieb-Liniger gas, a paradigm for quantum integrable models. In particular, we will introduce a Monte Carlo method to numerically reconstruct these correlators from their Lehmann representation (1.7). This is possible because in the integrable setup the matrix elements involved are explicitly known. However, given that an exponential number of them (in V) appears in (1.7), a sampling scheme is necessary to accomplish the task.

1.3.2 Hilbert space fragmentation

The Hilbert space $\mathcal{H}$ of any isolated quantum system[18] can be decomposed into decoupled subspaces as

$$\mathcal{H} = \bigoplus_{i=1}^{K} \mathrm{span}_t \{ U(t) \left| \psi_i \right\rangle \} \ , \tag{1.18}$$

where $U(t)$ represents a unitary time evolution (e.g. e^{-iHt} in Hamiltonian systems, like in (1.1), or U^t in quantum circuits with discrete evolution governed by a unitary U [16]) and span_t indicates the span of the vectors $U(t) \left| \psi_i \right\rangle$ for all values of t [107]. The K independent subspaces appearing in (1.18) are known as *Krylov* sectors, and their definition implicitly depends on the choice of the $\left| \psi_i \right\rangle$ states. The decomposition (1.18) is particularly meaningful when $\left| \psi_i \right\rangle$ are chosen to be simple weakly-entangled states[19]. Below, and in Chapter 3, we always mean it in this sense.

Hilbert space fragmentation (HSF) [108, 109] is the phenomenon for which the total number of Krylov sectors K (defined from simple $\left| \psi_i \right\rangle$ states) scales exponentially with the volume V of the system, despite the lack of simple conventional symmetries capable of explaining this behaviour. It is usually a consequence of the fractonic nature [110, 111] of the underlying system described by the unitary $U(t)$, in which elementary excitations possess very restricted mobility as a consequence

---

[18] Here we implicitly assume the Hilbert space to be finite dimensional, which is true in any finite lattice with on-site dimension $d < \infty$. In the case of $d = \infty$, e.g. bosons, one can recover a finite Hilbert space by restricting its attention to specific symmetry sectors, e.g. one with fixed finite number of particles.

[19] Indeed, Eq. (1.18) carries little significance when the states $\left| \psi_i \right\rangle$ are chosen to be, for example, the eigenstates of $U(t)$, in which case $K = \dim \mathcal{H}$.

of the interplay between a few different constraints. HSF significantly differs from quantum chaotic or quantum integrable models in several aspects:

- In general, a decomposition like the one in (1.18) is a consequence of $U(t)$ possessing some symmetries. In quantum chaotic systems these usually give rise to K distinct symmetry sectors, with K growing only polynomially (continuous global symmetries, e.g. U(1)) or being constant (discrete global symmetries, e.g. Z_2) in the volume V. This is in marked contrast with the scaling $K \sim \exp(c\,V)$ that defines HSF.

- In quantum integrable models the extensive number of (quasi)local charges $Q^{(i)}$ of Section 1.3.1 generates exponentially many symmetry sectors. However, this is practically equivalent to a full diagonalization of the Hamiltonian (hence of the unitary $U(t)$), and does not correspond to a decomposition like (1.18) in which simple states $|\psi_i\rangle$ appear[20]. On the contrary, the exponential scaling of K in HSF is a consequence of the existence of highly *non-local* symmetries which, unlike the integrable case, give rise to Krylov sectors featuring a *very wide range* of dimensions (e.g. from 1-dimensional sectors to exponentially large ones). Furthermore, as we discuss below, there exists a large class of arbitrary-strength perturbations that leaves the HSF structure unchanged.

To see how the previous points emerge we can focus on Hamiltonian dynamics, but identical conclusions apply for quantum circuit models. The HSF phenomenon characterizes entire classes $H(\boldsymbol{J})$ of Hamiltonians defined by a set of local operators $\{\hat{h}_i\}$ which have finite support [107]

$$H(\boldsymbol{J}) = \sum_i J_i\, \hat{h}_i \ . \tag{1.19}$$

Indeed, HSF emerges solely from the interplay between the finite-range nature of the interactions $\{\hat{h}_i\}$ and a few simple symmetries that these local terms possess, which together imply strong constraints on the dynamics. Unlike integrability, the

---

[20] As we have seen, finite-energy-density eigenstates of integrable models possess volume-law EE.

couplings J_i can be chosen arbitrarily without altering the fragmented structure[21]. From this point of view, HSF possesses a degree of robustness that integrability lacks. On the other hand, HSF disappears as soon as any of the key features of the set $\{\hat{h}_i\}$ (finite-range support, compatibility with some specific symmetries) fails to be exactly satisfied[22].

In some of the simplest models hosting HSF the non-local symmetries that label the exponentially many Krylov sectors possess a relatively simple form that allows for their explicit construction [107, 112], but the same does not appear to be possible in more general models (including many of those described in Chapter 3). Furthermore, we note that HSF can be more rigorously formalized using the language of commutant algebras [107]. Among other things, this makes it possible to draw a clear distinction between "classical HSF", which arises when all the states $|\psi_i\rangle$ in (1.18) can be chosen from a product-state basis, and "quantum HSF", where the use of some (slightly) entangled states is necessary to uncover the full block-diagonal structure of $H(\boldsymbol{J})$.

In Chapter 3, we will focus only on models that exhibit classical HSF. Due to this, we will see that the same phenomenology of fragmentation characterizes both quantum models with Hamiltonian (1.19) and classical stochastic models in which the dynamics proceeds by application of classical gates[23]. Despite the fact that the algebraic formalism based on the commutant algebra is very useful to rigorously define many features of HSF, it does not yield any advantage in tackling the questions we are concerned with in Chapter 3. To make progress, we will introduce a simple yet powerful framework that allows us to analytically characterize many aspects of fragmentation in the paradigmatic class of models in which HSF has originally been pointed out as a phenomenon [108, 109, 113], i.e. charge- and dipole-conserving chains.

---

[21] We note that for a given H there could be multiple different ways of expanding it in a sum like the one in (1.19). As a consequence, such H inherits the fragmented properties of all families $H(\boldsymbol{J})$, $H'(\boldsymbol{J}'), \ldots$ to which it belongs.

[22] In such cases, signatures of fragmented behaviour can be observed only on prethermal scales.

[23] Which implement the same type of transitions as the $\{\hat{h}_i\}$.

2

Full counting statistics in Gaussian theories of quantum magnets

2.1 Introduction

Central to our understanding of quantum phenomena is the existence of a probability distribution function (PDF) $P_{R,|\psi\rangle}$ associated with the possible outcomes of measuring an observable R in a given quantum state $|\psi\rangle$ [13]. Knowledge of $P_{R,|\psi\rangle}$ is equivalent to that of *all* moments of the observable, i.e. $\langle\psi|R^n|\psi\rangle$, $n = 1, 2, 3, \ldots$. In the realm of quantum many-body physics, quantum mechanical PDFs have appeared in relation to experiments in mesoscopic devices [114, 115], where precise measurements of the temporal fluctuations of electrical currents give access to the charge and statistics of quasiparticles relevant for transport. The interest in quantum PDFs has also been extended to different experimental platforms [116–124], where it is possible to measure the PDFs of various observables defined on subsystems. These experiments motivated theoretical efforts to compute PDFs both in [125–141] and out of [120, 142–157] equilibrium. We note that only very recently the non-equilibrium PDF of extended subsystem observables, addressed in this chapter, has become accessible experimentally [158–160]. In all these theoretical and experimental contexts, the generating functions of moments (or cumulants) associated with quantum PDFs are known as "full counting statistics" (FCS).

Given the difficulties in calculating the FCS for subsystem observables, there are relatively few known results, most of them established for systems in one spatial dimension $D = 1$. In this chapter, we consider FCS of subsystem observables in a paradigmatic model of quantum magnetism[1], the Heisenberg antiferromagnet in dimensions $D = 2$ and 3. We employ a range of representations of quantum spins in terms of canonical boson operators and focus on physical regimes dominated by Gaussian fluctuations of these bosons. This allows us to obtain efficient determinant representations for the FCS of observables of interest, both in and out of equilibrium. The prototypical example of spin systems where representations in terms of bosons and Gaussian approximations can be successfully employed are those possessing long-range magnetic order. Here Gaussian quantum fluctuations are the dominant contribution beyond the classical mean-field solution. We will also see how Gaussian approximations can be employed in absence of long-range magnetic order. As for the observable, we will consider the FCS of the staggered magnetization, an order parameter which is not a globally conserved charge.

The chapter is organized as follows. In Section 2.2 we introduce the PDF of quantum observables, and report a simple formula for the FCS of any observable expressible as at most a quadratic polynomial in bosonic variables, in any Gaussian state of said bosons. We also briefly review mean-field theory methods in and out of equilibrium. We then turn to applications of our FCS formula to extract PDFs in the Heisenberg model both in and out of equilibrium (after quantum quenches). In Section 2.3 we focus on regimes in $D = 2, 3$ that possess long-range magnetic order, and employ spin-wave theory to reduce the problem to the study of Gaussian theories of bosons. In Section 2.4 we turn to disordered phases of magnets and consider the 2D Heisenberg antiferromagnet at low but finite temperatures and its dynamics after quantum quenches. Here, we employ a modified spin-wave theory originally proposed by Takahashi, which we generalize to out-of-equilibrium scenarios.

---

[1] In our original work [1] we also addressed different systems using the same methods.

2.2 Probability distributions in Gaussian theories of bosons

2.2.1 Characteristic function

In the following sections we will be interested in quantum mechanical properties of observables that live in a subregion of an extended system. In particular, consider a generic system on a D-dimensional lattice and focus on a subsystem $\mathcal{A}$ with total number of sites $|\mathcal{A}| = \ell$. Given any Hermitian operator $R_\mathcal{A}$ with support only in $\mathcal{A}$, we want to determine the probability distribution function (PDF) $P_\mathcal{A}(r)$ of obtaining r as the outcome of a measurement of $R_\mathcal{A}$ in a state of the system characterized by the reduced density matrix (RDM) $\rho_\mathcal{A}$. Making no assumptions on the nature of the spectrum of $R_\mathcal{A}$, we can define $P_\mathcal{A}(r)$ in full generality as

$$P_\mathcal{A}(r) = \mathrm{Tr}_\mathcal{A}\left[\rho_\mathcal{A}\delta(r - R_\mathcal{A})\right] \qquad\qquad \rho_\mathcal{A} = \mathrm{Tr}_{\overline{\mathcal{A}}}\left[\rho\right] \ , \tag{2.1}$$

where $\overline{\mathcal{A}}$ is the complement of $\mathcal{A}$ and normalization derives from $\mathrm{Tr}_\mathcal{A}\left[\rho_\mathcal{A}\right] = 1$. In the case of observables with discrete spectrum, $P_\mathcal{A}(r)$ can be trivially interpreted as a discrete PDF.

$P_\mathcal{A}(r)$ can be rewritten in terms of the characteristic function $\chi_\mathcal{A}(\lambda)$ [131, 145]

$$\chi_\mathcal{A}(\lambda) \equiv \mathrm{Tr}_\mathcal{A}\left[\rho_\mathcal{A} \exp\left(i\lambda\, R_\mathcal{A}\right)\right] \qquad\qquad P_\mathcal{A}(r) = \int_{-\infty}^{\infty} \frac{d\lambda}{2\pi} e^{-i\lambda r} \chi_\mathcal{A}(\lambda) \ , \tag{2.2}$$

for which $\chi_\mathcal{A}(-\lambda) = \chi_\mathcal{A}^*(\lambda)$ holds. The characteristic function is bounded by $|\chi_\mathcal{A}(\lambda)| \leq 1$, as evident by resolving the trace in (2.2) over the eigenvectors of the RDM and applying Schwarz inequality to bound the contribution of the unitary operator $\exp\left(i\lambda R_\mathcal{A}\right)$.

In the following we will mostly be interested in the specific class of operators $R_\mathcal{A}$ that have discrete spectrum composed of equispaced eigenvalues

$$R_\mathcal{A}|m\rangle = r_m|m\rangle \qquad\qquad r_m = r_0 + m\, R \qquad\qquad r_0,\ R \in \mathbb{R}, \quad m \in \mathbb{Z} \ . \tag{2.3}$$

Given that $R_\mathcal{A}$ has support in the finite region $\mathcal{A}$, the set of integers m will be generally bounded. For this class of observables, the second formula in Eq. (2.2) can be simplified thanks to the periodicity

$$\chi_{\mathcal{A}}(\lambda + 2\pi n/R) = e^{i2\pi n\, r_0/R}\chi_{\mathcal{A}}(\lambda) \qquad\qquad n \in \mathbb{Z}\,. \tag{2.4}$$

Indeed, using (2.4), we can rewrite $P_{\mathcal{A}}(r)$ as

$$P_{\mathcal{A}}(r) = \sum_{n\in\mathbb{Z}} \int_{-\pi/R}^{\pi/R} \frac{d\lambda}{2\pi} e^{-i(\lambda+2\pi n/R)r}\chi_{\mathcal{A}}(\lambda)\, e^{i2\pi n\, r_0/R} = \tilde{P}_{\mathcal{A}}(r) \sum_{m\in\mathbb{Z}} \delta(r - r_0 - mR)\,, \tag{2.5}$$

where a Dirac comb emerges and

$$\tilde{P}_{\mathcal{A}}(r) \equiv \frac{R}{2\pi}\int_{-\pi/R}^{\pi/R} d\lambda\, e^{-i\lambda\, r}\chi_{\mathcal{A}}(\lambda) = \frac{R}{\pi}\,\mathrm{Re}\left[\int_0^{\pi/R} d\lambda\, e^{-i\lambda\, r}\chi_{\mathcal{A}}(\lambda)\right] \tag{2.6}$$

is normalized to 1 when viewed as a discrete PDF over the eigenvalues (2.3). The finite interval of integration in λ is the main advantage of (2.6) over the original (2.2) when numerical integrations are required.

2.2.2 Full-counting statistics in Gaussian theories of bosons

In this subsection we present the key *technical* result of this chapter: a compact formula for the characteristic function (FCS) of a quantum observable expressed as at most a quadratic polynomial in bosonic variables, when the quantum state can be expressed as a Gaussian function of said variables. The proof of the formula can be found in Appendix A.2.

Let $\{a_i\}_{i=1}^{\ell}$ be canonical annihilation operators for ℓ bosonic harmonic oscillators. These can be assembled into a 2ℓ-component vector

$$\boldsymbol{a}^\dagger = \{a_1^\dagger, \ldots, a_\ell^\dagger, a_1, \ldots, a_\ell\}\ , \qquad \left[\boldsymbol{a}_i, \boldsymbol{a}_j^\dagger\right] = \Sigma^z_{ij}\ , \tag{2.7}$$

where we have defined

$$\Sigma^x = \begin{pmatrix} 0 & \mathbb{I}_{\ell\times\ell} \\ \mathbb{I}_{\ell\times\ell} & 0 \end{pmatrix}\ , \qquad \Sigma^y = i\begin{pmatrix} 0 & -\mathbb{I}_{\ell\times\ell} \\ \mathbb{I}_{\ell\times\ell} & 0 \end{pmatrix}\ , \qquad \Sigma^z = \begin{pmatrix} \mathbb{I}_{\ell\times\ell} & 0 \\ 0 & -\mathbb{I}_{\ell\times\ell} \end{pmatrix}\ . \tag{2.8}$$

Let ρ denote the bosonic Gaussian state describing the system of ℓ bosons

$$\rho = \frac{1}{Z}\exp\left[\frac{1}{2}\boldsymbol{a}^\dagger W \boldsymbol{a} + \boldsymbol{w}^\dagger \cdot \boldsymbol{a}\right]\ , \tag{2.9}$$

where W is a Hermitian $2\ell \times 2\ell$ negative-definite matrix and $\boldsymbol{w}$ a vector of length 2ℓ such that $\boldsymbol{w}^\dagger = \boldsymbol{w}^T\Sigma^x$. The redundancy in the definition of $\boldsymbol{a}$ in (2.7), i.e. the simultaneous presence of both creation and annihilation operators, always allows us to choose W such that

$$\Sigma^x W \Sigma^x = W^T \ . \tag{2.10}$$

As a consequence of Wick's theorem the state ρ is fully characterised by the one and connected two-point functions of bosons [161, 162] (see Appendix A.2)

$$\boldsymbol{\omega} = \mathrm{Tr}\left[\rho\, \boldsymbol{a}\right] \ , \qquad \Delta = \mathrm{Tr}\left[\rho \left(\boldsymbol{a} - \boldsymbol{\omega}\right)\left(\boldsymbol{a}^\dagger - \boldsymbol{\omega}^\dagger\right)\right] - \frac{1}{2}\Sigma^z \ . \tag{2.11}$$

In defining the $2\ell \times 2\ell$ matrix Δ we made use of the outer product between the column vector $\left(\boldsymbol{a} - \boldsymbol{\omega}\right)$ and the row vector $\left(\boldsymbol{a}^\dagger - \boldsymbol{\omega}^\dagger\right)$.

Consider now a Hermitian operator R which is at most quadratic in the bosons

$$R = \frac{1}{2}\boldsymbol{a}^\dagger G \boldsymbol{a} + \boldsymbol{g}^\dagger \cdot \boldsymbol{a} \qquad \mathrm{Det}(G) \neq 0 \qquad \Sigma^x G \Sigma^x = G^T . \tag{2.12}$$

The last relation is analogous to (2.10), which we are always free to enforce. Our key result can be stated as follows.

Formula for the characteristic function

The characteristic function $\chi(\lambda)$ of the associated quantum mechanical PDF for the operator R in the state ρ can be represented in terms of one- and two-point functions as

$$\chi(\lambda) = \mathrm{Tr}\left[\rho e^{i\lambda R}\right] = Z_G \frac{\exp\left[-\frac{1}{2}\left(\boldsymbol{\omega}^\dagger - \boldsymbol{\omega}_G^\dagger\right)\left(\Delta + \Delta_G\right)^{-1}\left(\boldsymbol{\omega} - \boldsymbol{\omega}_G\right)\right]}{\sqrt{\mathrm{Det}\left(\Delta + \Delta_G\right)}} \ , \tag{2.13}$$

where

$$\begin{aligned} \boldsymbol{\omega}_G &= -G^{-1}\boldsymbol{g} \ , \qquad \Delta_G(\lambda) = -\frac{1}{2}\coth\left(i\lambda\frac{1}{2}\,\Sigma^z\, G\right)\Sigma^z \ , \\ Z_G(\lambda) &= \exp\left[-i\lambda\frac{1}{2}\,\boldsymbol{g}^\dagger G^{-1}\boldsymbol{g}\right] \mathrm{Det}\left[2\,\Sigma^z \sinh\left(-i\lambda\frac{1}{2}\,\Sigma^z G\right)\right]^{-1/2} \ . \end{aligned} \tag{2.14}$$

A derivation of (2.13) based on coherent states methods is presented in Appendix A.2. There we also discuss how the formula is modified in presence of a singular G. It is also possible to derive the formula by purely algebraic methods (see Appendix

D of our work [1]). We note that results similar to, but less general than, (2.13) have been derived in [163, 164]. Eq. (2.13) generalizes the analogous formula for the trace of the product of two physical Gaussian density matrices ρ_1 and ρ_2 specified by Hermitian negative-definite matrices [161, 165–167].

2.2.3 Static and dynamic self-consistent mean-field theory

To be able to use Eq. (2.13) we must restrict our treatment to Gaussian theories of bosons. In the context of quantum magnetism this will be achieved by mapping spin variables, which define the Hamiltonians of many models of interest, onto bosonic ones. The interacting bosonic Hamiltonian obtained in this way must then be approximated by a quadratic one through self-consistent mean-field theory, provided we are in a physical regime in which this step is expected to yield sensible results.

Self-consistent mean-field theory in equilibrium

The simplest example of a self-consistent mean-field theory (SCMFT) can be given for the case of thermal equilibrium, where expectation values of observables are computed as

$$\langle O\rangle_H = \frac{\mathrm{Tr}\left[\exp\left(-\beta H\right)\, O\right]}{\mathrm{Tr}\left[\exp\left(-\beta H\right)\right]}\ . \tag{2.15}$$

Here β denotes the inverse temperature and H is an interacting bosonic Hamiltonian. Suppose that H contains quartic interactions in bosonic variables, which we can schematically denote $\hat{A}\hat{B}\hat{C}\hat{D}$, and that thermal 1-point functions vanish, e.g. $\langle\hat{A}\rangle = 0$. The self-consistent mean-field decoupling consists in the replacement

$$\hat{A}\hat{B}\hat{C}\hat{D} \to \Big(\langle\hat{A}\hat{B}\rangle\hat{C}\hat{D} + \hat{A}\hat{B}\langle\hat{C}\hat{D}\rangle - \langle\hat{A}\hat{B}\rangle\langle\hat{C}\hat{D}\rangle\Big) + (\hat{B}\leftrightarrow\hat{C}) + (\hat{B}\leftrightarrow\hat{D})\ , \tag{2.16}$$

where now $\langle\,.\,\rangle$ denotes the self-consistent mean-field expectation value

$$\langle\hat{A}\hat{B}\rangle \equiv \frac{\mathrm{Tr}\left[\exp\left(-\beta H_{\mathrm{MF}}\right)\hat{A}\hat{B}\right]}{\mathrm{Tr}\left[\exp\left(-\beta H_{\mathrm{MF}}\right)\right]}\ , \tag{2.17}$$

and H_{MF} is the quadratic Hamiltonian obtained after decoupling H according to (2.16). Eq. (2.17) represents the self-consistent step. The SCMFT can be understood from a variational point of view: the Gaussian density matrix $\exp(-\beta H_{\mathrm{MF}})/Z_{\mathrm{MF}}$ minimizes the free energy associated with the interacting Hamiltonian H in the manifold of Gaussian states (*cf.* Gibbs-Bogoliubov inequality or see, e.g., [168]). Using this variational principle the decoupling (2.16) can be generalized to the case of higher-point interactions, or to the case in which odd-point functions, like $\langle \hat{A} \rangle$, do not vanish.

Self-consistent mean-field theory out-of-equilibrium

Imagine a quantum quench that starts from a Gaussian pure state $|\psi(0)\rangle$ and unitarily evolves according to H, i.e. $|\psi(t)\rangle = \exp(-iHt)\,|\psi(0)\rangle$. If H contains interacting terms in the bosons (i.e. it is not quadratic) then $|\psi(t)\rangle$ will be non-Gaussian for any $t > 0$. However, in certain physical scenarios one might hope that, for small or even intermediate time scales, $|\psi(t)\rangle$ remains sufficiently close to being Gaussian and hence that a time-dependent Gaussian approximation might yield results that accurately describe time evolution. A natural example are Hamiltonians with weak interactions governed by a small coupling ε. In such cases the approximation remains meaningful up to times that grow with $1/\varepsilon$.

One such type of approximations is known as self-consistent time-dependent mean-field theory (SCTDMFT) [1, 102, 103, 149, 169–179]. The idea is to replace the time-independent interacting Hamiltonian H with a *time-dependent* quadratic one $H_{\mathrm{MF}}(t)$, which defines an approximate evolution of the initial state as

$$|\psi_{\mathrm{MF}}(t)\rangle = U_{\mathrm{MF}}(t)\,|\psi(0)\rangle \qquad U_{\mathrm{MF}}(t) \equiv \mathcal{T}\left[\exp\left(-i\int_0^t dt'\, H_{\mathrm{MF}}(t')\right)\right] . \tag{2.18}$$

Here $\mathcal{T}$ is the time-ordering operator and $|\psi_{\mathrm{MF}}(t)\rangle$ is a Gaussian state $\forall\, t$. A proper derivation of SCTDMFT, which addresses the generic construction of $H_{\mathrm{MF}}(t)$ given any H, is presented in Appendix A.1. To give an example of what SCTDMFT looks like in a case of practical interest, we consider again a H involving quartic interactions $\hat{A}\hat{B}\hat{C}\hat{D}$. The substitution $H \to H_{\mathrm{MF}}(t)$ amounts to a decoupling identical to Eq. (2.16), where, however, the self-consistent expectation values (2.17) are replaced by time-dependent self-consistent ones

$$\langle \hat{A}\hat{B} \rangle(t) \equiv \langle \psi_{\mathrm{MF}}(t)|\hat{A}\hat{B}|\psi_{\mathrm{MF}}(t)\rangle . \tag{2.19}$$

In the presence of an interacting Hamiltonian, the quantum time evolution of an observable can be always rephrased as an infinite set of coupled differential equations in time, known as BBGKY hierarchy (see, e.g. [102, 103, 172]). In Appendix A.1 we prove that SCTDMFT is equivalent to truncating the infinite BBGKY hierarchy by assuming the validity of a Wick decomposition. There we also prove that SCTDMFT exactly conserves energy at all times

$$E = \langle\psi(0)|H|\psi(0)\rangle = \langle\psi_{\mathrm{MF}}(t)|H|\psi_{\mathrm{MF}}(t)\rangle \quad \forall\, t \; . \tag{2.20}$$

2.3 Magnetically ordered systems

2.3.1 2D and 3D Heisenberg antiferromagnet

The D-dimensional antiferromagnetic Heisenberg model is described by the SU(2) invariant Hamiltonian

$$H = J\sum_{\langle i,j\rangle} \boldsymbol{S}_i \cdot \boldsymbol{S}_j \qquad J > 0 \; , \tag{2.21}$$

where S_i^γ are spin-s operators with su(2) algebra $\left[S_i^\gamma, S_j^\rho\right] = i\delta_{ij}\epsilon_{\gamma\rho\omega}S_i^\omega$ on a D-dimensional hypercubic lattice with $N = L^D$ sites, the sum subscript $\langle i,j\rangle$ indicates that interactions are limited to neighbouring sites and periodic boundary conditions (PBC) are assumed. The ground-state of this model (for N even) is a non-degenerate SU(2) singlet [180, 181]. For $D > 1$ and any s, as well as for $D = 1$ (Heisenberg chain) and s half-odd integer, the gap to the first excited states vanishes in the thermodynamic limit [182, 183]. This is not the case for $D = 1$ and s integer, where the famous Haldane gap [184–186] persists in the thermodynamic limit.

In $D = 2$, the gapless nature of the spectrum leads to the spontaneous breaking of the rotational SU(2) symmetry at $T = 0$ [187]. The order parameter is the staggered magnetization

$$\Sigma = \sum_{i\in A} S_i^z - \sum_{j\in B} S_j^z \; , \tag{2.22}$$

where A and B are the "even" and "odd" sublattices respectively. In 3D the antiferromagnetic order persists also at $0 \le T < T_c$, with $T_c/J \simeq 1$ [188–192]. We are interested in calculating the PDF of the staggered magnetization in the presence of long-range order for a local subsystem $\mathcal{A}$ with total number of sites $|\mathcal{A}| = \ell$. We will focus both on the system at equilibrium for a given temperature $T < T_c$ and on the non-equilibrium time evolution following a global quantum quench from an ordered initial state. For the latter, we will start both from the classical Néel state or the ground state of the XXZ model, and time-evolve according to (2.21).

2.3.2 Holstein-Primakoff representation

To analytically study the model specified by (2.21) in the presence of long-range order, we employ the Holstein-Primakoff (HP) representation [193, 194] of the spin operators S_i^γ. In particular, we introduce two families of bosons a and b, respectively associated with sublattices A and B

$$\begin{aligned} S_i^z &= s - a_i^\dagger a_i \qquad & S_i^+ &= \sqrt{2\,s}\left(1 - \frac{1}{2\,s} a_i^\dagger a_i\right)^{1/2} a_i \\ S_j^z &= -s + b_j^\dagger b_j \qquad & S_j^- &= \sqrt{2\,s}\left(1 - \frac{1}{2\,s} b_j^\dagger b_j\right)^{1/2} b_j \ , \end{aligned} \tag{2.23}$$

where $s \geq 1/2$ and $S^\pm \equiv S^x \pm iS^y$. This is an exact representation of the su(2) spin algebra, as it can be verified using the bosonic commutation relations. HP exactly coincides with the original spin formulation in the physical Hilbert space of spins, which in bosonic language is the space spanned by all states with occupation number $a_i^\dagger a_i \leq 2s$, and similarly for b_i. Bosonic states with occupation numbers beyond $2s$ are unphysical. Crucially, the representation (2.23) does not connect physical and unphysical states. However, the presence of the square roots makes it intractable. To overcome this, one usually performs a Taylor expansion of the square root and truncates it at some order in the inverse powers of s. The truncation has the drawback of coupling the physical and unphysical Hilbert spaces, but it leads to very convenient expressions of the spin operators in terms of finite-order polynomials in the bosons. The intuitive rationale behind this scheme is that as long as one probes physical regimes in which occupation numbers remain sufficiently smaller than s, e.g. $\langle a_i^\dagger a_i \rangle \ll s$ (strong magnetic order is present), the truncated expansion is meaningful and the unphysical states generated play an insignificant role. This is the mechanism at the basis of spin-wave theory [187, 194–199] in ordered quantum magnets, which somewhat surprisingly can remain accurate down to s values of 1/2.

In the following we will truncate the expansion of the Hamiltonian (2.21) at $\mathcal{O}(s^0)$

$$\begin{aligned} H = J \sum_{\langle i,j \rangle} \Big[& -s^2 + s\left(a_i^\dagger a_i + b_j^\dagger b_j + a_i b_j + a_i^\dagger b_j^\dagger\right) \\ & - a_i^\dagger a_i b_j^\dagger b_j - \frac{1}{4}\left(a_i^\dagger a_i^2 b_j + a_i b_j^\dagger b_j^2 + \text{H.c.}\right) \Big] \, . \end{aligned} \tag{2.24}$$

Given the presence of quartic interactions we will refer to this truncation as HP4, while the truncation at $\mathcal{O}(s)$ is the standard linear spin-wave theory (LSW).

We note that alternative approaches, based on normal ordering the string of bosonic operators arising after the Taylor expansion of the square root, can generate exact[2] truncation schemes [194] (as recently rediscovered [200, 201]). However, as pointed out already by Kubo in [194], these representations lead to unphysical results when combined with mean-field approximations of the interacting terms, so that we do not consider them here.

2.3.3 Equilibrium PDFs

We apply the equilibrium self-consistent mean-field theory of Section 2.2.3 to decouple the quartic terms in (2.24). By directly passing to Fourier space in the bosons

$$\tilde{a}_k \equiv \sqrt{\frac{2}{N}} \sum_{i \in A} e^{-i\boldsymbol{k}\cdot\boldsymbol{x}_i} a_i \qquad\qquad \tilde{b}_k \equiv \sqrt{\frac{2}{N}} \sum_{j \in B} e^{-i\boldsymbol{k}\cdot\boldsymbol{x}_j} b_j \, , \tag{2.25}$$

we get the self-consistently decoupled Hamiltonian

$$H_{\text{MF}} = 2\, D J \sum_k \Big[\text{Re}(P)\,(\tilde{a}_k^\dagger \tilde{a}_k + \tilde{b}_k^\dagger \tilde{b}_k) + \gamma(k)(P^*\, \tilde{a}_k \tilde{b}_{-k} + P\, \tilde{a}_k^\dagger \tilde{b}_{-k}^\dagger)\Big] + C \, , \tag{2.26}$$

where C is a constant, $P \equiv s - f - g$ and

$$\begin{aligned} & f \equiv \langle a_i^\dagger a_i \rangle = \langle b_j^\dagger b_j \rangle \in \mathbb{R} && g \equiv \langle a_i b_j \rangle \quad i,j \text{ nearest-neighbours} \, , \\ & \gamma(k) \equiv \frac{1}{2\,D} \sum_{\vec{\delta}_i} e^{i\boldsymbol{k}\cdot\vec{\delta}_i} && |\gamma(k)| \leq 1, \;\; \gamma(k) \in \mathbb{R} \, . \end{aligned} \tag{2.27}$$

In the previous equation, $\langle\, . \,\rangle$ is the thermal expectation value (according to H_{MF}) at inverse temperature β and $\vec{\delta}_i$ runs over the vectors connecting a site to its nearest

---

[2] No coupling of physical and unphysical states.

neighbours. To lighten the notation, we use k in place of $\boldsymbol{k}$ to express the dependence of operators and variables on the vector $\boldsymbol{k}$. Note that we are working in a grand canonical ensemble, i.e. the trace involved in the thermal average is over the full Hilbert space of bosons[3]. In mean-field decoupling the interaction we have used the symmetries of the original Hamiltonian (2.24), i.e. we have set $\langle a^\dagger b\rangle$, $\langle aa\rangle$ and $\langle bb\rangle$ to zero because of the global U(1) symmetry $a \to e^{i\phi}a,\ b \to e^{-i\phi}b$ (which coincides with conservation of S^z_{tot}). Furthermore, $\langle a^\dagger a\rangle = \langle b^\dagger b\rangle$ because of the exchange symmetry $a \to b$. Note that setting the mean-fields f and g to zero brings us from the mean-field HP4 to LSW. We will assume that in equilibrium $g \in \mathbb{R}$ and check it self-consistently at the end. With this additional assumption we can diagonalize (2.26) by a canonical Bogoliubov transformation to a new set of bosons $\tilde{\alpha}_k$, $\tilde{\beta}_k$

$$\tilde{a}_k \equiv \cosh\theta_k\,\tilde{\alpha}_k - \sinh\theta_k\,\tilde{\beta}^\dagger_{-k} \qquad \tilde{b}_k \equiv \cosh\theta_k\,\tilde{\beta}_k - \sinh\theta_k\,\tilde{\alpha}^\dagger_{-k}\ , \tag{2.28}$$

with the angle θ_k defined by $\tanh 2\theta_k = \gamma(k)$. We arrive in this way to the diagonal form

$$H_{\text{MF}} = \sum_k \varepsilon_k(\tilde{\alpha}^\dagger_k\tilde{\alpha}_k + \tilde{\beta}^\dagger_k\tilde{\beta}_k) + E \qquad \varepsilon_k = 2\,DJP\sqrt{1-\gamma(k)^2}\ , \tag{2.29}$$

where E is a constant equal to the ground-state energy of H_{MF}. Given that $\varepsilon_k \to 0$ for $k \to 0$, the spectrum of H_{MF} is gapless, which is consistent with the presence of Goldstone modes associated with the spontaneous symmetry breaking of the SU(2) symmetry. It can be easily checked that below the transition temperature T_c, solutions to the self-consistent equations $f = 1/Z\,\mathrm{Tr}\left[\exp\left(-\beta H_{\text{MF}}\right)a^\dagger_i a_i\right]$ and $g = 1/Z\,\mathrm{Tr}\left[\exp\left(-\beta H_{\text{MF}}\right)a_i b_j\right]$ exist, g is real (consistent with previous assumption) and $0 < f < s$. The last inequality implies a nonzero order parameter, see (2.23), that reflects the presence of magnetic order [187].

The thermal Gaussian state is fully characterized by the set of all nonzero 2-point functions, i.e. $\Delta^{aa}_k \equiv \langle\tilde{a}^\dagger_k\tilde{a}_k\rangle$ and $\Delta^{ab}_k \equiv \langle\tilde{a}_k\tilde{b}_{-k}\rangle$, see Appendix A.2. Given (2.29),

---

[3] The chemical potential associated with the conserved z magnetization $S^z_{\text{tot}} = \sum_{j\in B} b^\dagger_j b_j - \sum_{i\in A} a^\dagger_i a_i$ is zero, reflecting the absence of external magnetic fields, and similarly for the x and y directions.

the Δ_k functions at inverse temperature β are easily found to be

$$\Delta_k^{aa}(\beta) = \frac{1}{2}\frac{(2n_k(\beta)+1)}{\sqrt{1-\gamma(k)^2}} - \frac{1}{2} \qquad \Delta_k^{ab}(\beta) = -\gamma(k)\left(\Delta_k^{aa}(\beta) + \frac{1}{2}\right) \ , \tag{2.30}$$

where $n_k(\beta) = [\exp(\beta\varepsilon_k) - 1]^{-1}$ is the Bose occupation for the mode of momentum k. Given that our interest is in a local subset $\mathcal{A}$ of ℓ total sites, the knowledge of the full density matrix $\rho = \exp(-\beta H_{\mathrm{MF}})/Z$ is not required and we can work with the RDM associated with $\mathcal{A}$. Given that the partial trace of a Gaussian state is another Gaussian state [161], $\rho_{\mathcal{A}}$ has the form of (2.9) but without linear terms

$$\rho_{\mathcal{A}} = \frac{1}{Z_{\mathcal{A}}}\exp\left[\frac{1}{2}\boldsymbol{a}^\dagger W\boldsymbol{a}\right] \ , \tag{2.31}$$

where $\boldsymbol{a}$ defined as in (2.7) is a 2ℓ vector that accommodates all a_i, $a_i^\dagger$, b_j, $b_j^\dagger$ operators, with $i,j \in \mathcal{A}$. To compute the PDF of the staggered magnetization $\Sigma_{\mathcal{A}}$ in $\mathcal{A}$, which we denote simply as $P_{\mathcal{A}}$, we start by expressing $\Sigma_{\mathcal{A}}$ in terms of the HP bosons

$$\Sigma_{\mathcal{A}} = \ell s - \sum_{i\in A\cap\mathcal{A}} a_i^\dagger a_i - \sum_{j\in B\cap\mathcal{A}} b_j^\dagger b_j \ . \tag{2.32}$$

It is evident that aside from the constant we can cast the previous quadratic observable in the general form (2.12). The PDF $P_{\mathcal{A}}$ is thus obtained by direct application of (2.6) and (2.13).

For the rest of this subsection we focus on the specific case $s = 1/2$, for which the effect of quantum fluctuations is the strongest in differentiating the quantum ground state from the classical ($s \to \infty$) Néel state. All the subsequent results are expected to become more accurate for higher values of s. As a consequence of the cluster decomposition principle and the central limit theorem, in states with a finite correlation length ξ and for large values of $\ell^{1/D} \gg \xi$, $P_{\mathcal{A}}$ approaches a Gaussian PDF with standard deviation that scales as the square root of the subsystem volume ℓ [145]. In states with power-law correlations the asymptotic PDF can be non-Gaussian if the decay is slow enough, see e.g. Refs [126, 132, 143].

In Fig. 2.1 we report $P_{\mathcal{A}}$ for a square subsystem $\mathcal{A}$ in the ground-state of the $s = 1/2$ 2D Heisenberg antiferromagnet, where LSW and mean-field HP4 give the

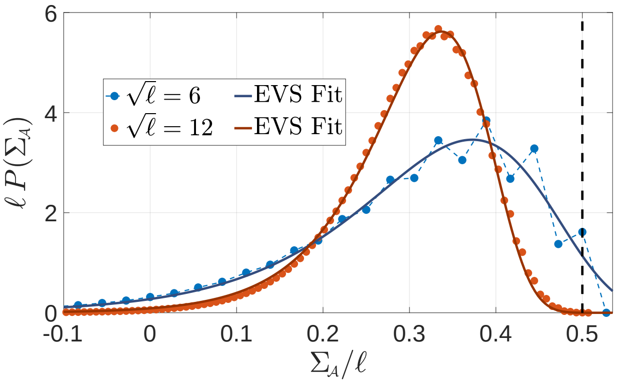

Figure 2.1: PDF of the staggered magnetization at $T/J = 0$ for the $s = 1/2$ 2D Heisenberg antiferromagnet in a square local subsystem $\mathcal{A}$ with ℓ total sites, for $\ell = 36$, 144. Phenomenological fits to extreme value statistics (EVS) Gumbel distributions are also shown. The vertical dashed line indicates the physical threshold of 1/2 for the staggered magnetization per site.

same result, given that the different scaling of ε_k is irrelevant at $T/J = 0$. Both the probabilities shown yield an average of the staggered magnetization that exactly matches the value of $\langle \Sigma_{\mathcal{A}} \rangle / \ell \simeq 0.303$ reported in literature [187]. As shown in Fig. 2.1, for intermediate values of ℓ the distribution $P_{\mathcal{A}}$ is well described by the extreme value statistics (EVS) Gumbel distribution

$$G(x|a,b) = \frac{1}{b} \exp\left[\frac{x-a}{b} - \exp\left(\frac{x-a}{b}\right)\right] \,. \tag{2.33}$$

We note that Gumbel distributions have previously appeared in the description of PDFs of fringe visibilities in interference experiments with 1D Bose liquids [143]. However, in the current context it is a phenomenological fit[4]. The fact that our $P_{\mathcal{A}}$ is exactly zero beyond the physical threshold $\Sigma_{\mathcal{A}}/\ell = 1/2$ is a direct consequence of the HP representation for the operator S^z, which does not allow eigenvalues larger than 1/2. In contrast, the lower bound of $\Sigma_{\mathcal{A}}/\ell = -1/2$ is violated as the constraint of the boson occupancy being at most one is not strictly enforced. However, in ordered systems this effect is greatly reduced by the condition of having a small number of bosons per site and indeed both curves in Fig. 2.1 are appreciable only within the physical region. Finally, an even/odd effect in the values of $\Sigma_{\mathcal{A}}$ is evident,

---

[4] Note that a *proper* identification of $P_{\mathcal{A}}$ with the Gumbel distribution requires an analysis of the extreme tails of the curve, which is not possible due to the finite range of values of the staggered magnetization associated with the intermediate ℓ for which the fit appears to be good.

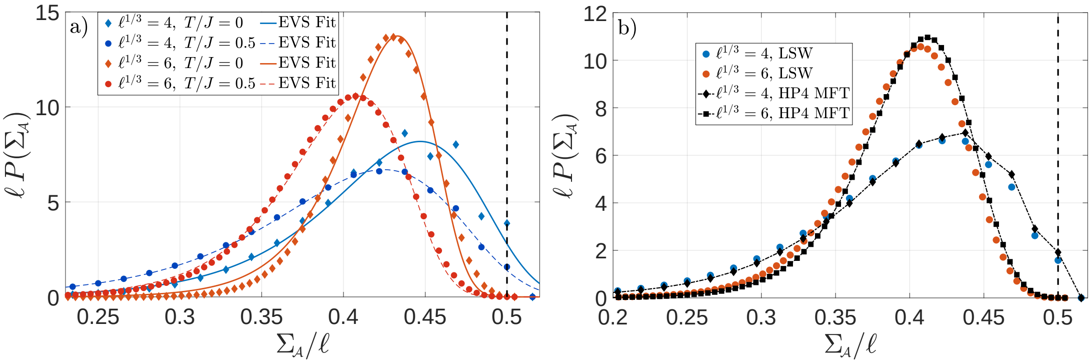

Figure 2.2: a) LSW PDFs of the staggered magnetization at $T/J = 0$ and $T/J = 0.5$ for the $s = 1/2$ 3D Heisenberg antiferromagnet in a cubic $\mathcal{A}$ with $\ell = 64, 216$, together with phenomenological extreme value statistics (EVS) Gumbel fits. Being at $T = 0$, these are also the curves for mean-field HP4. b) Differences between LSW and HP4 for $T/J = 0.5$. The vertical dashed lines indicate the physical threshold of 1/2 for the staggered magnetization per site.

in particular for $\ell = 36$, where the even and odd eigenvalues of the staggered magnetization follow two different smooth curves. Note that such an effect, already reported in PDFs of magnetic models in [132, 145], would have been difficult to infer from the sole knowledge of the first few moments of the distributions. As we will see below, the even/odd effect is usually associated with small temperatures and is suppressed by going to large values of ℓ.

In Fig. 2.2 we show the $s = 1/2$ 3D Heisenberg antiferromagnet $P_{\mathcal{A}}$ in a cubic subsystem $\mathcal{A}$ both in the ground-state and for $T/J = 0.5$, as calculated using LSW and the mean-field HP4 for $\ell = 64, 216$. The probabilities associated with the ground-state give an average $\langle \Sigma_{\mathcal{A}} \rangle/\ell \simeq 0.422$, exactly matching the known value reported in literature. We see how for $T/J = 0.5$ the temperature fluctuations reduce the ordered moment. Furthermore, the fact that for the mean-field of HP4 at $T/J = 0.5$ the term P, which rescales (with respect to LSW) the dispersion ε_k in (2.29), takes a value slightly larger than 1/2 is translated into a lower presence of excitations. This induces the small right-shift of the mean-field HP4 curves with respect to the LSW ones in Fig. 2.2b. By comparing the two curves at $T/J = 0$ in Fig. 2.2a, it is evident the beginning of the transition from a Gumbel-like shape towards a Gaussian one, given that for $\ell = 216$ the fit is not as good as for $\ell = 64$.

The plot for $\ell = 64$ and $T/J = 0.5$ also shows that the even/odd effect is not only suppressed by increasing ℓ, but also by increasing the temperature.

2.3.4 Out-of-equilibrium PDFs

The Holstein-Primakoff formalism from Section 2.3.2 can be employed also out-of-equilibrium. If we start from an initial state that breaks the SU(2) symmetry along the z direction, i.e. $\langle S_i^x \rangle = \langle S_i^y \rangle = 0$, $\langle S_i^z \rangle \neq 0 \; \forall \, i$, and time evolve according to (2.21), we have $\langle S_i^x \rangle = \langle S_i^y \rangle = 0$ throughout the time evolution. This is a direct consequence of the surviving U(1) symmetry (rotations around z) that the initial state possesses. Thus the HP representation (2.23) is suitable also in this out-of-equilibrium scenario, as long as the order does not melt. In particular, following a quantum quench an energy density e is injected into the system, and this corresponds to an effective temperature T_e in the thermal ensemble that is locally reached at late times (see Chapter 1). Hence, as long as $T_e < T_c$, we expect magnetic order, i.e. $\langle S_i^z \rangle \neq 0$, to survive at all times and the mean-field approximation to be applicable. In [1] we also addressed the more general case in which, during a time evolution, the vectorial order parameter $\langle \boldsymbol{S}_i \rangle$ changes both in direction and magnitude. In such cases, a “static” HP expansion around the z axis can become inaccurate already at very short times [1]. A path around this limitation was proposed in Refs. [202, 203], and further developed in [204, 205]. It is based on the idea of implementing spin-wave theory within a self-consistently determined rotating frame. In [1] we show that such an approach possesses some intrinsic complications that arise from the attempt to use SCTDMFT in a rotating frame. For example, unlike SCTDMFT in a fixed frame (Appendix A.1), the method does not conserve energy. We show in [1] that under certain conditions a better approximation can be obtained.

To study quench dynamics using the HP representation we apply the SCTDMFT, discussed in Section 2.2.3, to the HP4 Hamiltonian (2.24). We consider Gaussian initial states[5], such as the classical Néel state or the ground state of the XXZ Hamiltonian as determined by the self-consistent mean-field theory in equilibrium of Section 2.2.3. The time-dependent mean-field Hamiltonian $H_{\mathrm{MF}}(t)$ obtained by applying the normal-ordering procedure of Appendix A.1 is formally identical to (2.26), with the only difference in that the mean-field P acquires an explicit time dependence as a consequence of Eqs. (2.18) and (2.19). We remark that even if there is no small parameter in front of the quartic interaction in (2.24) to justify the applicability of the SCTDMFT, as long as the number of bosons per site is small (strong magnetic order) interactions among them are effectively suppressed, and the approximation is expected to be good on short and intermediate time scales. The Heisenberg equations of motion (EOM) for the Heisenberg picture operators $O(t) = U^{\dagger}_{\mathrm{MF}}(t)\, O\, U_{\mathrm{MF}}(t)$ are

$$\begin{aligned} \frac{d}{dt}\tilde{a}_k(t) &= -i\,2\,DJ\,\left[\mathrm{Re}(P(t))\,\tilde{a}_k(t) + P(t)\,\gamma(k)\tilde{b}^{\dagger}_{-k}(t)\right]\ , \\ \frac{d}{dt}\tilde{b}_k(t) &= -i\,2\,DJ\,\left[\mathrm{Re}(P(t))\,\tilde{b}_k(t) + P(t)\,\gamma(k)\tilde{a}^{\dagger}_{-k}(t)\right]\ . \end{aligned} \tag{2.34}$$

From these we find

$$\begin{aligned} \frac{d}{dt}\Delta^{aa}_k &= -4\,DJ\gamma(k)\,\mathrm{Im}(P^*\,\Delta^{ab}_k) \\ \frac{d}{dt}\Delta^{ab}_k &= -i\,4\,DJ\left[\mathrm{Re}(P)\,\Delta^{ab}_k + P\,\gamma(k)\left(\Delta^{aa}_k + \frac{1}{2}\right)\right]\ . \end{aligned} \tag{2.35}$$

Thanks to (2.35) we have complete knowledge[6] of the pure Gaussian state $|\psi(t)\rangle$ that approximates the time evolution of the system. As in Section 2.3.3, given our interest in PDFs within a local subset $\mathcal{A}$ of ℓ total sites, the knowledge of the full state $\rho = |\psi\rangle\langle\psi|$ at each time is not required and we therefore work with the Gaussian RDM $\rho_{\mathcal{A}}$, which has exactly the same functional form as (2.31). By making use of the representation (2.32) for $\Sigma_{\mathcal{A}}$, together with (2.6) and (2.13), we can directly obtain the PDF $P_{\mathcal{A}}$ for the staggered magnetization.

The HP4 Hamiltonian (2.24) possesses two local conservation laws: the energy, defined by the Hamiltonian itself, and the total z magnetization $S^z_{\mathrm{tot}} = \sum_{j\in B} b^{\dagger}_j b_j -$

---

[5] This is a requirement for the meaningful application of SCTDMFT, see Section 2.2.3.

[6] We solve (2.35) by a 4th order Runge-Kutta integration.

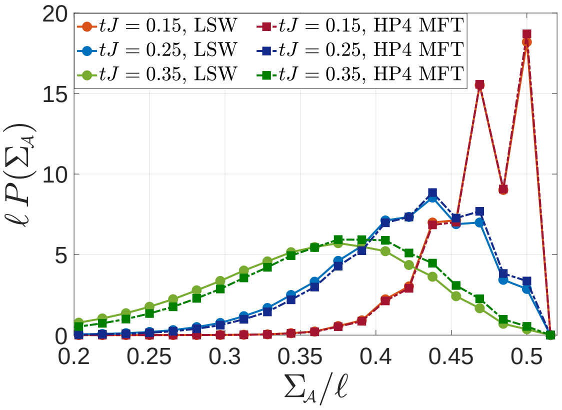

Figure 2.3: Early instants of the out-of-equilibrium evolution of $P_{\mathcal{A}}$ in a 3D cubic subsystem $\mathcal{A}$ with $\ell = 64$ total site and $s = 1/2$, following a quench from the classical Néel state according to LSW theory and the SCTDMFT of HP4.

$\sum_{i\in A} a_i^\dagger a_i$. Starting from an initial state that is an eigenstate of S^z_{tot}, the dynamics entirely takes place in the symmetry sector selected by the initial value of S^z_{tot}. Within it, the system is expected to locally relax towards a Gibbs ensemble [49, 50, 206] (see Section 1.2) whose effective temperature $1/\beta$ is fixed by the post-quench energy E_0 by requiring $E_0 = \langle H_{\text{HP4}}\rangle_\beta$. Given the equivalence of thermal ensembles in the thermodynamic limit [23], the Gibbs average within a single S^z_{tot} sector can be replaced by a Gibbs average over the entire bosonic Hilbert space (grand canonical average), provided that an appropriate chemical potential for S^z_{tot} is introduced. Actually, we will always start quenches in the sector $S^z_{\text{tot}} = 0$, and hence no additional chemical potential will be needed. In the spirit of assessing the SCTDMFT of HP4 as an approximation to the time evolution of the non-integrable interacting Heisenberg Hamiltonian (2.21), we will compare its late time behaviour with the mean-field HP4 Gibbs ensemble at the appropriate effective temperatures. Even if the SCTDMFT is by construction not expected to yield good results at late times [102, 103], in models where local observables relax quickly, i.e. over short time scales where the SCTDMFT is expected to work well, it is possible to describe approximate thermalization by this simple mean-field approach [178, 179].

We imagine to perform out-of-equilibrium time evolution following a global quantum quench starting from ground-states $|\mathrm{GS}, \eta\rangle$ of the XXZ model with anisotropy parameter $0 \leq \eta < 1$

$$H_{\mathrm{XXZ}}(\eta) = \sum_{\langle i,j\rangle} \left[\eta \left(S_i^x S_j^x + S_i^y S_j^y\right) + S_i^z S_j^z\right] \ , \tag{2.36}$$

and then quenching to the XXX Hamiltonian (2.21) corresponding to $\eta = 1$. In Fig. 2.3 we plot the early instants of the time evolution starting from the classical Néel state $|\mathrm{GS}, 0\rangle$ for the 3D case with cubic subsystem $\mathcal{A}$ of $\ell = 64$ total sites. The spin is again set to $s = 1/2$, which is the most difficult case for the type of HP scheme we are employing. The full order present at $t = 0$ is quickly destroyed by the energy injected in the system by the quench, whose associated effective temperature is of the order of $0.9J$ for both $1/\beta_{\mathrm{LSW}}$ and $1/\beta_{\mathrm{HP4}}$, i.e. very close to the transition temperature. Clearly, states too close to the transition, and more generally states where the order is greatly reduced, lie beyond the limit of validity of our approximation. Therefore, there is no reason to believe our approximation to be any good at later times in this specific case. At the short times considered, small differences between LSW and the SCTDMFT of HP4 are visible, and the very strong even/odd effect that is present for times $t < 0.20/J$ is almost completely suppressed already at times $t > 0.35/J$.

To obtain a time evolution that is accessible to our approximation up to later times, we need to reduce the energy injected in the system by the quench. This is obtained by reducing the parameter jump, i.e. we start from $|\mathrm{GS}, \eta\rangle$ with $\eta = 1/2$, $3/4$ and $9/10$. Such ground state is obtained by exactly the same steps discussed in Section 2.3.3, with the only difference in the replacement of $\eta = 1$ with $\eta < 1$. These quenches have effective temperatures $1/(J\beta_{\mathrm{HP4}}) \simeq 0.69, 0.54, 0.40$ in mean-field HP4. In Fig. 2.4 we plot $P_{\mathcal{A}}$ from the SCTDMFT of HP4 for $s = 1/2$ and a 3D cubic $\mathcal{A}$ with $\ell = 64$ sites, at initial, intermediate and late times after the quench from the three different values of η. We also compare the late-time curves with the thermal ones at the appropriate effective temperature. The $\eta = 3/4$ quench is also produced for $\ell = 216$. In all cases the system starts out at $t = 0$ being strongly ordered, with $P_{\mathcal{A}}$ featuring a peak close to $\Sigma_{\mathcal{A}}/\ell \sim 1/2$, which gets then

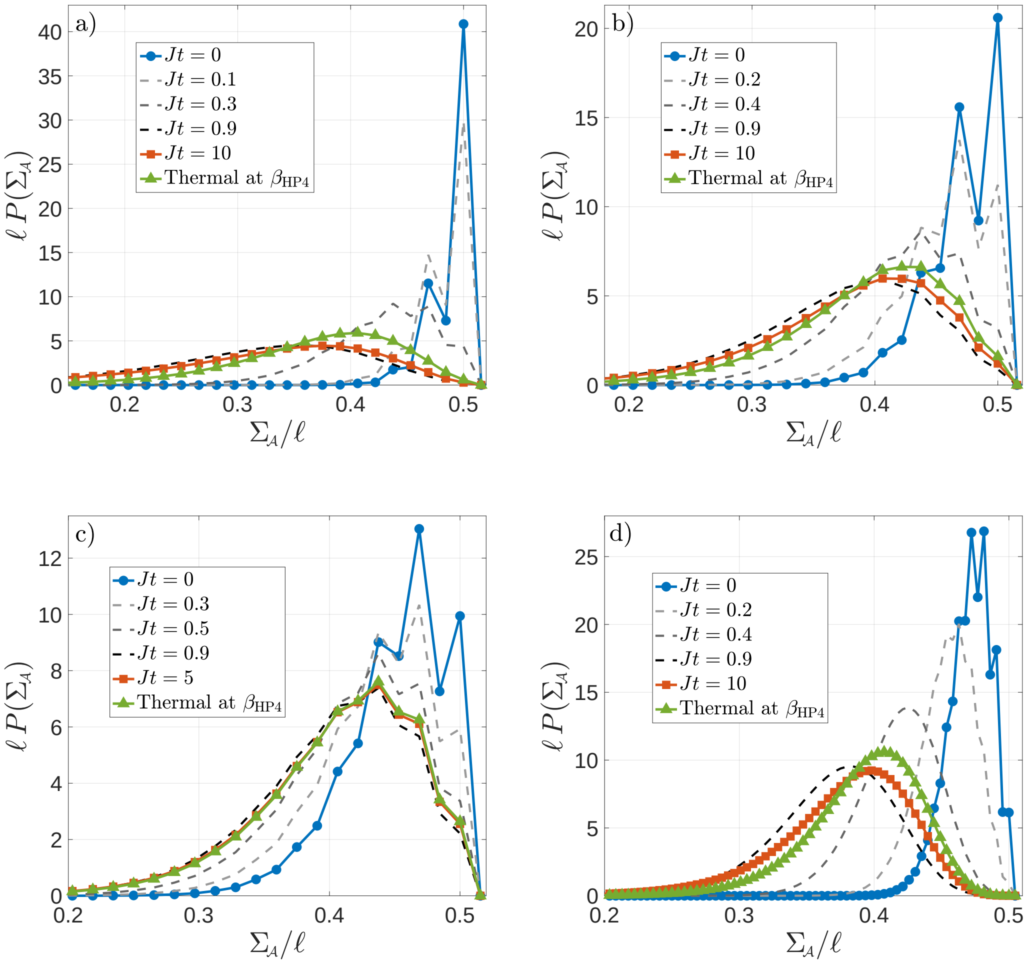

Figure 2.4: Initial, intermediate and late time $P_{\mathcal{A}}$ in the s-1/2 3D cubic subsystem with $\ell = 64$ for quenches from the ground-state of the XXZ model with a) $\eta = 1/2$, b) $\eta = 3/4$, c) $\eta = 9/10$. d) Same plot with $\ell = 216$ and $\eta = 3/4$. The late time probability distributions are compared with the equilibrium ones at appropriate effective temperature β_{HP4}.

gradually broadened and shifted to the left, in a way proportional to the energy injected by the quench. The deep quench $\eta = 1/2$, characterized by an effective temperature which is beyond half of the transition one, presents a strong difference between the initial PDF and the late-time stationary one. It is thus surprising that even for such a high injected energy the agreement between the late-time $P_{\mathcal{A}}$ and the thermal one is reasonable. In the case $\eta = 9/10$ the match between late time behaviour and Gibbs ensemble is essentially exact on the scale of Fig. 2.4c, which includes the initial probability. The even/odd effect present in every initial state of Fig. 2.4 is seen to disappear in the late time dynamics, except for the shallow quench $\eta = 9/10$, where a slightly suppressed even/odd effect is still visible at times $Jt \sim 5$. Finally, by comparing the two quenches for $\eta = 3/4$ of size $\ell = 64$ in Fig. 2.4b and $\ell = 216$ in 2.4d, we note that the agreement thermal state/stationary state in the latter is slightly worse. This is a consequence of the fact that the match in the 2-point functions between thermal and stationary state is slightly better for shorter distances[7], like the ones involved in the $\ell = 64$ plot.

2.4 2D disordered Heisenberg antiferromagnet: modified spin-wave theory

In the previous sections we have addressed the problem of approximately determining the PDFs of subsystem observables in models of quantum magnets that exhibit long-range magnetic order. We now turn our attention to the same problem in systems whose underlying quantum states are *disordered*, i.e. there is no spontaneous breaking of any symmetry and order parameters are identically equal to zero.

In particular, we concentrate on the isotropic 2D spin-1/2 Heisenberg antiferromagnet in thermal equilibrium at finite temperatures[8] and after quantum quenches starting from disordered initial states. Exactly as in Section 2.3.1, our aim is to obtain a good approximation to the FCS of the staggered magnetization. In our original work [1], we employed two different approaches, one based on the Schwinger boson mean-field theory (SBMFT) by Arovas and Auerbach [207] and the other on Takahashi's modified spin-wave theory (MSWT) [168, 208]. Although SBMFT has the appealing property of respecting the full SU(2) symmetry of the problem, it fails to quantitatively predict features of PDFs known from numerical studies. In particular, we compared the equilibrium PDFs obtained from SBMFT for the

---

[7] Indeed, in producing the PDFs via Eq. (2.13) all that matters are the 2-point functions in real space within the subsystem $\mathcal{A}$.

[8] Contrary to the case of $T = 0$ considered in Section 2.3.3, absence of long-range order at any $T > 0$ is guaranteed by Mermin-Wagner theorem.

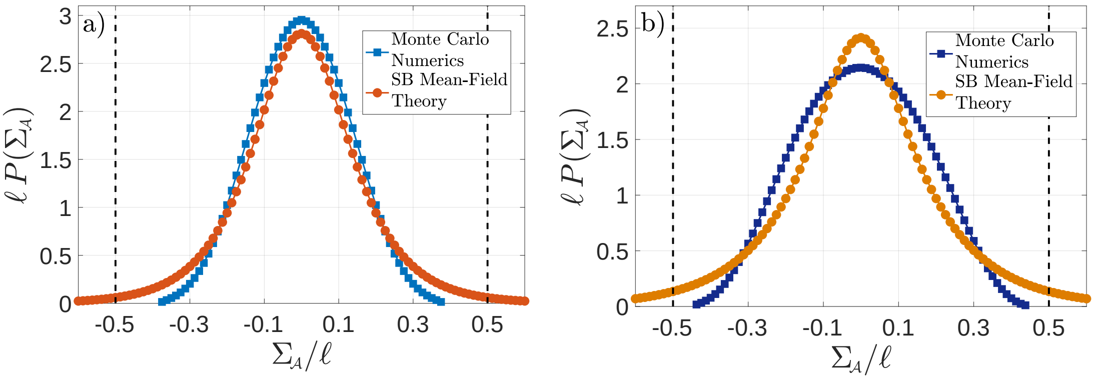

Figure 2.5: PDF for the staggered magnetization $\Sigma_{\mathcal{A}}$ in a disc-shape subsystem $\mathcal{A}$ of $\ell = 80$ sites as computed in SBMFT at a) $\beta = 1.59/J$ and b) $\beta = 2.22/J$. Comparison with the exact Monte Carlo results from [135] are shown. The black dashed lines represent the physical thresholds on the eigenvalues of $\Sigma_{\mathcal{A}}$.

staggered magnetization $\Sigma_{\mathcal{A}}$ with those available from Monte Carlo results[9] on a disc-shape subsystem $\mathcal{A}$ of $\ell = 80$ total sites at inverse temperatures $J\beta = 1.59, 2.22$ [135] (these were motivated by the geometry and temperatures of the experiment in [122]).

In Fig. 2.5 we plot the SBMFT results from [1] and compare them with the Monte Carlo PDFs. The main difference with the PDFs of ordered quantum magnets seen before is that now the curves are symmetric around zero, as expected for disordered systems. For the higher temperature ($\beta = 1.59/J$) shown in Fig. 2.5a the Monte Carlo results are well described by a Gaussian PDF, which as noted in Section 2.3.1 is expected to emerge asymptotically when the linear subsystem size becomes much larger than the correlation length. At the lower temperature ($\beta = 2.22/J$) shown in Fig. 2.5b the correlation length is larger and the Monte Carlo results are no longer well described by a Gaussian. The PDFs obtained from SBMFT are seen to be a poor approximation to the Monte Carlo data. In particular, the tails of the SBMFT distributions decay much slower than the Monte Carlo results and extend beyond the physical thresholds $\Sigma_{\mathcal{A}}/\ell = \pm 1/2$. The disagreement is especially pronounced at lower temperatures where the exact distribution is broader.

---

[9] These were obtained for the disc-shape subsystem embedded in a total system of linear size $L = 32$, which in general cannot be representative of the thermodynamic limit of the global system. However, for the temperatures and subsystem sizes considered here the finite-size effects arising from the use of such small L are expected to be negligible.

In this chapter, we show that MSWT, unlike SBMFT, is surprisingly effective in predicting PDFs with good accuracy. Compared to SBMFT, MSWT approaches the problem from a very different perspective: designing a way to employ a spin-wave formalism (Section 2.3) in a disordered context. The intuitive rationale behind this is that, despite the absence of magnetic order, at sufficiently low temperatures where antiferromagnetic correlations can be locally strong, a (modified) description in terms of spin waves can remain meaningful[10]. MSWT represents one of the simplest approximate descriptions of the 2D Heisenberg antiferromagnet at $T > 0$. Similarly to SBMFT, the spin-spin correlation length ξ predicted by this theory is

$$\xi \propto c_1/T \, \exp(c_2/T) \ , \tag{2.37}$$

where c_1, c_2 are $O(1)$ positive constants [209]. This functional dependence matches the one-loop renormalization group result for the nonlinear σ model, but the $1/T$ pre-factor disagrees with the two-loop RG calculation [210] and Monte Carlo results [187]. We start by briefly reviewing MSWT in equilibrium, and show that the reason why MSWT improves over SBMFT is that it reduces the weight associated with unphysical states. We then generalize MSWT to out-of-equilibrium scenarios in Section 2.4.3.

2.4.1 Takahashi's approach

Following the original derivation [168] we employ a Dyson-Maleev (DM) representation of spin operators [211, 212]

$$\begin{aligned} S_i^z &= s - a_i^\dagger a_i \qquad & S_i^- &= a_i^\dagger \qquad & S_i^+ &= (2s - a_i^\dagger a_i)\, a_i \qquad & i \in A \\ S_j^z &= -s + b_j^\dagger b_j \qquad & S_j^- &= b_j \qquad & S_j^+ &= b_j^\dagger (2s - b_j^\dagger b_j) \qquad & j \in B \ , \end{aligned} \tag{2.38}$$

where a_i and b_j are bosonic annihilation operators and $[a_i, b_j] = [a_i, b_j^\dagger] = 0$. Note that the DM representation is non-Hermitian with respect to the standard inner product, but it has the advantage (over the HP representation from Section 2.3.2)

---

[10] For example, in Ref. [208] Takahashi observed that MSWT provides a low temperature expansion of the free energy in the 1D Heisenberg *ferromagnet* that is in good agreement with the exact results obtained from Bethe-ansatz.

of being expressible in terms of only finite-order polynomials in the bosons. Clearly, a physical constraint on the boson occupation, identical to the one for HP bosons, applies here too. The DM representation yields the following expression for the $s = 1/2$ Heisenberg Hamiltonian

$$H = J\sum_{\langle i,j\rangle} \boldsymbol{S}_i\cdot\boldsymbol{S}_j = \frac{J}{2}\sum_{\langle i,j\rangle}\left(a_i^\dagger a_i + b_j^\dagger b_j + a_i b_j + a_i^\dagger b_j^\dagger - a_i^\dagger(a_i + b_j^\dagger)^2 b_j\right) - \frac{J}{2}L^2 \,. \tag{2.39}$$

In place of DM, it is also possible to employ HP and retain only terms involving at most 2n bosons in H, as done up to $n = 2$ in Section 2.3.1. This results in an approximation that (post mean-field decoupling) we refer to as "MSWT/HP2n".

The key step is mean-field decoupling the quartic interaction in (2.39) while ensuring a disordered state with $\langle S_j^\gamma\rangle = 0 \;\; \forall\, \gamma = x, y, z$. To obtain $\langle S_j^z\rangle = 0$ Takahashi introduces a chemical potential μ in the Hamiltonian that fixes the average occupation numbers $\langle a_i^\dagger a_i\rangle = \langle b_j^\dagger b_j\rangle = 1/2$, while the z-rotational invariance[11] ensures $\langle S_j^x\rangle = \langle S_j^y\rangle = 0$, together with

$$\langle a_i^\dagger b_j\rangle = \langle a_i a_{i'}\rangle = \langle b_j b_{j'}\rangle = 0 \qquad \forall\; i, i' \in A,\;\; j, j' \in B \,. \tag{2.40}$$

Imposing $\langle a_i^\dagger a_{i+q}\rangle = \langle b_j^\dagger b_{j+q}\rangle$ from the physical equivalence between the two sublattices, and setting $\langle a_i b_j\rangle \in \mathbb{R}$ to end up with a Hermitian mean-field theory, results in the MSWT/DM Hamiltonian

$$\begin{aligned} H_{\mathrm{MF}} &= -\,J\Delta\sum_{\langle i,j\rangle}\left(a_i^\dagger a_i + b_j^\dagger b_j + a_i b_j + a_i^\dagger b_j^\dagger\right) - \mu\sum_{i\in A,\, j\in B}\left(a_i^\dagger a_i + b_j^\dagger b_j\right) + E_{\mathrm{MF}} \\ &= -(4J\Delta + \mu)\sum_k\left(\tilde a_k^\dagger \tilde a_k + \tilde b_k^\dagger \tilde b_k\right) - 4J\Delta\sum_k \gamma(k)(\tilde a_k \tilde b_{-k} + \tilde a_k^\dagger \tilde b_{-k}^\dagger) + E_{\mathrm{MF}} \,, \end{aligned} \tag{2.41}$$

where $\Delta \equiv \langle a_i b_j\rangle \in \mathbb{R}$ for i, j nearest neighbours, E_{MF} is a constant and $\gamma(k)$ is defined as in (2.27). We note that MSWT/HP4 results formally in the same mean-field Hamiltonian (2.41) for $\Delta \in \mathbb{R}$, *cf.* (2.26). As we will see, this does not imply that MSWT/DM and MSWT/HP4 yield identical results for physical observables, given that they retain very different ways of expressing spin operators

---

[11] In terms of bosons, a rotation around the z-axis is obtained by $a \to a e^{i\phi}$, $b \to b e^{-i\phi}$.

in bosonic language (compare Eqs. (2.23) and (2.38)). The Hamiltonian (2.41) can be diagonalized by the following Bogoliubov transformation

$$\begin{aligned} \tilde{a}_k &= \cosh\theta_k\,\tilde{\alpha}_k - \sinh\theta_k\,\tilde{\beta}^\dagger_{-k} \qquad & \tilde{b}_k &= \cosh\theta_k\,\tilde{\beta}_k - \sinh\theta_k\,\tilde{\alpha}^\dagger_{-k} \\ \tanh 2\theta_k &\equiv \eta\,\gamma(k) & \eta &\equiv \frac{4J\Delta}{4J\Delta+\mu}\ , \end{aligned} \tag{2.42}$$

thus obtaining

$$H_{\mathrm{MF}} = \sum_k \varepsilon_k \left(\tilde{\alpha}^\dagger_k\tilde{\alpha}_k + \tilde{\beta}^\dagger_k\tilde{\beta}_k\right) + E_0 \qquad \varepsilon_k = -(4J\Delta+\mu)\sqrt{1-\eta^2\gamma(k)^2}\ . \tag{2.43}$$

Here we have $|\eta| < 1$ and $(4J\Delta + \mu) < 0$. In equilibrium at inverse temperature β the self-consistency equations for Δ and μ read

$$\Delta = -\frac{1}{L^2}\sum_k \frac{\eta\,\gamma(k)^2}{\sqrt{1-\eta^2\gamma(k)^2}}(1+2n_k)\ , \qquad 1 = \frac{1}{L^2}\sum_k \frac{(1+2n_k)}{\sqrt{1-\eta^2\gamma(k)^2}}\ , \tag{2.44}$$

where n_k is a Bose occupation number for a mode of energy ε_k at inverse temperature β. Very similar equations are obtained when dropping the assumption that Δ is real. We also note that they have the same form as the self-consistent equations obtained in SBMFT [213]. For $T > 0.91J$ the only solution to the self-consistent equations is the unphysical (trivial) one with $\Delta = 0$. This reflects the inability of MSWT to describe the high-temperature disordered phase of the 2D Heisenberg antiferromagnet, where nearest neighbours correlations are strongly suppressed. However, in the lower (but still finite) temperature interval $0 < T < 0.91J$ non-trivial solutions to (2.44) exist. This fully defines H_{MF}, which in turn gives us access to all the 2-point functions within the subsystem $\mathcal{A}$ of interest.

Despite having set $\langle S^\gamma_j\rangle = 0$ for $\gamma = x, y, z$, the mean-field theory constructed so far violates spin rotational symmetry. This is due to the particular choice of a quantization axis which is intrinsic to the DM representation (2.38) (or the HP one). This drawback is absent in the full SU(2)-invariant SBMFT, and must be resolved in order to correctly describe a magnetic phase without long-range order. To address this issue Takahashi introduces an explicit rotational averaging [208]. This involves the replacement of generic expectation values of (products of) spin operators by rotationally invariant ones, by means of an integral over the SO(3) Haar measure[12]

$$\langle\Psi|\mathcal{O}|\Psi\rangle \to \overline{\langle\Psi|\mathcal{O}|\Psi\rangle} = \frac{1}{8\pi^2}\int_0^\pi d\theta \sin\theta \int_0^{2\pi} d\phi \int_0^{2\pi} d\psi \, \langle\Psi|U^\dagger\, \mathcal{O}\, U|\Psi\rangle \ , \tag{2.45}$$

where U is a global SO(3) rotation

$$U(\theta,\phi,\psi) = \exp\left(i\theta\sum_i S_i^y\right) \exp\left(i\phi\sum_i S_i^z\right) \exp\left(i\psi\,\hat{n}\cdot\sum_i \boldsymbol{S}_i\right) \ , \tag{2.46}$$

and $\hat{n}$ is the direction specified by the θ and ϕ angles. This prescription ensures that for any SO(3) rotation V[13]

$$\overline{\langle\Psi|V^\dagger\, \mathcal{O}\, V|\Psi\rangle} = \overline{\langle\Psi|\mathcal{O}|\Psi\rangle} \ . \tag{2.47}$$

This procedure trivially generalizes to expectation values with respect to a density matrix ρ. Some examples of the rotational averaging are

$$\begin{aligned} &\overline{\langle\Psi|S_j^\alpha|\Psi\rangle} = 0 \ , \qquad \overline{\langle\Psi|S_j^\alpha S_k^\gamma|\Psi\rangle} = \frac{\delta_{\alpha,\gamma}}{3}\langle\Psi|\boldsymbol{S}_j\cdot\boldsymbol{S}_k|\Psi\rangle \ , \\ &\overline{\langle\Psi|(S_i^\gamma S_j^\gamma S_k^\gamma S_\ell^\gamma)|\Psi\rangle} \\ &\qquad = \frac{1}{15}\langle\Psi|\left(\boldsymbol{S}_i\cdot\boldsymbol{S}_j\right)\left(\boldsymbol{S}_k\cdot\boldsymbol{S}_\ell\right) + \left(\boldsymbol{S}_i\cdot\boldsymbol{S}_k\right)\left(\boldsymbol{S}_j\cdot\boldsymbol{S}_\ell\right) + \left(\boldsymbol{S}_i\cdot\boldsymbol{S}_\ell\right)\left(\boldsymbol{S}_j\cdot\boldsymbol{S}_k\right)|\Psi\rangle \ . \end{aligned} \tag{2.48}$$

2.4.2 PDFs in equilibrium

We start by considering the PDF associated with the on-site operators that define the physical constraint in the chosen bosonic representation of spins. For DM or HP this translates into calculating the PDF of the occupation number $n_i = a_i^\dagger a_i$ (identical to the one for b_j) in a thermal state at inverse temperature β. This provides a useful diagnostic for the role of unphysical boson states introduced by not treating the constraint exactly. Thanks to (2.40) and the fact that we impose $\langle n_i\rangle = 1/2$, it is possible to obtain a temperature-independent analytical expression for the one-site RDM ρ_1 of the mean-field equilibrium state, and its associated PDF for n_i

$$\rho_1 = \frac{2}{3}\exp\left[-\log(3)\, n_i\right] \qquad\qquad P_{n_i}(n) = \int_{-\pi}^{\pi}\frac{d\lambda}{2\pi}e^{-in\lambda}\frac{2}{3-e^{i\lambda}} \ . \tag{2.49}$$

---

[12] Given the lattice structure that we are considering, we always have an even total number of sites, which guarantees a total integer spin. This justifies the interchangeability SU(2) ↔ SO(3).

[13] It also automatically satisfies $\langle\Psi_0|\mathcal{O}|\Psi_0\rangle = \overline{\langle\Psi_0|\mathcal{O}|\Psi_0\rangle}$ for any singlet state $|\Psi_0\rangle$.

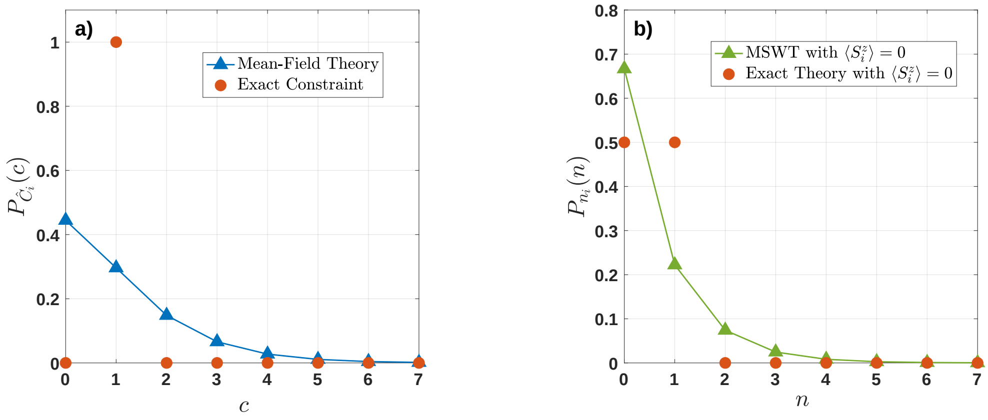

Figure 2.6: a) PDF of the constraint $\hat{C}_i$ in SBMFT (see [1]) and comparison with the exact constraint. b) PDF from mean-field MSWT of the occupation number $n_i = a_i^\dagger a_i$ and comparison with the exact distribution of a disordered spin-1/2 antiferromagnet.

In Fig. 2.6b we plot $P_{n_i}(n)$ as a function of n. For comparison with SBMFT, in Fig. 2.6a we report an analogous PDF for an on-site operator $\hat{C}_i$ that in the exact Schwinger-boson mapping is associated with the constraint $\hat{C}_i = 1$, which however SBMFT satisfied only on average $\langle \hat{C} \rangle = 1$ (see [1]). While also in MSWT there are significant deviations from the exact PDF, the agreement is better than for SBMFT. The higher weight given to unphysical states by SBMFT is the primary reason why it represents a poorer approximation than MSWT.

By turning our attention to PDFs of the staggered magnetization $\Sigma_{\mathcal{A}}$ in a subsystem $\mathcal{A}$, we however encounter a significant downside of MSWT (that SBMFT does not have): the physically-required rotational averaging (2.45) precludes us from applying our FCS formula (2.13). This is because the operator appearing in the expectation value $\overline{\langle \exp\left(i\lambda\Sigma_{\mathcal{A}}\right) \rangle}$ over the Gaussian RDM $\rho_{\mathcal{A}}$ is not a Gaussian bosonic operator, as required by Eqs. (2.12) and (2.13). We therefore resort to computing the first few cumulants of the PDF by brute force, i.e. employing Wick's theorem. The first and third cumulants vanish identically as a result of the rotational averaging. The second cumulant is given by

$$\overline{\kappa}_2 \equiv \overline{\langle \Sigma_{\mathcal{A}}^2 \rangle} = \frac{1}{3} \sum_{i,j \in \mathcal{A}} v_{ij} \langle \boldsymbol{S}_i \cdot \boldsymbol{S}_j \rangle \ , \tag{2.50}$$

where v_{ij} is equal to 1 if i, j are both in the same sublattice and -1 otherwise. Expressing the spin operators by the DM representation (2.38) and using (2.41)

$\overline{\kappa}_2/\ell$				
β	Monte Carlo	MSWT/HP6	MSWT/DM	SBMFT
1.59	1.32	1.56	1.59	2.38
2.22	2.19	2.51	2.71	3.89

Table 2.1: 2nd cumulant per site of the staggered magnetization $\Sigma_{\mathcal{A}}$ in the disc-shape subsystem $\mathcal{A}$ with $\ell = 80$ sites in the various mean-field approximations and Monte Carlo results from [135].

$\overline{\kappa}_4/\ell$				
β	Monte Carlo	MSWT/DM	MSWT/HP4	SBMFT
1.59	-51.5	-42.0	243.0	748.2
2.22	-240.2	-427.7	-60.8	2059.9

Table 2.2: 4th cumulant per site of the staggered magnetization $\Sigma_{\mathcal{A}}$ in the disc-shape subsystem $\mathcal{A}$ of $\ell = 80$ sites.

together with the condition $\Delta \in \mathbb{R}$ gives

$$\overline{\kappa}_2 = \frac{1}{3}\Big[2\sum_{i,i'\in A}\Big(\langle a_i^\dagger a_{i'}\rangle^2 + \frac{1}{2}\delta_{i,i'}\Big) + 2\sum_{i\in A,\, j\in B}\langle a_i b_j\rangle^2\Big] \qquad i,i',j\in\mathcal{A}\,. \tag{2.51}$$

The same result is obtained by expressing the spins in terms of HP bosons and discarding terms beyond quartic interactions. Thus $\overline{\kappa}_2$ is the same in MSWT/DM and MSWT/HP4.

We explicitly computed $\overline{\kappa}_2$ for the disc-shape subsystem $\mathcal{A}$ of $\ell = 80$ sites and the two temperatures $J\beta = 1.59, 2.22$ discussed above [122, 135]. In Table 2.1 we report values from MSWT/DM as well as the next order in the HP expansion (MSWT/HP6), obtained by including and mean-field decoupling sextic interactions in the Hamiltonian and taking into account sextic terms arising in (2.50). To facilitate comparison, we also report the results from the Monte Carlo simulations [135] and from SBMFT [1] (see Fig. 2.5). We see that the MSWT results are in fair agreement with Monte Carlo simulations, in clear contrast to SBMFT.

The 4th cumulant of $\Sigma_{\mathcal{A}}$ is given by

$$\overline{\kappa}_4 \equiv \overline{\langle\Sigma_{\mathcal{A}}^4\rangle} - 3\,\overline{\kappa}_2^2\,, \tag{2.52}$$

and its evaluation requires Wick decomposing a fairly large number of terms, as evident from (2.48). For this reason we limit the evaluation of $\overline{\kappa}_4$ to the cases

MSWT/DM and MSWT/HP4, for which we obtain the two different results reported in Table 2.2, together with the corresponding 4th cumulants from the Monte Carlo simulations and SBMFT. We see that MSWT/DM is better than MSWT/HP4 in this case, and that both are better than SBMFT.

We can also attempt an approximate reconstruction of the PDF from the knowledge of the first 4 cumulants (two of which vanish). This allows one to more easily visualize the comparison with the Monte Carlo data [135]. The cumulants $\overline{\kappa}_n$ are related to the characteristic function by

$$\chi_{\mathcal{A}}(\lambda) = \exp\left[\sum_{n=1}^{\infty} \overline{\kappa}_n \frac{(i\lambda)^n}{n!}\right] . \tag{2.53}$$

The approximation we employ follows from neglecting all $\overline{\kappa}_n$ for $n > 4$, i.e. expressing $\chi_{\mathcal{A}}(\lambda)$ as

$$\chi_{\mathcal{A}}(\lambda) \approx \exp\left[-\frac{1}{2}\overline{\kappa}_2\lambda^2 + \frac{1}{24}\overline{\kappa}_4\lambda^4\right] . \tag{2.54}$$

The approximate PDFs[14] generated by integrating (2.54) are shown in Fig. 2.7, with $\overline{\kappa}_2$, $\overline{\kappa}_4$ obtained from MSWT/DM or extracted directly from the Monte Carlo results. The agreement with the full Monte Carlo PDFs is significantly better than in the SBMFT case of Fig. 2.5. We note that the approximate construction of PDFs just presented works only under the condition $\overline{\kappa}_4 < 0$ and thus cannot be applied to MSWT/HP4 at $\beta = 1.59$, *cf.* Table 2.2.

2.4.3 Non-equilibrium dynamics and PDFs

We now generalize MSWT to non-equilibrium dynamics using SCTDMFT (Section 2.2.3). We focus on quantum quenches starting from initial states $|\psi_i\rangle$ that exhibit no magnetic order. We are particularly interested in situations where $|\psi_i\rangle$ is characterized by a short correlation length and low energy density relative to the ground state of the 2D Heisenberg antiferromagnet. We then expect the correlation length to grow under time evolution and the PDF of the staggered subsystem magnetization (along any direction) to become broader and flatter.

---

[14] The PDFs obtained assuming $\overline{\kappa}_n = 0$ for $n > 4$ contain in general some negative values and are not properly normalized, but these effects are negligible in the examples considered.

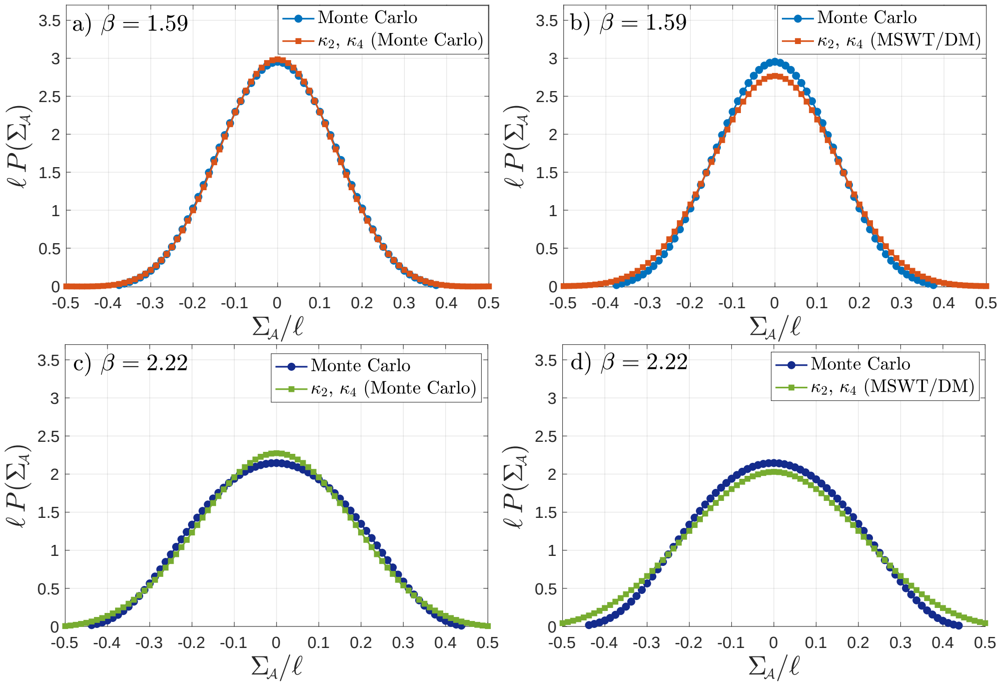

Figure 2.7: Staggered magnetization PDFs in the disc-shape subsystem $\mathcal{A}$ with $\ell = 80$ sites as reconstructed from 2nd and 4th cumulants using (2.54), and comparison with full Monte Carlo PDFs. a) $\beta = 1.59$ with $\overline{\kappa}_2$, $\overline{\kappa}_4$ extracted from full Monte Carlo PDFs. b) $\beta = 1.59$ with $\overline{\kappa}_2$, $\overline{\kappa}_4$ from MSWT/DM. c) $\beta = 2.22$ with $\overline{\kappa}_2$, $\overline{\kappa}_4$ extracted from full Monte Carlo PDFs. d) $\beta = 2.22$ with $\overline{\kappa}_2$, $\overline{\kappa}_4$ from MSWT/DM.

A clear difference with respect to previous applications of the SCTDMFT is that the DM Hamiltonian (2.39) is non-Hermitian. To proceed, we follow [214] and define the Heisenberg-picture time evolution for a non-Hermitian Hamiltonian $\tilde{H}$ (from an initial state $|\psi_i\rangle$) as

$$\langle\psi_i|e^{i\tilde{H}t}\, O\, e^{-i\tilde{H}t}|\psi_i\rangle \ . \tag{2.55}$$

This choice is sensible because it leaves the standard form of the Heisenberg EOM unchanged, from which we also see that setting $O = \tilde{H}$ still yields conservation of energy. If one could treat the evolution (2.55) exactly[15] the results would be identical to those of the Hermitian evolution in spin language. On the contrary, one might be worried that the use of mean-field schemes on (2.55) could lead to complex expectation values of Hermitian observables O and divergences (for $t \to \infty$) due to the complex nature of the spectrum of the non-Hermitian mean-field Hamiltonian.

---

[15] Hence, with no mixing of the physical and unphysical part of the bosonic Hilbert space.

We will verify that neither of these two issues appears in our treatment[16]. Within the prescription (2.55), the normal ordering of Appendix A.1 which is at the basis of SCTDMFT can be generalized to the case of non-Hermitian $\tilde{H}$, leading to a formally identical procedure to perform the mean-field decoupling. We hence arrive to the following time-dependent mean-field Hamiltonian

$$\begin{aligned} H_{\mathrm{MF}}(t) = -4\,J \sum_k \Big(\Delta(t)\,\tilde{a}_k^\dagger \tilde{a}_k + \overline{\Delta}(t)\,\tilde{b}_k^\dagger \tilde{b}_k\Big) \\ - 4J \sum_k \gamma(k) \Big(\overline{\Delta}(t)\,\tilde{a}_k \tilde{b}_{-k} + \Delta(t)\,\tilde{a}_k^\dagger \tilde{b}_{-k}^\dagger\Big) + E_{\mathrm{MF}}(t)\ . \end{aligned} \tag{2.56}$$

Here the two complex time-dependent mean fields $\Delta(t)$, $\overline{\Delta}(t)$ are defined by

$$\begin{aligned} &\langle O\rangle_t \equiv \langle\psi_i|U_{\mathrm{MF}}(t)^{-1}\,O\,U_{\mathrm{MF}}(t)|\psi_i\rangle\ , \qquad U_{\mathrm{MF}}(t) = \mathcal{T}\left[e^{-i\int_0^t ds\,H_{\mathrm{MF}}(s)}\right]\ , \\ &\Delta(t) = \langle a_i b_j\rangle_t\ , \quad \overline{\Delta}(t) = \langle a_i^\dagger b_j^\dagger\rangle_t\ , \quad i,j \text{ nearest neighbours.} \end{aligned} \tag{2.57}$$

In deriving (2.56) we have already used $\langle a_i^\dagger a_i\rangle_t = \langle b_i^\dagger b_i\rangle_t = 1/2 \ \ \forall\ t$, without the need to introduce any (time-dependent) chemical potential. This is possible because when starting from an initial state that satisfies $\langle\psi_i|n_j|\psi_i\rangle = 1/2$, the time evolution with the SCTDMFT Hamiltonian (2.56) automatically ensures that $\langle n_j\rangle_t = 1/2$ is fulfilled at all times (see third EOM below). The EOM for the momentum space 2-point functions derived from (2.56), (2.57) are

$$\begin{aligned} \frac{d}{dt}\langle\tilde{a}_k\tilde{b}_{-k}\rangle_t &= i4J\left[(\Delta+\overline{\Delta})\langle\tilde{a}_k\tilde{b}_{-k}\rangle_t + \Delta\,\gamma(k)\left(\langle\tilde{a}_k^\dagger\tilde{a}_k\rangle_t + \langle\tilde{b}_{-k}^\dagger\tilde{b}_{-k}\rangle_t + 1\right)\right]\ , \\ \frac{d}{dt}\langle\tilde{a}_k^\dagger\tilde{b}_{-k}^\dagger\rangle_t &= -i4J\left[(\Delta+\overline{\Delta})\langle\tilde{a}_k^\dagger\tilde{b}_{-k}^\dagger\rangle_t + \overline{\Delta}\,\gamma(k)\left(\langle\tilde{a}_k^\dagger\tilde{a}_k\rangle_t + \langle\tilde{b}_{-k}^\dagger\tilde{b}_{-k}\rangle_t + 1\right)\right]\ , \\ \frac{d}{dt}\langle\tilde{a}_k^\dagger\tilde{a}_k\rangle_t &= i4J\gamma(k)\left[\Delta\langle\tilde{a}_k^\dagger\tilde{b}_{-k}^\dagger\rangle_t - \overline{\Delta}\langle\tilde{a}_k\tilde{b}_{-k}\rangle_t\right] = \frac{d}{dt}\langle\tilde{b}_{-k}^\dagger\tilde{b}_{-k}\rangle_t\ . \end{aligned} \tag{2.58}$$

Crucially, the structure of (2.58) ensures that the initial conditions $\overline{\Delta}(0) = \Delta(0)^*$, $\langle\tilde{a}_k\tilde{b}_{-k}\rangle_0^* = \langle\tilde{a}_k^\dagger\tilde{b}_{-k}^\dagger\rangle_0$ and $\langle\tilde{a}_k^\dagger\tilde{a}_k\rangle_0$, $\langle\tilde{b}_k^\dagger\tilde{b}_k\rangle_0 \in \mathbb{R}$ remain valid at all times, despite the fact that $H_{\mathrm{MF}}(t)$ remains non-Hermitian at all times[17]. Thus, at the level of 2-point functions[18] the non-Hermitian time evolution defined by (2.57) preserves

---

[16] The absence of divergences is not surprising, given that by construction SCTDMFT conserves the expectation value of the energy.

[17] See terms in $H_{\mathrm{MF}}(t)$ proportional to $\tilde{a}_k^\dagger\tilde{a}_k$ and $\tilde{b}_k^\dagger\tilde{b}_k$.

[18] This is in contrast to the EOM for 1-point functions, which expose the non-unitary nature of $U_{\mathrm{MF}}(t)$ in (2.57). However, all 1-point functions vanish due to the z-rotational invariance of the DM and HP4 Hamiltonian.

the relations expected from a Hermitian theory. In fact, one can verify that by starting from the Hermitian HP4 Hamiltonian and performing the usual SCTDMFT decoupling of Appendix A.1, one arrives exactly at the EOM (2.58) with the identification $\overline{\Delta}(t) \equiv \Delta^*(t)$. From (2.58) we easily derive that $|\Delta|$ is a conserved quantity, and this ensures conservation of energy, which is always guaranteed when using SCTDMFT (Appendix A.1). The EOM for the phase ϕ of $\Delta = |\Delta| e^{i\phi}$ is

$$\frac{d\phi}{dt} = 8\,J \left[\mathrm{Re}(\Delta) + \frac{1}{L^2} \sum_k \gamma(k)^2 \left(\langle \tilde{a}_k^\dagger \tilde{a}_k \rangle + \langle \tilde{b}_{-k}^\dagger \tilde{b}_{-k} \rangle + 1 \right) \right] \ . \tag{2.59}$$

Having obtained all the EOM needed to characterize the Gaussian RDM, we turn to the construction of the initial state $|\psi_i\rangle$. We require $|\psi_i\rangle$ to respect the $\hat{z}$ rotational invariance and the spatial symmetries of the Hamiltonian, which constraints us to the functional form

$$|\psi_i\rangle = C \exp\left[-\frac{1}{2} \sum_{i \in A, j \in B} \eta_{ij} a_i^\dagger b_j^\dagger \right] |0\rangle \ , \tag{2.60}$$

where $|0\rangle$ is the vacuum of bosons and $\eta_{ij} := \eta(|\boldsymbol{x}_i - \boldsymbol{x}_j|)$ in order to enforce the spatial symmetries. The η_{ij} are chosen by requiring the state to be normalizable, to possess an average bosonic occupation on a site equal to $1/2$ and to be characterized by a sufficiently small correlation length ξ_i for spin-spin correlations. Even though (2.60) breaks SU(2) invariance, the latter is recovered after applying the averaging procedure (2.45). Furthermore, although by satisfying the constraint only on average the Gaussian state (2.60) is not a physical spin state, it is expected to generate dynamics with features similar to those obtained starting from physical singlet states, or SU(2)-invariant density matrices, with correlation length close to ξ_i. At late times the system governed by the Heisenberg Hamiltonian will thermalize at an effective temperature set by the energy density in the initial state (Section 1.2). Spin correlations in this thermal state can approximately be described by equilibrium MSWT and will possess a finite correlation length ξ_f. To clearly exhibit the growth of the spin correlation length under time evolution we adjust the parameters η_{ij} in order to achieve $\xi_f \gg \xi_i$. This is done by considering nonvanishing η_{ij} for the first seven consecutive classes of nearest-neighbours (η_i for $i = 1, \ldots, 7$) and

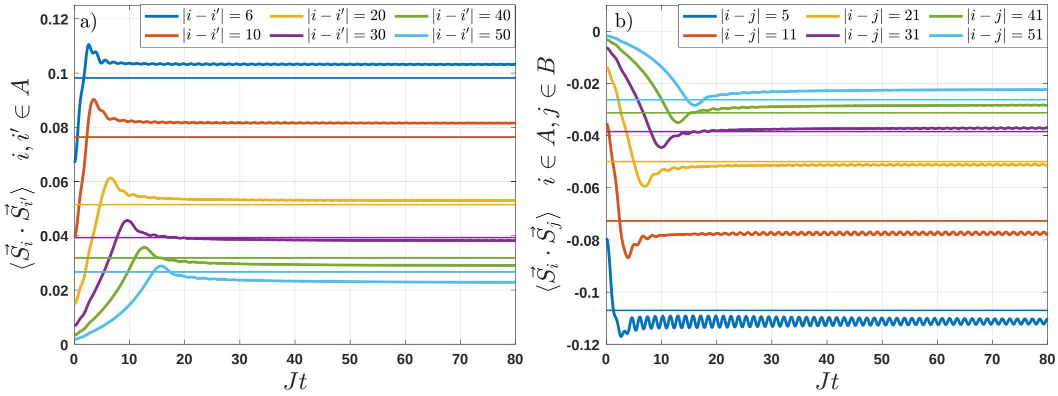

Figure 2.8: Time evolution of 2-point spin correlation functions in MSWT/DM–HP4 starting from the initial state (2.60) with $\eta_1 = 0.35$, $\eta_2 = \eta_3 \sim 0.024$, $\eta_4 \sim 0.012$, $\eta_5 = 0$, $\eta_6 \sim 0.008$, $\eta_7 \sim 0.015$ ($\xi_i \sim 20$, $\xi_f(\beta,\mu) \sim 200$), and comparison with thermal values at appropriate β and μ. a) Same sublattice. b) Different sublattices.

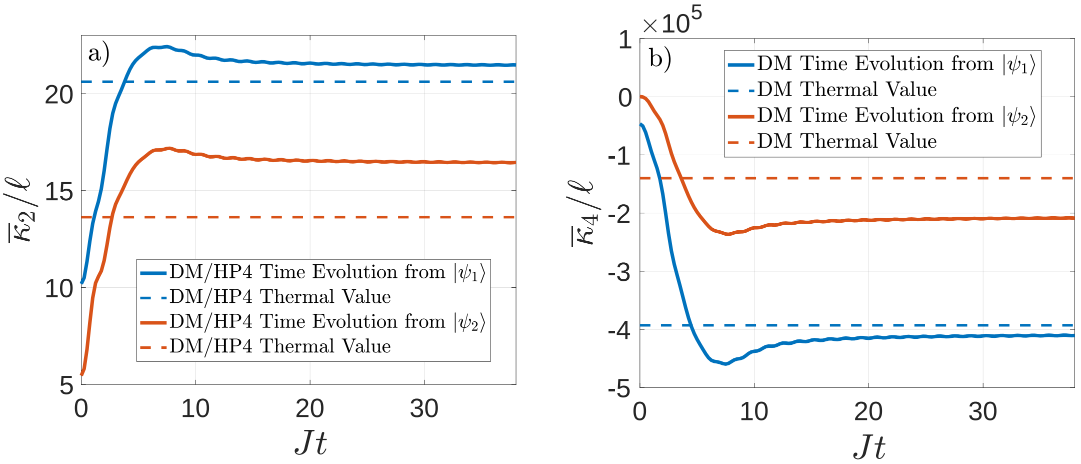

Figure 2.9: Time evolution of DM cumulants starting from the state $|\psi_1\rangle$ specified by the η_i of Fig. 2.8 and the state $|\psi_2\rangle$ specified by $\eta_1 \sim 0.386$, $\eta_2 \sim 0.017$, $\eta_3 \sim 0.012$, $\eta_4 \sim 0.007$, $\eta_5 \sim 0.001$, $\eta_6 \sim 0.0$, $\eta_7 \sim 0.025$ ($\xi_i \sim 10$, $\xi_f(\beta,\mu) \sim 45$). The subsystem $\mathcal{A}$ is a square with $\ell = 30 \times 30$ sites. Comparison with thermal values is shown. a) 2nd cumulant $\overline{\kappa}_2(t)$. b) 4th cumulant $\overline{\kappa}_4(t)$.

tuning them to have a low initial energy density (which ensures ξ_f large) while retaining $\xi_i \ll \xi_f$ (hence maximizing the correlation length growth). We stress again that while it is well-understood that a simple self-consistent time-dependent mean-field approximation like the one employed here cannot correctly describe thermalization [102, 103, 176, 177, 215], it can describe relaxation to a steady state that is approximately thermal, see e.g. Ref. [178].

In Fig. 2.8 we plot the time evolution, starting from (2.60), of some SU(2)-invariant 2-point functions of spins. The late-time behaviour captures their

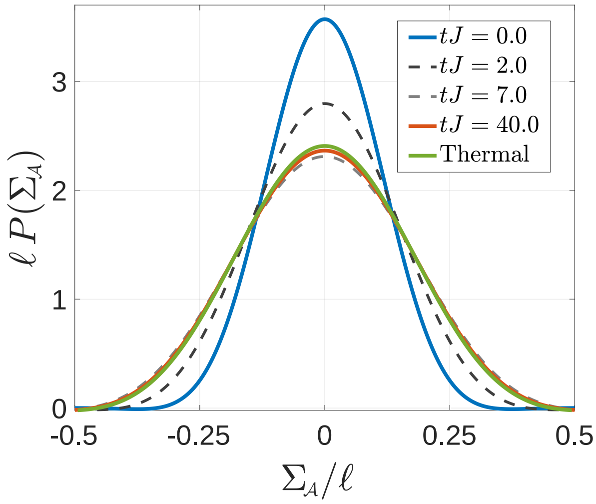

Figure 2.10: Approximate PDFs of $\Sigma_{\mathcal{A}}$ constructed from the DM 2nd and 4th cumulants at different times, in the time evolution from initial state specified by the η_i of Fig. 2.8. The subsystem $\mathcal{A}$ is the 30×30 square of Fig. 2.9. Comparison with the PDF constructed from the DM thermal $\overline{\kappa}_2$ and $\overline{\kappa}_4$ is shown.

approximate thermalization. As expected, correlators between spins on different sublattices possess antiferromagnetic character, as opposed to those within the same sublattice. Note that expressing the operators $\boldsymbol{S_i} \cdot \boldsymbol{S_j}$ in terms of bosons and using Wick contractions to compute their expectation value in the SCTDMFT yields identical results for the DM and HP representations. The same is *not* true for $2n$-point spin-functions with $n \geq 2$. In [1] we also showed that the time evolution for the 2-point spin functions agrees in functional form with the Lieb-Robinson bound for correlators [24, 25], and that $\Delta = \langle a_i b_j \rangle$ (i, j nearest-neighbours) relaxes to a real value at late times.

In Fig. 2.9 we show the DM time evolution, starting in two different initial states, of the 2nd and 4th cumulant of the staggered magnetization in a square subsystem $\mathcal{A}$ with $\ell = 30 \times 30$ sites. We compare the late time values with the DM thermal values at appropriate β and μ. The DM time evolution of the 2nd cumulant coincides with the HP4 result, but this is not true for the 4th cumulant. We avoid explicitly reporting results for the 4th cumulant from HP4 as they display a poorer agreement between stationary values and thermal ones, with respect to DM. This is perhaps not surprising given that HP4 represents a truncation of the exact HP mapping, while the DM mapping requires no truncation[19]. As seen in Fig. 2.9 both the 2nd and 4th cumulants increase in absolute value after the quench. This is a consequence of the fact that the final correlation length is larger than the initial one and thus antiferromagnetic correlations grow in strength. We also notice that the agreement between stationary values and thermal ones is better for the quench possessing a larger final correlation length. This is expected because, by construction, MSWT works better at low energy densities (low temperatures, in equilibrium).

Given that $\overline{\kappa}_4 < 0$ during the whole time evolution, we can generate approximate PDFs obtained from the knowledge of $\overline{\kappa}_2$ and $\overline{\kappa}_4$, exactly as done in equilibrium. The results are shown in Fig. 2.10. As expected the PDFs broaden in time and eventually approach their appropriate thermal values. Moreover, the shapes of the approximate PDFs are closer to what one might expect (after a quench in which the correlation length strongly increases) than those obtained, again for quench dynamics, with SBMFT in [1].

2.5 Conclusions

The main technical result introduced in this chapter is the determinant representation (2.13) for the FCS in Gaussian theories of bosons. This allowed us to explore the PDFs of the subsystem staggered magnetization, a local order parameter that is not conserved globally, in the paradigmatic Heisenberg antiferromagnet in dimensions $D = 2$ and 3. We obtained results in equilibrium and after quantum quenches, both in the presence and in the absence of long-range magnetic order, by employing (modified) spin-wave representations together with time-dependent self-consistent mean-field schemes.

Given the rich dynamics we uncovered for PDFs of the subsystem staggered magnetization after quantum quenches, it would be interesting to investigate these experimentally. This appears to be within close reach [122, 158–160].

---

[19] One may expect that considering higher truncations HP$2n$ with $n \geq 3$ would lead to results closer to DM.

3

Universal freezing transitions of charge- and dipole-conserving chains

3.1 Introduction

The phenomenon of HSF, introduced in Section 1.3.2, has been originally pointed out in the context of quantum chains conserving a charge N and its dipole moment X [108, 109, 113]. In this chapter, we present considerable progress on the analytical and numerical characterization of this paradigmatic class of ergodicity-breaking systems. These models effectively arise in the context of the quantum Hall effect [216, 217], in systems of particles exposed to strong tilt potentials [218–223], and in the presence of driving at special frequencies [224]. The combined effect of the two conserved charges and the finite local support of interactions greatly inhibits mobility and generates HSF. In particular, isolated charges cannot propagate on their own, as they require other nearby charges to interact with. This induces a fracture of (N, X) quantum sectors into multiple Krylov subspaces (Section 1.3.2) that are dynamically disconnected.

Recently, there have been attempts to understand how these and other types of systems undergo a continuous "freezing" phase transition between "weak" and "strong" HSF as the charge density $\nu = N/L$ (with L length of the chain) is varied [225–228]. These two distinct phases differ in the degree of fragmentation

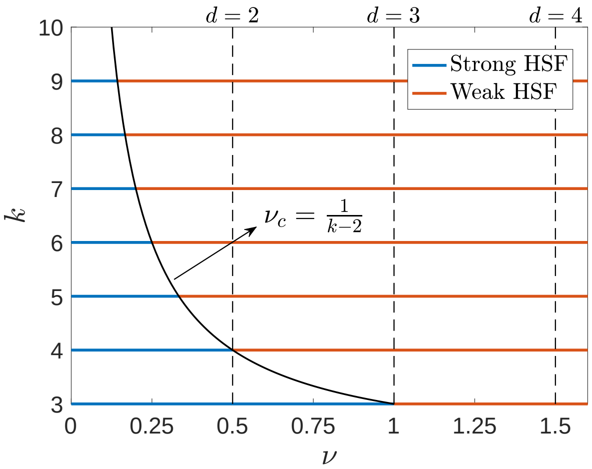

Figure 3.1: Conjectured universal (with respect to the on-site dimension d) phase diagram of charge- and dipole-conserving quantum chains with range-k interactions. The relevant variables are the continuous particle filling $\nu \geq 0$ and the discrete range of interactions $k \geq 3$. A first strong-to-weak fragmentation transition occurs at $\nu_c = 1/(k-2)$, and is independent of d. Note that for each value of d we depict the corresponding phase diagram *only below the half-filling* $(d-1)/2$ (vertical dashed lines). Beyond half-filling the phase diagram is *mirrored* by particle-hole symmetry, leading to a second opposite transition (not depicted here) at $d-1-\nu_c$. Also note that for $d=2$ it is only meaningful to consider $k \geq 4$, as there can be no dynamical evolution at $k=3$ which respects the global conservation laws.

they exhibit (see Section 3.2.2). By considering quantum chains with *unbounded* on-site dimension $d=\infty$, range-k interactions and charge-dipole symmetry, Ref. [226] analytically argued that the critical density for the freezing transition[1] is located at $\nu_c = (k-2)^{-1}$. In this chapter we make considerable progress on characterizing the transition in dipole-conserving chains with *any* on-site dimension d. In particular, we present analytical and numerical evidence that the critical density $\nu_c = (k-2)^{-1}$ of Ref. [226] is "universal": for arbitrary on-site Hilbert space dimension d, there is a strong-to-weak transition at $\nu = \nu_c$, with a second weak-to-strong transition at $\nu = d-1-\nu_c$ by particle-hole symmetry[2]. This leads to the universal phase diagram of Fig. 3.1. We note that, unlike previous analytical results on this phase transition [226], our framework provides several analytical insights into the dynamical impacts of strong fragmentation.

---

[1] In the largest dipole moment sector, as $N = \nu L$ varies.

[2] Note that this result on the precise location of the phase transition point in principle relies on the natural assumption of "gate completeness" discussed in Section 3.2.1.

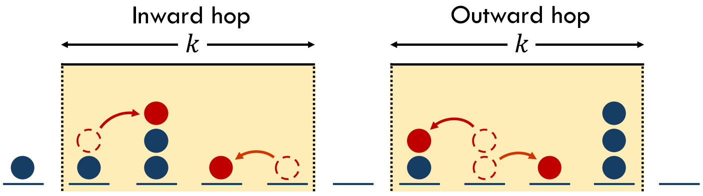

Figure 3.2: Examples of range-k gates ($k = 4$) implementing inward (left) and outward (right) hops that conserve N and X. The initial and final configurations are compatible with any on-site dimension $d \geq 4$.

The remainder of the chapter is organized as follows. In Section 3.2 we introduce the dipole-conserving models, and the order parameters that enable to distinguish between weak and strong HSF. In Section 3.3 we introduce a new framework to identify local hindrances to the global (dynamical) connectivity of the system. In particular, we uncover the existence of novel forms of obstructions to transport. In Section 3.4 we use this framework to analytically prove that *typical* (N, X) symmetry sectors at $\nu < \nu_c$ are strongly fragmented. In Section 3.5 we present numerical evidence compatible with the fact that typical (N, X) sectors at $\nu > \nu_c$ are weakly fragmented. In this section we also analytically determine some critical exponents, hence establishing on firm grounds the dipole-conserving universality class, and conjecture the existence of an inverse QMBS phenomenon on the basis of the EE of eigenstates. We highlight how the underlying mechanisms behind the non-ergodic features of the EE also have important consequences on quantum dynamics.

3.2 Fragmentation in dipole-conserving models

3.2.1 Charge- and dipole-conserving local models

Despite our main objective being the characterization of charge- and dipole-conserving *quantum* chains, due to the classical nature of HSF in these models significant progress can be made by considering their classical counterparts [225–227]. For many purposes, it is hence sufficient to focus on classical particles hopping on one-dimensional lattices and subject to finite-range local rearrangements that conserve a charge and its dipole moment.

We consider a chain of L sites with open boundary conditions (OBC), where each site can host from 0 up to $d-1$ particles, with $2 \leq d \leq \infty$. The particles dynamically evolve through sequences of hopping moves implemented via range-k gates, as depicted in Fig. 3.2. Letting n_i indicate the number of particles on site i, every gate conserves the total number of particles N and the dipole moment X

$$N = \sum_{i=0}^{L-1} n_i \qquad X = \sum_{i=0}^{L-1} i\, n_i \ . \tag{3.1}$$

We define the filling ν and the intensive centre of mass ν_x as

$$\nu = \frac{N}{L} \qquad \nu_x = \frac{X}{N\, L} \ , \tag{3.2}$$

where X/N represents the centre of mass. In order to uncover universal features of broad classes of dipole-conserving chains, we will require that the dynamics satisfies "gate-completeness", i.e. that the set of available gates (and their combinations) enables *all* possible rearrangements of particles compatible with range-k locality of interactions, maximal occupancy of $d-1$ and conservation of N and X. This is a very natural requirement, as it implies that if two particles are within a distance k one from the other, they can perform any move compatible with the constraints above. It is clear that violations of gate-completeness further reduce mobility. An example of this, for $d=4, k=4$, would be a chain in which the move on the left in Fig. 3.2 is available, but the move on the right is not allowed. We anticipate that, as a consequence of the additional hindrance to dynamics that a violation of gate-completeness entails, the main results for the strongly fragmented phase derived in this thesis remain unchanged.

In the following, we will be mainly concerned with understanding which and how many configurations can be reached starting from a given initial configuration of particles and performing classical (stochastic) dynamics, e.g. randomly drawing and applying sequences of range-k gates. Our focus will be on "infinite-time" properties, whose quantum counterparts describe the block diagonal structure of quantum dynamics and properties of eigenstates. Indeed, all the results derived in this thesis via classical reasoning have direct consequences on the physics of 1D quantum lattice models with any on-site Hilbert space dimension d and range-k interactions that conserve a charge $\hat{N}$ and its dipole moment $\hat{X}$, with $[\hat{N}, \hat{X}] = 0$. In the case of Hamiltonian quantum dynamics, the Hamiltonian H is a sum of range-k terms $\hat{h}_i^{(k)}$ and has a form identical to (1.19)

$$H(\boldsymbol{J}) = \sum_i J_i \, \hat{h}_i^{(k)} + \text{H.c.}\,, \qquad \left[\hat{h}_i^{(k)}, \hat{N}\right] = \left[\hat{h}_i^{(k)}, \hat{X}\right] = 0 \;\; \forall \, i \, . \tag{3.3}$$

Here any *individual* operator $\hat{h}_i^{(k)}$ (possibly non-Hermitian) can be chosen such that it maps product states in a properly defined "particle basis" to other product states in the same basis. Analogously to the classical case, we require gate-completeness of the set $\{\hat{h}_i^{(k)}\}$ and all their combinations. A standard example is a model of spin-s variables with $k = 4$ and Hamiltonian

$$H = \sum_{i=0}^{L-4} J_i \, \hat{S}_i^+ \hat{S}_{i+1}^- \hat{S}_{i+2}^- \hat{S}_{i+3}^+ + \sum_{i=0}^{L-3} K_i \, \hat{S}_i^+ (\hat{S}_{i+1}^-)^2 \hat{S}_{i+2}^+ + \text{H.c.}\ , \tag{3.4}$$

where $\hat{S}_i^{\pm}$ represent on-site raising and lowering operators and J_i, K_i are arbitrary scalars. Note that any product state in the $\hat{S}^z$ basis is in one-to-one correspondence with a product state in a particle basis with $d = 2s + 1$, where the on-site particle occupation $\hat{n}_i = (\hat{S}_i^z + s)$ allows one to define $\hat{N}$, $\hat{X}$ analogously to Eq. (3.1). Identical considerations can be applied to fermionic ($d = 2$) and bosonic ($d = \infty$) models. Instead of Hamiltonian dynamics, one can equally well consider (stochastic) quantum dynamics implemented via unitary circuits that are built using range-k quantum gates with charge and dipole conservation [109, 113].

In what follows we refer to individual configurations of particles on the chain simply as "states". In Section 3.5.2, where we discuss entanglement and quantum dynamics, we refer explicitly to "eigenstates" and "product states" to highlight their quantum nature. From now on, we restrict our attention to fillings $0 \leq \nu \leq (d-1)/2$. The regime $(d-1)/2 \leq \nu \leq d-1$ can be exactly mapped to the former by particle-hole symmetry. Similarly, our conclusions for $\nu_x \leq 1/2$ can be automatically extended to $\nu_x \geq 1/2$. Finally, we often implicitly resolve the dynamics of particles in terms of sequences of *pairwise one-site* hops. Indeed, provided gate-completeness is satisfied, it is easy to verify that this is always possible independently of the on-site dimension d (see [2] for a more explicit discussion).

3.2.2 Order parameters for the degree of fragmentation

Let $D^{(d)}_{N,X}$ denote the size (dimension) of a given (N, X) symmetry sector in the classical (quantum) setup. Given that N and X are the only "obvious" symmetries of the models introduced in the previous subsection and that terms like $\hat{h}^{(k)}_i$ in (3.3) represent genuine interactions, one might expect from the phenomenology of quantum chaotic models that N and X resolve the entire block diagonal structure of dynamics. However, this is not the case, as a consequence of the fractonic nature of dynamics that emerges from the interplay between conservation of N and X and the finite-range locality of interactions. The simplest way to see this is considering an isolated particle at a distance larger than $(k-2)$ (k is the finite-range of interactions) from other particles. Due to the conservation of X, the particle remains immobile until another particle enters its k-site interaction window. This is in striking contrast with more standard forms of dynamics, e.g. a simple tight-binding model. The major consequence of this N, X, k interplay is that each (N, X) symmetry sector necessarily fractures into exponentially many (in system size L) Krylov sectors[3]. These feature a wide variety of dimensions [108, 109], ranging from 1-dimensional to exponentially large ones. An example of a 1-dimensional Krylov sector, which therefore represents an eigenstate for any of the Hamiltonians $H(\boldsymbol{J})$, is depicted below for a chain with $(d = 3, k = 4, L = 26)$

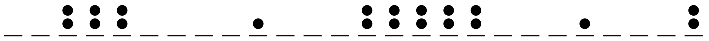
.

Here the two single particles are immobile because isolated by a distance equal or greater than $k-1$ from neighbouring ones, the two stacks of consecutive doubly-occupied sites are frozen because of the finite d constraint and the two particles on the right boundary cannot move due to the finite size of the chain and the open boundary conditions enforced. Note that for any choice of d and k it is possible to construct exponentially many (in L) 1-dimensional Krylov sectors by combining in

---

[3] Krylov sectors in the classical case are defined to be the set of product states in the particle basis that span their associated quantum Krylov subspace. Hence, classical Krylov sectors coincide with the subsets of states within each classical symmetry sector that are connected by the classical (stochastic) dynamics.

different ways frozen configurations like the ones just discussed [108, 109]. We will discuss examples of exponentially large Krylov sectors later in the chapter.

While in the highly constrained models with $(d = 2, k = 4)$ and $(d = 3, k = 3)$ it is possible to identify Krylov subspaces as the quantum number sectors of simple non-local symmetries expressed as "strings" of local operators [107, 112], we note that this is not possible for the general class of models with arbitrary d and k considered in this chapter[4].

Let $\mathcal{D}^{(d,k)}_{N,X}(i) \geq 1$ denote the dimension of the i-th Krylov sector (for some choice of indexing i) of a given (N, X) sector for on-site dimension d and interaction range k. Then we have

$$D^{(d)}_{N,X} = \sum_{i=1}^{K^{(d,k)}_{N,X}} \mathcal{D}^{(d,k)}_{N,X}(i) \ , \tag{3.5}$$

where $K^{(d,k)}_{N,X}$ is the total number of Krylov sectors in the (N, X) sector. Importantly, we always consider *families* of (N, X) sectors, where one family includes all the (N, X) sectors characterised by $N = \nu L$ and $X = \nu_x \nu L^2$ as we let L approach the thermodynamic limit, with ν and ν_x either fixed real numbers or fixed real functions of L. In terms of the dimensions just introduced, Refs. [108, 109] identified two distinct phases of HSF, characterized by a strikingly different degree of fragmentation. These are referred to as *strong* and *weak* fragmentation, and are defined in terms of the ratio

$$r^{(d,k)}_{N,X} = \frac{\mathcal{D}^{(d,k)}_{\max}(N, X)}{D^{(d)}_{N,X}} \ , \tag{3.6}$$

$$\lim_{L\to\infty} r^{(d,k)}_{N,X} = \begin{cases} 0 & \text{strong fragmentation} \\ 1 & \text{weak fragmentation} \end{cases} \ , \tag{3.7}$$

where $\mathcal{D}^{(d,k)}_{\max}(N, X)$ represents the dimension of the largest Krylov sector in a given (N, X) sector. We see that in families of symmetry sectors that are strongly fragmented each Krylov sector constitutes only a vanishingly small fraction of its corresponding symmetry sector. Furthermore, numerical evidence for small system

---

[4] The models with $(d = 2, k = 4)$ and $(d = 3, k = 3)$ are atypical in that they possess a higher degree of ergodicity-breaking compared to other choices of d and k. We later discuss this point further (see also the explicit discussion in [2]).

sizes has been given in Refs. [108, 109] that $r_{N,X}^{(d,k)}$ decays to zero exponentially fast with L. In contrast, in weakly fragmented families the largest Krylov sector includes in the thermodynamic limit a measure-1 fraction of all configurations present in the corresponding (N, X) sector. It is evident that strong and weak HSF represent two different scenarios within the realm of ergodicity-breaking mechanisms. In particular, strong fragmentation represents a strong violation of diagonal ETH (Section 1.2), given that typical eigenstates do not appear thermal within their corresponding (N, X) sector. On the contrary, in weakly fragmented (N, X) sectors only a vanishingly small fraction of all eigenstates is expected to be non-thermal, and ETH is violated only weakly [108]. In this sense, weak HSF is similar to weak ergodicity breaking due to QMBS (see Section 1.3), even though we note that in many models hosting QMBS the number of scar eigenstates scales polynomially with the volume of the system, while in systems hosting HSF, non-dominant (hence non-thermal) Krylov subspaces in weakly fragmented symmetry sectors are still exponentially many in L.

A different probe for the nature of fragmentation was introduced in Ref. [225]. Let $\rho_F^{(d,k)}(i)$ be the density of frozen sites in the i-th Krylov sector of a given N sector, where a frozen site is a site whose occupation number is the same throughout the entire Krylov sector. Then, numerical evidence for small system sizes suggests that the average density of frozen sites in a given N family of symmetry sectors, defined by the weighted average

$$\overline{\rho}_F^{(d,k)}(N, L) = \frac{\sum_{i=1}^{K_N^{(d,k)}} \rho_F^{(d,k)}(i)\, \mathcal{D}_{N,X}^{(d,k)}(i)}{\sum_{i=1}^{K_N^{(d,k)}} \mathcal{D}_{N,X}^{(d,k)}(i)} \;, \tag{3.8}$$

is a non-increasing function of the filling ν, which is exactly zero (in the thermodynamic limit) beyond a critical filling. Here we have defined $K_N^{(d,k)}$ to be the total number of Krylov sectors in fixed N sectors, i.e. we are not resolving[5] over

---

[5] One can also define a ratio of dimensions analogous to (3.6) that, however, does not resolve with respect to X. Its expression is identical to the right-hand side of (3.6) but with a sum over all X sectors (for a given N) both in the numerator and denominator.

the different dipole moments X compatible with N. The numerical evidence for $d = 3, k = 4$ and small system sizes in [225] is compatible with the existence of a unique critical filling, coinciding with our $\nu_c = (k-2)^{-1}$, that characterizes the phase transition point for *both* the ratio $r_{N,X}^{(d,k)}$ from (3.6) and the density of frozen sites[6] $\overline{\rho}_F^{(d,k)}$. We note that both the "order parameters" (3.6) and (3.8) introduced are highly non-local. For example, in computing $\overline{\rho}_F^{(d,k)}$ one cannot recognize a site as frozen without having first globally resolved the Krylov sector.

In the following sections we will obtain both analytic results and strong numerical evidence regarding the behaviour of these order parameters as a function of the filling ν. For example, in Section 3.4 we prove analytically that for any d, any $\nu < \nu_c = (k-2)^{-1}$, and any *typical*[7] family of (N, X) sectors, $r_{N,X}^{(d,k)}$ decays to zero exponentially with L and hence these families are strongly fragmented.

3.3 Blockages and fully extended states

We present in this section a framework that allows us to analytically characterise the strongly fragmented phase of models with any on-site dimension d. It also forms the basis of the efficient numerical procedure for addressing the weakly fragmented phase discussed in Section 3.5.3.

The main idea behind our formalism is that the degree of "dynamical connectivity" in the system is directly related to the presence or absence of *blockages* along the chain. These are defined as subregions of the chain across which transport of particle number and dipole moment cannot occur, i.e. blockages prevent the regions to their left and right from exchanging particles and dipole moment quanta. We prove the existence of two distinct types of blockages, which we classify as *type-1* and *type-2*. The former involve $k-1$ or more consecutive empty sites that are frozen, and hence create a disconnection in the system due to the finite range k of

---

[6] Despite this powerful connection between the strongly fragmented phase and the presence of finite densities of frozen sites, it is quite easy to verify that in the regime $(k-1)^{-1} \leq \nu < \nu_c$ rare Krylov sectors devoid of frozen sites exist for any d (see Section 3.4.3).

[7] Here with "typical" we mean families characterized by an intensive centre of mass $\nu_x = 1/2 + o(L^0)$, as these exponentially dominate their corresponding N sectors for large L (as we prove in Section 3.4.1).

interactions. Type-2 blockages are more subtle, as they do not involve frozen sites but still prevent transport. For $d = \infty$, we show that type-1 and type-2 blockages can be efficiently located by analyzing simple *local* properties of a special state called a "fully extended state" (FES) that is present in each Krylov sector, despite the fact that blockages reflect *global* properties of the sector. We then generalize our results to finite on-site dimension d by a procedure we refer to as the "FES picture". Finally, we discuss special Krylov sectors that lack blockages, and hence that possess a high degree of dynamical connectivity. Perhaps unsurprisingly, in later sections we will be able to connect the existence of these special sectors to the onset of the weakly fragmented phase.

3.3.1 Blockages as local features of fully extended states

Our framework for identifying blockages is centred around the concept of FES originally introduced in Ref. [226]. An FES is a state of a $d = \infty$ system in which no pair of particles can perform an outward hop (*cf.* Fig. 3.2). In this regard, it is important to remember that two particles separated by $k - 3$ or more empty sites (holes) *cannot perform an outward hop.* This significantly constraints the structure of any FES. Indeed, to exclude the possibility of performing outward hops an FES can host at most 1 particle on any of its sites and different particles must be separated by sequences of at least $k - 3$ holes. On the two boundary sites of the open chain, however, an indefinite number of particles can be stacked and there is no lower bound on how many holes separate each of these stacks from the next closest particle. An example of an FES with $k = 5, N = 12, X = 162$ is

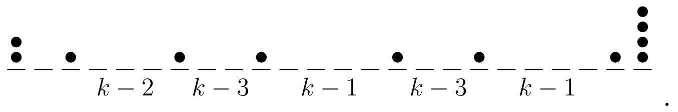

In a $d = \infty$ system an FES can always be reached by starting from any initial configuration of particles and applying outward hops (irrespective of the order of application) until it is no longer possible to proceed further [226]. Clearly, this statement relies on the natural assumption of gate-completeness discussed in

Section 3.2.1, and it is not true for systems with finite values of d[8]. In Appendix A of [2] J. Classen-Howes proved the following uniqueness property of FESs for any range of interactions k:

In a $d = \infty$ system, an FES cannot be dynamically connected to a different FES, i.e. each Krylov sector possesses a unique FES.

We now show that in $d = \infty$ systems this uniqueness enables the identification of blockages from *local* features of FESs, despite the fact that blockages reflect *global* properties of Krylov sectors. An obvious but important property for the following derivation is that any subsystem composed of adjacent sites of an FES also represents an FES (with associated uniqueness) if considered in isolation. We call any such contiguous subregion of an FES a "sub-FES".

Type-1 blockages. Consider a $d = \infty$ system and an FES that possesses a sequence of $k-1$ or more consecutive holes somewhere along the chain, as depicted below

$$\cdots\underline{\bullet}\;\underset{\geq k-1}{\underline{}\;\underline{}\ldots\underline{}}\;\underline{\bullet}\cdots \quad .$$

Given that 2 particles separated by $k-1$ or more empty sites cannot interact, the subsystems on either side of these holes can be dynamically connected only if one of them expands further, i.e. if one of the 2 particles in the figure is "pushed" towards the other and reaches the k-site interaction window of the latter. However, the left and right subsystems represent sub-FESs that are (by uniqueness of FESs) maximally expanded, and hence none of them can push its corresponding boundary particle. This proves that the $k-1$ empty sites are frozen and hence the regions on their left and right are dynamically disconnected. A consequence of this is that dynamics will conserve N and X separately on both sides of the hole sequence. Thus, the hole sequence represents a blockage composed of empty frozen sites.

---

[8] Because the maximal occupation of $d-1$ on each site can lead the system to remain stuck in a state where no further outward hops can be applied, even though it does not coincide with an FES.

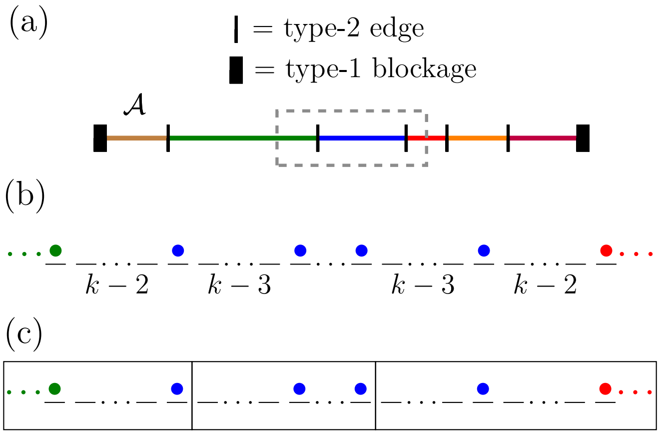

Figure 3.3: Schematic representation of type-2 blockages, as identified from the sub-FES that occupies a region $\mathcal{A}$ of the chain. (a) Example of region $\mathcal{A}$ enclosed by two type-1 blockages. Subregions separated by a type-2 edge (i.e. a sequence of exactly $k-2$ consecutive holes in an FES) are associated with particles of different colours. Any region consisting of two type-2 edges and the sites enclosed by them represents a type-2 blockage. (b) Close-up of the portion of region $\mathcal{A}$ highlighted by the dashed gray rectangle in panel (a), where two sequences of $k-2$ holes (type-2 edges) appear in the FES. In between the two type-2 edges, particles are separated only by sequences of $k-3$ holes. (c) Example of a possible partition of the portion of $\mathcal{A}$ from panel (b) into disjoint subregions that can at most host two different colours. Note that it is irrelevant where between two chosen particles of the FES we place a given partition cut.

Type-2 blockages. Consider a $d=\infty$ system in an FES and a subregion $\mathcal{A}$ of the chain that is enclosed by two type-1 blockages, so that $\mathcal{A}$ is dynamically disconnected from the rest of the chain. We also require that within $\mathcal{A}$ there are no type-1 blockages. In cases where there are no type-1 blockages in the entire system, $\mathcal{A}$ coincides with the whole chain. Let us denote as "type-2 edge" any sequence of $k-2$ consecutive holes enclosed between two particles in an FES. Within $\mathcal{A}$ we can employ a useful colour scheme according to which regions separated by a type-2 edge have particles of different colours, as schematically depicted in Fig. 3.3(a) and (b). In the example of Fig. 3.3(b) two type-2 edges are separated by a nonzero number of sequences of $k-3$ holes. However, type-2 edges can also be next to each other, i.e. enclose just one particle and no sequence of $k-3$ holes.

Consider the "local" Krylov sector composed of all the particle configurations in $\mathcal{A}$ that can be reached starting from the sub-FES that originally occupies $\mathcal{A}$. In Appendix B.1 we prove that:

Any configuration in this local Krylov sector can be dynamically reached by partitioning $\mathcal{A}$ into disjoint subregions that contain at most two different colours each and, starting from the sub-FES, performing independent series of hops within each of these subregions.

We note that different particle configurations in the local Krylov sector might be associated with different partitions of $\mathcal{A}$. In the following, we will refer to the statement above as "2-colour connectivity". An example of a 2-colour partition for the local subregion in Fig. 3.3(b) is represented in Fig. 3.3(c).

With reference to the particle configurations and colours of Fig. 3.3(b)-(c), let us refer to the region consisting of the two type-2 edges and all the sites enclosed by them as the "central region". An elementary consequence of the 2-colour connectivity is that the green and red regions cannot exchange particles or dipole moment quanta, and hence that the central region represents a blockage. Indeed, the 2-colour connectivity ensures that given any particle configuration in the local Krylov sector, we can find a cut somewhere along the central region such that the particle number and dipole moment to the left and right of the cut are the same as in the original sub-FES. In striking contrast to type-1 blockages, here no frozen site is involved and the green and red regions can exchange particles and dipole quanta with the blockage. Identical conclusions hold for all the other colours in $\mathcal{A}$, *cf.* Fig. 3.3(a).

In the following we will refer to any subregion of an FES devoid of type-1 blockages and consisting of two type-2 edges and the sites enclosed by them as a "type-2" blockage. These constitute an example of active blockages in that they do not involve frozen sites.

3.3.2 The FES picture

The methods just introduced to identify blockages when $d = \infty$, which leverage the nice properties of FESs, allow us to also address systems with finite d. Consider a configuration of particles on the chain in a system S with d finite. Starting from this state, we can imagine to perform dynamics in an auxiliary system $\tilde{S}$ which is identical to S aside from having no upper bound on the maximal on-site occupancy, i.e. $\tilde{d} = \infty$. This allows us to apply outward hops until we reach the corresponding unique FES in $\tilde{S}$. If in this FES some sequences of empty sites constitute type-1 blockages, the same sites will also be empty and frozen in the finite-d system S, thus representing frozen blockages there as well. Indeed, the Krylov sector in S associated with the initial state is included in the corresponding Krylov sector in $\tilde{S}$, as a consequence of the fact that any dynamical move allowed in the finite-d case is also allowed for $\tilde{d} = \infty$ (but the converse is not true). By similar reasoning, sites identified with type-2 blockages in $\tilde{S}$ constitute, or are part of, blockages also in S. Indeed, they necessarily prevent the propagation of particles and dipole moment between the regions to their left and right. In the following, we refer to this approach that maps a configuration of the system S to its corresponding FES in the auxiliary system $\tilde{S}$ as the "FES picture".

We remark that the only blockages that can exist for $\tilde{d} = \infty$ are type-1 and type-2 blockages. However, in general, S might possess frozen sites and blockages in addition to those it has in common with $\tilde{S}$, due to the maximal occupation constraint of $d - 1$ particles per site. Importantly, there can be finite-d blockages in S that cannot be identified using the FES picture. The simplest example is given by $k - 1$ or more contiguous sites with maximal occupation $d - 1$ embedded in an otherwise empty chain. These sites are clearly frozen in S, but when using the FES picture no type-1 blockage emerges to signal them, and hence this finite-d feature is invisible to the FES picture. We note that finite-d blockages are accounted for by the numerical methods addressing the weakly fragmented phase in [2]. They are expected to play a minor role in the transition.

3.3.3 Blockage-free FESs

Given the dynamical disconnections induced by the presence of blockages, it is natural to ask if Krylov sectors devoid of type-1 and type-2 blockages can exist. Defining n_1 and n_2 respectively to be the number of type-1 blockages and of type-2 edges in an FES, we see that a Krylov sector devoid of blockages must necessarily contain a “blockage-free FES”, i.e. its unique FES must be characterized by $n_1 = 0$ and $n_2 = 0$ or 1. Thus, if one considers all the separations between neighbouring particles in a blockage-free FES, there can be at most one separation of $k-2$ holes while all the other separations must be of $k-3$ holes, with the only exception being the separations next to the two boundary sites which can be composed of fewer than $k-3$ holes. Note that stacking remains allowed at the two boundary sites and that the single sequence of $k-2$ holes, if present, can also be in-between one of the boundary sites and the next closest particle. An example of a blockage-free FES for $k = 6$, $L = 21$, $N = 13$, $X = 112$ is given by

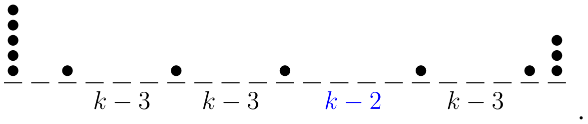

Importantly, blockage-free FESs can only exist for states with filling $\nu \geq \nu_c$ (*cf.* Section 3.4), which already hints at their importance for the onset of the weakly fragmented phase. Fillings $\nu < \nu_c$ are compatible with another special class of FESs, composed of a sub-FES which hosts no blockages and is surrounded by empty sites (which constitute frozen blockages) up to the chain boundaries[9]. We refer to the latter type of FESs and to blockage-free FESs collectively as “particle-connected” (PC) FESs, given that both types host no “disconnections” between the leftmost and rightmost of their particles. In [2] J. Classen-Howes and I proved that:

Given an interaction range k, there exists one and only one PC FES within each (N, X) sector.

Cases in which the unique PC FES is not a blockage-free FES arise when $\nu < \nu_c$ or when the centre of mass X/N is significantly far from the centre of the chain (the latter case is atypical, as we will see in Section 3.4.1). From the analysis in Section 3.4 it will become apparent that, for any d, in typical weakly fragmented (N, X) sectors a *necessary* condition for a Krylov sector to be the dominant one, i.e. the one appearing in the limit of $r^{(d,k)}_{N,X}$ going to 1 in (3.7), is for it to be free of

---

[9] Note that it is also possible for the sub-FES to overlap with one of the two boundaries.

blockages. This means that dominant Krylov sectors must necessarily be mapped by the FES picture to the unique blockage-free FES associated with the chosen (N, X) sector. The intuition behind this is that a dominant Krylov sector cannot possess the strong dynamical disconnections induced by the presence of type-1 and type-2 blockages. In Section 3.5.3 we will present numerical evidence for $d = \infty$ that a *necessary and sufficient* condition for a typical (N, X) sector to be weakly fragmented is for it to contain a blockage-free Krylov sector (which dominates in size the symmetry sector). In [2] this conclusion is extended numerically to finite-d systems.

3.4 Analytic characterisation of strong fragmentation

In this section we prove that, given any on-site Hilbert space dimension d, any *typical* (see below) family of symmetry sectors with $\nu < \nu_c = (k-2)^{-1}$ is strongly fragmented. In particular, we show that the decay of the ratio $r_{N,X}^{(d,k)}$ in Eq. (3.6) is exponential with L. The proof relies on the fact that for $\nu < \nu_c$ there is an *extensive* presence of blockages along the chain. This leads to a significant restriction of the number of configurations that can be reached from a given initial state via range-k dipole-conserving dynamics, and hence implies strong fragmentation.

We start by discussing the scaling of the dimensions of symmetry sectors, and defining what we mean by a "typical" symmetry sector. This, combined with the FES picture, allows us to very easily prove that the region $\nu < (k-1)^{-1}$ is strongly fragmented. We then present the full proof, which addresses the less trivial region $(k-1)^{-1} \leq \nu < \nu_c$. Some of the technical details for this last part are discussed in Appendix B.2.

3.4.1 Size of symmetry sectors and typicality

The asymptotic formulas (and related statements) reported in this subsection have been derived by me in Appendix D of [2]. For some of them, I made use of recent results from the mathematical literature [229].

Let $D_N^{(d)}$ denote the total number of configurations in the symmetry sector of $N = \nu L$ particles, where we do not fix the dipole moment X. For $0 < \nu < d-1$ and asymptotically large L one has (see Appendix D of [2])

$$\ln D_N^{(d)}(L) = L\,\eta_d(\nu) - \frac{1}{2}\ln L + \mathcal{O}(L^0)\ . \tag{3.9}$$

Here $\eta_d(\nu)$ is a strictly concave $\mathcal{O}(L^0)$ function of ν with a unique global maximum at half-filling $\nu^* = (d-1)/2$, where it takes the value $\eta_d(\nu^*) = \ln d$. We can also consider the dimension $D_{N,X}^{(d)}$ of the symmetry sector with $N = \nu L$ particles and $X = \nu\,\nu_x L^2$ dipole moment. Its asymptotic form is

$$\ln D_{N,X}^{(d)}(L) = L\Big(\eta_d(\nu) - \Lambda_d(\nu,\nu_x)\Big) - 2\ln L + \mathcal{O}(L^0)\ , \tag{3.10}$$

where $\Lambda_d(\nu,\nu_x) \geq 0$. For ν_x sufficiently close to $1/2$ the function Λ_d can be expanded as

$$\Lambda_d(\nu,\nu_x) = \lambda_d(\nu)\,\nu_{x0}^2 + o(\nu_{x0}^2)\ , \tag{3.11}$$

where λ_d is a positive function and $\nu_{x_0} = \nu_x - 1/2$ is the intensive centre of mass when the origin is set in the middle of the chain. If we fix ν, Eqs. (3.10) and (3.11) imply that for any family of $(N = \nu L, X)$ sectors characterized by $\nu_{x_0} = o(L^0)$, i.e. with intensive centre of mass infinitesimally close (in the thermodynamic limit) to the middle of the chain, one gets

$$\frac{1}{L}\ln D_{N,X}^{(d)}(L) = \eta_d(\nu) + o(L^0) \qquad\qquad \nu_{x_0} = o(L^0)\ . \tag{3.12}$$

By comparing with Eq. (3.9) we see that families characterized by $\nu_{x_0} = o(L^0)$ are *typical*, i.e. together they contain a fraction that tends to 1 exponentially with L of all the configurations in the chosen $N = \nu L$ sector.

Another important property needed in the following is related to “spatial” typicality, which is a natural consequence of the strict concavity of $\eta_d(\nu)$:

Typical states in a given family of $N = \nu L$ sectors are homogeneous over extensive length scales, i.e. the “local” filling of any extensive subregion equals the global ν.

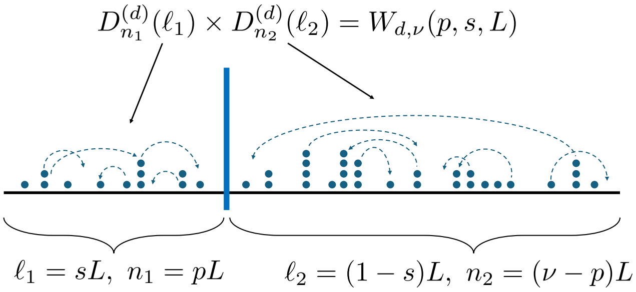

Figure 3.4: Example of a bipartition of the chain with L sites and $N = \nu L$ particles. $W_{d,\nu}$ indicates the total number of configurations compatible with it, i.e. the number of different configurations on the chain that can be reached by rearranging particles within each subregion (without exchanges of particles between the two).

This is nothing but the familiar[10] combinatorial property that homogeneous arrangements dominate in number the configuration space. To formalize this, consider a system of length L and $N = \nu L$ particles, and imagine to introduce a bipartition of the chain such that one of the two subregions contains sL sites and pL particles, with $0 < s < 1$. We are interested in the total number $W_{d,\nu}(p,s,L)$ of different particle configurations compatible with such a bipartition, see Fig. 3.4 for a schematic illustration. We can extract the asymptotic dependence of $W_{d,\nu}(p,s,L)$ directly from (3.9), which yields

$$\begin{aligned} g_{d,\nu}(p,s) &= \lim_{L\to\infty} \frac{1}{L} \ln W_{d,\nu}(p,s,L) \\ &= s\,\eta_d\left(\frac{p}{s}\right) + (1-s)\,\eta_d\left(\frac{\nu-p}{1-s}\right) \ . \end{aligned} \tag{3.13}$$

It then easily follows from the strict concavity of η_d that

$$g_{d,\nu}(p,s) < \eta_d(\nu) \qquad \forall\ p \neq p^* \ , \tag{3.14}$$

where $p^* = \nu\, s$ is the unique global maximum of $g_{d,\nu}$, as a consequence of the identity $g_{d,\nu}(p^*,s) = \eta_d(\nu)$. As there are only $\mathcal{O}(L)$ ways to distribute the total number of particles $N = \nu L$ between the two subregions (i.e. to choose p once s is fixed), we see by comparing (3.14) with (3.9) that “homogeneous” configurations in which both subregions have local filling equal to the global ν are typical, i.e. their number exponentially dominates (with L) over all other configurations in the $N = \nu L$

---

[10] To any physicist, since the work of Boltzmann on the microscopic definition of entropy.

sector[11]. Note that this spatial typicality condition is consistent with the typicality of (N, X) sectors with vanishingly small ν_{x_0}.

3.4.2 Warm-up: strong fragmentation for $\nu < (k-1)^{-1}$

Despite our goal being the proof that the entire region $\nu < \nu_c = (k-2)^{-1}$ is strongly fragmented, it is instructive to consider first the proof of the same statement for the restricted region $\nu < (k-1)^{-1}$. This is the simplest case, as a consequence of the *necessary* presence of an extensive number of frozen sites.

Consider a chain S with $2 \leq d \leq \infty$ and global filling $\nu < (k-1)^{-1}$. Starting from any configuration of particles on the chain, we can employ the FES picture of Section 3.3.2 and reach an FES in the auxiliary system $\tilde{S}$. Let f denote the fraction of sites in the chosen Krylov sector of S that are part of a frozen blockage. Given the current upper bound on ν, we automatically know from the FES picture that

$$f \geq 1 - \nu(k-1) > 0 \; . \tag{3.15}$$

This lower bound is obtained by noticing that in the FES of $\tilde{S}$ the lowest number of sites involved in a type-1 blockage is obtained when each one of the N particles is separated from its neighbours by exactly $k-2$ holes. This implies that *at most* a fraction $\nu(k-2+1)$ of all sites is not part of a type-1 blockage, leading to (3.15). We now prove that as a consequence of Eq. (3.15), any typical (N, X) family (see previous Section 3.4.1) in S is strongly fragmented according to the ratio test in Eq. (3.7). Indeed, for any typical (N, X) family, the exponential scaling of $D^{(d)}_{N,X}$ is given by Eq. (3.12). On the other hand, the $f\,L$ empty frozen sites induce a natural bipartition of the chain in which they represent one (possibly non-contiguous) of two independent subregions that cannot exchange particles or dipole moment. By construction, the total number $W_{d,\nu}(p = 0, s = f, L)$ of particle configurations (of

---

[11] We note that it is straightforward to generalize this argument to the case in which we partition the system into any $G = \mathcal{O}(L^0)$ number of extensively large subregions of size $s_i L$, with $s_1 + \ldots + s_G = 1$.

any dipole moment) compatible with this bipartition (see Fig. 3.4) is larger than the dimension of any Krylov subspace in the chosen (N, X) sector, i.e.

$$\mathcal{D}_{\max}^{(d,k)}(N, X) < W_{d,\nu}(p = 0, s = f, L) \ . \tag{3.16}$$

From the uniqueness of the maximum p^* of $g_{d,\nu}(p, s)$ discussed in Section 3.4.1 and the fact that here $p = 0 \neq \nu f = p^*$, we automatically see that

$$\lim_{L\to\infty} \frac{1}{L} \ln r_{N,X}^{(d,k)} \leq g_{d,\nu}(0, f) - \eta_d(\nu) < 0 \ . \tag{3.17}$$

This proves, for any d, that all the (N, X) families characterized by $\nu < (k-1)^{-1}$ and $\nu_{x_0} = o(L^0)$ (typical) are strongly fragmented according to the ratio test (3.7), given that $r_{N,X}^{(d,k)}$ decays to zero exponentially with L. We note that Eq. (3.15) also trivially proves that the average density of frozen sites $\overline{\rho}_F^{(d,k)}$ from Eq. (3.8) is nonzero for fillings $\nu < (k-1)^{-1} < \nu_c$.

3.4.3 The full proof

We now conclude the full proof by addressing the interval $(k-1)^{-1} \leq \nu < (k-2)^{-1} = \nu_c$, to which we will refer as $\mathcal{C}_{k-2}$. The crucial difference with respect to the ν region discussed in the previous subsection is that in $\mathcal{C}_{k-2}$ it is possible to have Krylov sectors hosting no frozen sites.

Similarly to before, to prove strong fragmentation in $\mathcal{C}_{k-2}$ it is *not* necessary to understand the specific features of the largest Krylov subspaces in a given family of (N, X) sectors, i.e. the one entering the definition (3.6) of $r_{N,X}^{(d,k)}$. Our strategy is once again simpler: we aim to show that for any $\nu \in \mathcal{C}_{k-2}$, the largest Krylov sectors occupy, *irrespective of their characteristics*, an exponentially vanishing fraction of their corresponding symmetry sectors (N, X).

We start by noticing that in $\mathcal{C}_{k-2}$ there still exist exponentially many FESs of the auxiliary chain $\tilde{S}$ that possess a non-vanishing fraction $f > 0$ of frozen sites that are part of a type-1 blockage. This leads us to

Case 1: The largest Krylov subspaces within a typical family of (N, X) sectors in S possess a nonzero fraction f of frozen sites that are part of a type-1 blockage.

By reasoning identical to the previous subsection we see that, in Case 1, $r_{N,X}^{(d,k)}$ is exponentially suppressed in L.

Now we turn to the scenario in which $f = 0$, which is possible because the inequality (3.15) does not hold in $\mathcal{C}_{k-2}$. Assume that, in addition to $f = 0$, there are no particles stacked on the two boundary sites of the FES of $\tilde{S}$ to which the Krylov subspace of S in question is connected (by the FES picture). If we call ρ_2 and ρ_3 the densities of particles that are separated from the next closest particle to their right by $k-2$ and $k-3$ holes respectively, then in the thermodynamic limit we have

$$\rho_2 + \rho_3 = \nu \qquad \rho_2(k-1) + \rho_3(k-2) = 1 \ , \tag{3.18}$$

from which we find

$$\rho_2 = 1 - \nu(k-2) \qquad \rho_3 = \nu(k-1) - 1 \ . \tag{3.19}$$

This proves that for fillings ν within $\mathcal{C}_{k-2}$, one has $\rho_2 > 0$ and $\rho_3 \geq 0$. If we keep $f = 0$ but allow stacking of particles at the two boundary sites, then ρ_2 necessarily increases with respect to the case (3.19) with no stacking. This means that every Krylov sector with $f = 0$ must possess an extensive number of type-2 edges, and thus, of type-2 blockages. Given the $\mathcal{O}(L)$ number of possible choices to select one, we can always pick a type-2 blockage ($\mathcal{B}$) of L-independent size such that the regions to its left ($\mathcal{A}_1$) and right ($\mathcal{A}_2$), up to the boundaries, are both extensively large. Given that $\mathcal{A}_1$ and $\mathcal{A}_2$ are prevented from exchanging particles and dipole moment (by definition of blockage), we can upper bound the dimension of the largest Krylov sector as

$$\mathcal{D}_{\max}^{(d,k)}(N,X) < D^{(d)}_{N_{\mathcal{A}_1+\mathcal{B}},X_{\mathcal{A}_1+\mathcal{B}}} \, D^{(d)}_{N_{\mathcal{A}_2+\mathcal{B}},X_{\mathcal{A}_2+\mathcal{B}}} \ . \tag{3.20}$$

Note that on the right-hand side of the previous inequality the blockage is joined both to $\mathcal{A}_1$ and $\mathcal{A}_2$. To obtain an expression that avoids this doubling of $\mathcal{B}$, we notice that starting from a chain with L sites and N particles that possesses $D_N^{(d)}$ configurations, if we add to it $\ell = \mathcal{O}(L^0)$ sites which contain $n = \mathcal{O}(L^0)$ particles, then $\lim_{L\to\infty} D^{(d)}_{N+n}(L+\ell)/D^{(d)}_N(L)$ is a finite $O(L^0)$ number, as seen by applying Eq. (3.9). The same is true when we consider the sizes $D^{(d)}_{N,X}(L)$ of (N,X) sectors. This implies that there always exists an L-independent constant Q such that from Eq. (3.20) we can arrive to

$$\mathcal{D}^{(d,k)}_{\max}(N,X) < Q\, D^{(d)}_{N_{\mathcal{A}_1+\mathcal{B}},X_{\mathcal{A}_1+\mathcal{B}}}\, D^{(d)}_{N_{\mathcal{A}_2},X_{\mathcal{A}_2}}\ , \tag{3.21}$$

in which the doubling has been removed. From this we can consider

Case 2: The largest Krylov subspaces within a typical family of (N,X) sectors have $f=0$, and the regions $\mathcal{A}_1+\mathcal{B}$ and $\mathcal{A}_2$ can be chosen in such a way that their local filling is different from ν in the limit of large L.

Remembering that extensive subregions with "local" filling different from the global one can characterize only atypical states (see Section 3.4.1), similarly to the steps that led to (3.17) we can use (3.14) (together with (3.12) for the denominator in $r^{(d,k)}_{N,X}$) to obtain again that $\lim_{L\to\infty}\ln r^{(d,k)}_{N,X}/L<0$, i.e. $r^{(d,k)}_{N,X}$ decays exponentially with L also in Case 2.

Let's now consider the final scenario, given by

Case 3: The largest Krylov subspaces within a typical family of (N,X) sectors have $f=0$, but the "inhomogeneous" assumption on $\mathcal{A}_1+\mathcal{B}$ and $\mathcal{A}_2$ of Case 2 does not hold.

Case 3 implies that any extensive subregion of the chain has "local" filling approaching the global ν for large L values. As we show in Appendix B.2, this provides us with an algorithm to partition the system into an *extensive* number G of subregions $\mathcal{A}_i$ that are separated by type-2 blockages $\mathcal{B}_i$ of L-independent size, as pictured in Fig. 3.5. The length ℓ_i of each subregion $\mathcal{A}_i$ is guaranteed to be subextensive. Given such a partition of the chain, and given the disconnecting effect induced by type-2 blockages $\mathcal{B}_i$, one arrives at the inequality (see Appendix B.2)

$$r^{(d,k)}_{N,X} < L^2\prod_{i=1}^{G}\frac{\widetilde{Q}}{\ell_i^2}\ . \tag{3.22}$$

Here $\widetilde{Q}$ is an L-independent positive constant such that $\widetilde{Q}<\ell_i^2\ \ \forall\ i$. Given that $G=\mathcal{O}(L)$, Eq. (3.22) shows that also in Case 3 the ratio $r^{(d,k)}_{N,X}$ decays exponentially

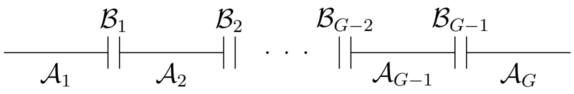

Figure 3.5: Partition of the chain into contiguous subregions ($\mathcal{A}_i$) separated by type-2 blockages of L-independent size ($\mathcal{B}_i$). Each vertical line represents a type-2 edge.

with L, hence concluding the proof.

A few remarks are in order. For a brief discussion of the fate of strong fragmentation in *atypical* families of (N, X) sectors, i.e. those with a centre of mass significantly far from the centre of the chain, we refer to Appendix E of our original work [2].

In [2] it is also proved for $d = 2$ and $d = \infty$ that *typical* states in a given $N = \nu L$ sector with $\nu < \nu_c$ host an extensive number of type-1 blockages. In the language of this section this implies that Krylov sectors with $f = 0$ are vanishingly rare. Therefore, if one could easily prove the same for any d (which we believe to be true), then the previous proof of strong fragmentation[12] could be limited to the case of $f > 0$, which we have seen to be trivial.

Finally, we remark that even if the assumption of gate-completeness from Section 3.2.1 does not hold, our results still prove that $r_{N,X}^{(d,k)}$ decays to zero exponentially with L in typical symmetry sectors for $\nu < \nu_c$, and hence that these sectors are strongly fragmented. This is a trivial consequence of the fact that violations of gate-completeness further suppress dynamics and reduce the connectivity in the system, and hence all the blockages identified by our method remain such.

3.5 Critical exponents, entanglement entropy and weak fragmentation

In this section we present additional analytical results, as well as numerical evidence, concerning both the strongly and weakly fragmented phases. For example, we

---

[12] According to the ratio test in Eq. (3.7).

derive the scaling with $(\nu_c - \nu)$ of the total number of blockages in the strongly fragmented phase, and thoroughly discuss the EE of eigenstates. Our findings constitute significant additional evidence for the phase diagram of Fig. 3.1.

3.5.1 Critical scaling for the number of blockages

The discussion in this subsection implicitly addresses models that possess a weakly fragmented phase (and hence a transition), i.e. we exclude the special cases $d = 3, k = 3$ and $d = 2, k = 4$. These coincide with the only two choices of the pair (d, k) for which the lower phase transition point $\nu_c = (k-2)^{-1}$ and the upper one $d - 1 - \nu_c$ (by particle-hole symmetry) coincide, and hence these models do not possess a weakly fragmented phase. This fact is tightly related to the existence, for such (d, k) pairs, of *absolute blockages* [2, 109].

Consider a typical state[13] at $\nu < \nu_c$ for any d, and apply the FES picture to it. Let $\rho_{1,\ell}$ designate the density of particles in the FES that have to their right a type-1 blockage of length ℓ, i.e. exactly ℓ holes before the next particle. Similarly, let ρ_2 indicate the density of particles that have to their right a type-2 edge (i.e. exactly $k-2$ holes before the next particle) and ρ_3 the density of particles that have to their right exactly $k-3$ holes. Clearly, ρ_2 coincides with the total density of type-2 edges. Similarly, the sum over ℓ of $\rho_{1,\ell}$ coincides with the total density of type-1 blockages, i.e. $\rho_1 = \sum_\ell \rho_{1,\ell}$.

Given that in the following we consider only intensive quantities, we can ignore the presence of possible stacks of particles at the boundaries. Indeed, for typical states such stacks can host at most a subextensive number of particles for $\nu < \nu_c$ (by reasoning identical to the one employed in the partitioning algorithm in Appendix B.2, see also [2]). We hence obtain in the limit of large L

$$\rho_3 + \rho_2 + \sum_{\ell=k-1}^{\ell_{\max}} \rho_{1,\ell} = \nu \tag{3.23}$$

$$(k-2)\rho_3 + (k-1)\rho_2 + \sum_{\ell=k-1}^{\ell_{\max}} (\ell+1)\rho_{1,\ell} = 1 \ . \tag{3.24}$$

---

[13] Remember that, as proved in Section 3.4.1, any extensive subregion of a typical states has "local" filling equal to the global ν.

In principle ℓ_{max} can grow with L (subextensively, given our restriction in considering only typical states). However, at any nonzero ν type-1 blockages with $\ell = \mathcal{O}(L^{\gamma})$ and $0 < \gamma < 1$ are extremely unlikely to arise[14]. This means that for any nonzero ν there exists a large but finite[15] cutoff length $\ell_{\text{cut}} = \mathcal{O}(L^0)$ such that $\sum_{\ell=\ell_{\text{cut}}+1}^{\ell_{\text{max}}} \ell\, \rho_{1,\ell} \ll 1$ for any large size L. Combining (3.23) and (3.24), and neglecting the vanishingly small error in replacing ℓ_{max} with ℓ_{cut}, we obtain

$$\rho_2 + \sum_{\ell=k-1}^{\ell_{\text{cut}}} (\ell - k + 3)\rho_{1,\ell} = \frac{1}{\nu_c}(\nu_c - \nu) \ , \tag{3.25}$$

where we have used $\nu_c = (k-2)^{-1}$. From (3.25) it is straightforward to obtain the following inequalities

$$\frac{(\nu_c - \nu)}{\ell_{\text{cut}}\, \nu_c} < \rho_2 + \sum_{\ell=k-1}^{\ell_{\text{cut}}} \rho_{1,\ell} < \frac{(\nu_c - \nu)}{\nu_c} \ . \tag{3.26}$$

Given the finiteness of ℓ_{cut}, we obtain from (3.26)

$$\rho_2 + \rho_1 \propto (\nu_c - \nu) \ . \tag{3.27}$$

It is our expectation that the previous scaling applies separately to the two terms, i.e.

$$\rho_t \propto (\nu_c - \nu)^{\beta} \qquad \beta = 1, \qquad\quad t = 1, 2 \ . \tag{3.28}$$

We confirm this numerically in Section 3.5.3 (see the linear dependence in Fig. 3.7(c) for ν close to ν_c). Notice that from the scaling of ρ_1 and the finiteness of ℓ_{cut} we also obtain $\rho_F \propto (\nu_c - \nu)^{\beta}$ with $\beta = 1$, where ρ_F denotes the density of frozen sites. For $d = \infty$ this follows from the fact that type-1 blockages are the only source of frozen sites (notice that a single particle enclosed by two type-1 blockages represents a frozen site too), while at finite d they are expected to represent the largest source by far[16]. The value of $\beta = 1$ agrees with the one suggested for the density of frozen

---

[14] Instead of the typicality class characterised by homogeneity over extensive length scales, one can consider smaller but still dominant classes of states that have local filling equal to the global ν over any region of length $\mathcal{O}(L^{\gamma})$, for a given $0 < \gamma < 1$.

[15] This finiteness is crucial because to arrive to Eq. (3.26) we will need to divide for a length that doesn't diverge in the thermodynamic limit.

[16] Indeed, other types of frozen sites can only emerge from the additional constraints due to the maximal on-site occupation of $d - 1$. However, at the low fillings $\nu < \nu_c = (k-2)^{-1}$ we are considering, these constraints are not expected to play any major role.

sites in [225] on the basis of numerical evidence and heuristic arguments. Note that in Section VIIA of [2] I also derived the critical scaling for the average length of active subregions[17] and of a related characteristic length scale ξ.

3.5.2 Entanglement entropy and quantum dynamics in the strongly fragmented phase

As already mentioned, in [2] it is proved for $d = 2$ and ∞ that type-1 blockages are extensively present in typical states at any $\nu < \nu_c = (k-2)^{-1}$ (note that in Section 3.4 we only proved this for $\nu < (k-1)^{-1}$, although for any d). We numerically show that the same is true for other finite d values in Section 3.5.3. Also, typically these type-1 blockages are quite uniformly distributed along the chain (see analytical proof in [2], based on the same type of partitioning algorithm used in Appendix B.2, or numerical evidence in Figs. 3.7(d)-(e) from Section 3.5.3). On the basis of this, in this subsection we demonstrate that typical eigenstates in the strongly fragmented phase feature an area law for EE, and discuss further consequences for quantum dynamics. On the other hand, we will see that contrary to frozen blockages, type-2 blockages allow the exchange of some amount of quantum information between the two regions that they disconnect from the point of view of transport (of particles and dipole moment). This is because these regions can both interact with the active type-2 blockage, as described in Section 3.3.1. This is the mechanism behind an "inverse quantum many-body scar" phenomenon that we conjecture, based on the existence of rare eigenstates which possess beyond-area-law EE scaling.

Type-1 blockages

As discussed in Chapter 1, in both quantum chaotic and integrable models eigenstates at a finite energy density above the ground state possess volume-law EE

$$S_A = -\mathrm{Tr}_A(\rho_A \ln \rho_A) \propto |A| \ , \tag{3.29}$$

---

[17] Here "active" refers to the fact that these subregions host no type-1 blockage.

where A is a subsystem of size $|A|$, B its complement, $\rho_A = \mathrm{Tr}_B(|E_i\rangle\langle E_i|)$ and $|E_i\rangle$ an eigenstate at energy E_i. We now show that the EE of typical eigenstates in N-sectors characterized by $\nu < \nu_c$ follows instead an *area law*.

The bipartite EE of each eigenstate within the i-th Krylov sector of an (N, X) sector can be upper bounded by $\ln \mathcal{D}_i^{(d,k)}(A)$, where $\mathcal{D}_i^{(d,k)}(A)$ is the dimension of the Krylov sector restricted to the subsystem A of the bipartition [85, 109, 230], where we are assuming $\mathcal{D}_i^{(d,k)}(A) \leq \mathcal{D}_i^{(d,k)}(B)$. In particular, this ensures that *all* eigenstates of strongly fragmented (N, X) families have EE density s upper bounded in the thermodynamic limit by

$$s \leq \lim_{L\to\infty} \frac{1}{L} \ln \mathcal{D}_{\max}^{(d,k)} < \lim_{L\to\infty} \frac{1}{L} \ln D_{N,X}^{(d)} \ . \tag{3.30}$$

In quantum chaotic models, the rightmost term in the previous inequality would be expected to coincide with the EE density of highest-DoS eigenstates (i.e. typical ones) in the chosen family of (N, X) sectors (see works on generalizations of Page formula [231, 232] to symmetry sectors [44, 233]). Thus, the inequality in Eq. (3.30) proves ergodicity breaking at the level of entanglement on the basis of the exponential suppression of the dimension of Krylov sectors compared to the dimension of symmetry sectors. However, given that usually $\mathcal{D}_{\max}^{(d,k)}$ scales exponentially with L, the inequality in (3.30) remains compatible with volume-law EE scaling in the strongly fragmented phase. It has been first remarked in Ref. [109] that further restrictions on the generation of entanglement can arise from local configurations that completely disconnect the regions of the chain to their left and right. In [109] these disconnections coincided with "absolute blockages" (using the language of [2]), which exist only in the special models with $d = 2, k = 4$ and $d = 3, k = 3$, which are strongly fragmented irrespective of the filling ν. Armed with the more general concept of type-1 blockages introduced in Section 3.3.1, we now generalise this idea to models with any d and k.

Consider a Krylov sector $\mathcal{K}$ that contains a type-1 blockage somewhere along the chain. By the definition of Krylov sectors, the Hamiltonian leaves the vector space $\mathcal{K}$ invariant, i.e. $H\mathcal{K} \subseteq \mathcal{K}$. Call $H_{\mathcal{K}}$ the restriction of H to $\mathcal{K}$. Imagine now to partition the chain by inserting a cut somewhere in the middle of the type-1 blockage, and obtain in this way two subregions α and β. By definition of type-1 blockages we have

$$H_{\mathcal{K}} = H_\alpha \otimes \mathbb{I}_\beta + \mathbb{I}_\alpha \otimes H_\beta \ , \tag{3.31}$$

where $\mathbb{I}$ represents the identity operator and H_α, H_β are Hermitian operators. From (3.31) we see that the eigenstates of $H_{\mathcal{K}}$, which form a basis of $\mathcal{K}$, have the form

$$|n, m\rangle = |n\rangle_\alpha \otimes |m\rangle_\beta \ , \tag{3.32}$$

where $|n\rangle_\alpha$ and $|m\rangle_\beta$ are eigenstates of respectively H_α and H_β. More generally, if a Krylov sector contains several type-1 blockages which partition the system into G regions α_i, then all its eigenstates can be expressed as product states of active regions enclosed by the type-1 blockages $|n_1, \ldots, n_G\rangle = |n_1\rangle_{\alpha_1} \otimes \ldots \otimes |n_G\rangle_{\alpha_G}$. From this "separable" structure of the eigenstates we trivially derive the following results:

1. The bipartite EE associated with a single entanglement cut located within a type-1 blockage is exactly zero.

2. The bipartite EE associated with a single entanglement cut that has to its left or right a type-1 blockage is upper bounded by $\ln \mathcal{D}^*$, where $\mathcal{D}^*$ is the dimension of the Krylov sector restricted to the subregion enclosed by the entanglement cut and the type-1 blockage. We notice that for any such subregion of size ℓ, $\ln \mathcal{D}^* \leq \ell \ln d$.

The previous statements trivially generalise to the case in which the entanglement bipartition arises from two entanglement cuts. Given the extensive presence of type-1 blockages, and their fair uniformity, in typical Krylov sectors for $\nu < \nu_c$ (discussed above), we conclude that typical eigenstates in the strongly fragmented phase possess area-law EE[18].

More generally, the decomposition in Eq. (3.31) and the finite density of uniformly distributed type-1 blockages imply that, in the strongly fragmented phase, quantum unitary dynamics[19] can be typically resolved into the independent action of extensively many ultralocal Hamiltonians on regions of L-independent

---

[18] E.g. the bipartite EE with single entanglement cut does not grow with L as the latter is increased to infinity.

[19] For example starting from a product state belonging to a strongly fragmented (N, X) sector.

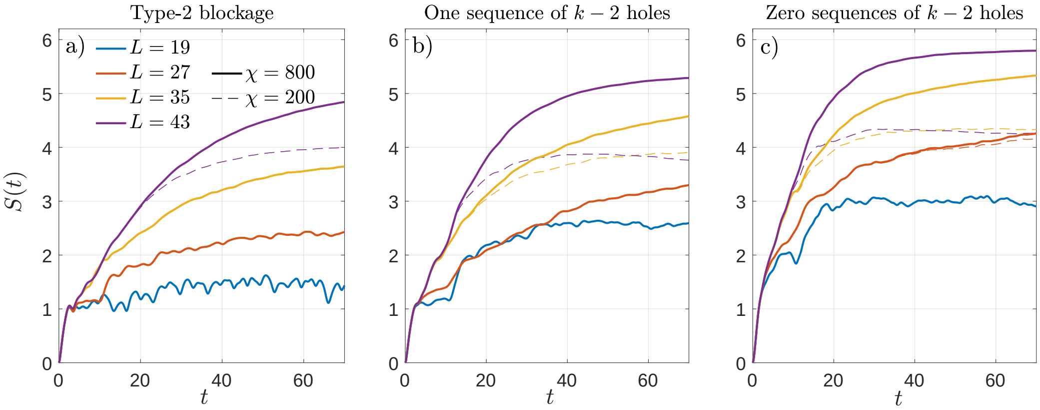

Figure 3.6: Time-dependence of the bipartite von Neumann entropy $S(t)$ under Hamiltonian dynamics computed using tDMRG. The Hamiltonian is characterised by $d = 2$, $k = 6$ and the initial product state is chosen among the set of configurations discussed in Section 3.5.2, for various system sizes L. We report results for bond dimensions $\chi = 200$ and 800. (a) Local disturbance coinciding with the simplest kind of type-2 blockage. (b) Local disturbance represented by a single sequence of $k-2$ holes (no blockage). (c) No disturbance.

size. In other words, the quantum many-body problem is transformed into a set of extensively many independent *few-body* problems. The consequences of this range from eigenstate expectation values of local operators strongly deviating from the ETH prediction (Section 1.2), to entanglement growth by quench dynamics (e.g. starting from a simple product state) saturating to an area-law value, and to the possible presence of long-lived oscillations in the dynamics of local observables[20].

We remark that such conclusions do not hold if one considers eigenstates in weakly fragmented sectors, or dynamics starting from product states that belong to them, due to the typical absence of type-1 blockages in such cases.

Type-2 blockages and inverse quantum many-body scars

We now consider the effect of type-2 blockages on the EE, which turns out *not* to be as drastic as the one of type-1 blockages. Given that type-2 blockages prevent transport of particles and dipole moment between the regions to their left and right, their presence along the chain typically reduces the value of $\ln \mathcal{D}_i^{(d,k)}(A)$ discussed in the previous subsection, thus lowering the maximal eigenstate EE reachable

---

[20] The emergence of long-lived oscillations in this context has a different nature compared to that due to QMBS [84] or other known mechanisms (see, e.g., [179]).

in principle through a bipartition into A and B. This is however only a weak suppression of EE generation compared to the strong disconnecting effect of type-1 blockages, and it is compatible with volume-law EE scaling. One might wonder whether any type of strong suppression, similar to type-1 blockages, is produced also by active blockages. However, due to the possibility of the regions to the left and right of a type-2 blockage interacting with the particles involved in the blockage, these active blockages are not in principle expected to fully block the generation of entanglement. This is verified numerically in Fig. 3.6 for $d = 2$, using tDMRG [234] (see also [67] and references therein). We consider a chain of length L in an FES, in which the boundary sites are occupied and particles are separated by exactly $k - 3$ holes, with the only exception of a local disturbance in the middle of the chain. This is chosen to be a type-2 blockage formed by two type-2 edges separated by just one particle.

$$\underline{\bullet}\;\underset{k-3}{\underline{\ \ }\ldots\underline{\ \ }}\;\underline{\bullet}\ldots\underline{\bullet}\;\underset{k-3}{\underline{\ \ }\ldots\underline{\ \ }}\;\underline{\bullet}\;\underset{k-2}{\underline{\ \ }\ldots\underline{\ \ }}\;\underline{\bullet}\;\underset{k-2}{\underline{\ \ }\ldots\underline{\ \ }}\;\underline{\bullet}\;\underset{k-3}{\underline{\ \ }\ldots\underline{\ \ }}\;\underline{\bullet}\ldots\underline{\bullet}\;\underset{k-3}{\underline{\ \ }\ldots\underline{\ \ }}\;\underline{\bullet}$$

We focus on quantum Hamiltonian dynamics, with H from Eq. (3.3) characterized by $d = 2$ and $k = 6$, for which we choose $\{\hat{h}_j^{(k)}\}$ to represent a gate-complete set as defined in Section 3.2.1. We place the entanglement cut somewhere within the type-2 blockage and calculate the von Neumann entropy $S(t)$ as a function of time. From Fig. 3.6(a) we see that $S(t)$ is different from zero and becomes larger as L is increased. This must be contrasted with the case in which the local disturbance is a type-1 blockage with entanglement cut within it, for which $S(t) = 0 \; \forall \; t, \forall \; L$. In Fig. 3.6(b) and 3.6(c) we produce the same kind of dynamics but replacing the type-2 blockage with, respectively, a single sequence of $k - 2$ holes and no sequence of $k - 2$ holes, as these do not give rise to blockages of any kind. These plots show a very similar evolution for $S(t)$ compared to the type-2 blockage case, confirming that the latter does not lead to any absolute hindrance to the generation of EE. Similar conclusions are reached if one places the entanglement cut just to the left or just to the right of the disturbance. This supports the claim that the bipartite

EE with entanglement cut lying in a subregion A that hosts active blockages but no type-1 blockages can have a dependence on the size of A.

We remark that in the entire phase $\nu < \nu_c$ there exist *atypical* Krylov sectors that contain extensively large "connected" subregions devoid of type-1 and type-2 blockages. These can give rise to eigenstates with volume-law EE, if the entanglement cuts lie within one of these subregions. Given the numerical evidence just presented, even more interesting are the rare Krylov sectors in the interval $(k-1)^{-1} \leq \nu \leq \nu_c$ (see Section 3.4.3) which possess an extensive number of type-2 blockages uniformly distributed along the chain, but no type-1 blockages. Our tDMRG results suggest that the EE of their eigenstates scales beyond any area law, irrespective of the entanglement cut's location. This phenomenon of rare eigenstates with beyond-area-law EE, embedded in a sea of area-law eigenstates, could be interpreted as inverse QMBS [235–238].

3.5.3 Numerical results for strong and weak fragmentation

In this subsection we provide numerical results supporting the claim that, for any d, typical states in the strongly fragmented phase host an extensive number of *both* type-1 blockages and type-2 edges, which are fairly uniformly distributed along the chain. This is analytically demonstrated in [2] for $d = 2$ and ∞. We also show that blockages become vanishingly rare as soon as $\nu > \nu_c$, and for $d = \infty$ we discuss evidence of weak fragmentation according to the ratio test in Eq. (3.7). In [2] weak fragmentation is addressed numerically also for finite d.

We numerically determine the total number n_t of type-1 blockages ($t = 1$) and type-2 edges ($t = 2$) associated with a given state by using the FES picture from Section 3.3.2, i.e. by mapping a state of a finite-d system S to its associated FES in the $\tilde{d} = \infty$ auxiliary system $\tilde{S}$. We also record their location along the chain. From a computational point of view the FES mapping is an easy task, given that it only involves applications of outward hops in $\tilde{S}$ (in no particular order) until no further hops can be applied (see Section 3.3.1). However, to easily address large system sizes of the order of 10^5 sites, we employ a more advanced algorithm developed in [2] by J. Classen-Howes, which allows us to perform the FES mapping even more efficiently.

In Fig. 3.7(a)-(c) we plot numerical results for the average densities $\overline{\rho}_1^{(d,k)} = \langle n_1 \rangle / L$ of type-1 blockages and $\overline{\rho}_2^{(d,k)} = \langle n_2 \rangle / L$ of type-2 edges[21]. These results were obtained by uniformly sampling states in a given N sector[22] (in accordance with the on-site dimension d) and identifying blockages in each of them by the procedure outlined above. In Fig. 3.7(a), where the system is in its strongly fragmented phase given that $\nu < \nu_c$, we see that for various values of d the average densities tend to a constant with increasing L. Importantly, both type-1 blockages and type-2 edges are simultaneously present, in an extensive number, in each of the states sampled. In Figs. 3.7(d)-(e) we present the spatial distribution of type-1 blockages along the chain for two randomly generated states at large L, with particle densities $\nu < \nu_c$ and $d = 2$ and 4. As anticipated, the distribution of blockages is seen to be quite homogeneous along the entire chain. This was found to be the case for all other randomly generated states tested, and the spatial distribution of type-2 edges was also found to be generally uniform.

In Fig. 3.7(b) type-1 blockages and type-2 edges are seen to become vanishingly rare with increasing L for $\nu > \nu_c$, which is consistent with the onset of the weakly fragmented phase. Indeed, as anticipated in Section 3.3.3, the analytic results of Section 3.4 imply for any d that a necessary condition for a Krylov sector to be dominant (and hence for the weakly fragmented phase to arise) is that any state in the Krylov sector must be mapped by the FES picture to the unique blockage-free FES present in the corresponding (N, X) sector. Indeed, even the presence of a single blockage in the bulk of the chain leads to a zero ratio $r_{N,X}^{(d,k)}$ for $L \to \infty$ (*cf.* Appendix B.2). In this regard, the data in Fig. 3.7(b), together with several other tests performed (see [2]), show that typical randomly drawn states for any d are mapped by the FES picture to an FES with $n_1 = 0$ and $n_2 \leq 1$, i.e. to the unique blockage-free FES compatible with the chosen values of N, X and L.

---

[21] Compared to Section 3.5.1 we are now making the d and k dependence explicit.

[22] These states were found to have vanishingly small intensive centres of mass ν_{x_0}, as expected for typical states.

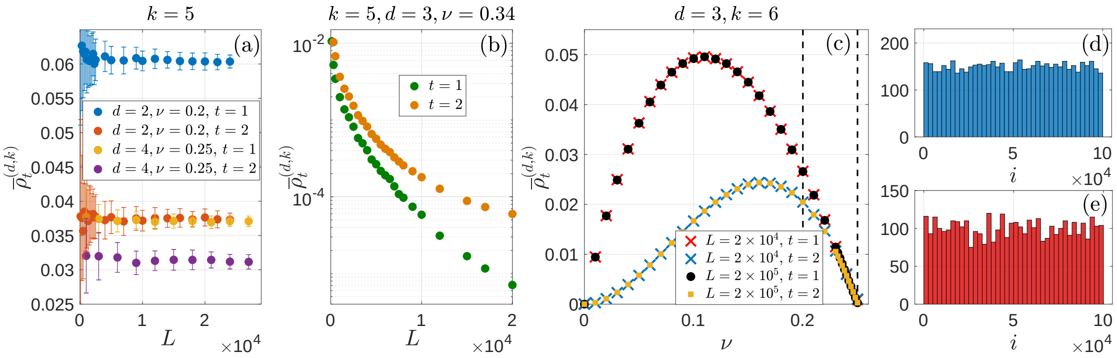

Figure 3.7: (a) Numerical estimates for $\overline{\rho}_t^{(d,k)}$ (from random sampling) as a function of L for 100 randomly generated states with local on-site dimensions $d = 2, 4$, for $k = 5$ and fillings $\nu < \nu_c = 1/3$. The error bars show the standard deviation associated with the set of 100 random states at each L value. (b) $\overline{\rho}_t^{(d,k)}$ as a function of L for 1000 randomly generated states at $\nu = 0.34 > 1/3 = \nu_c$, $k = 5$ and $d = 3$. (c) $\overline{\rho}_t^{(d,k)}$ for $d = 3$, $k = 6$ as a function of $\nu < \nu_c = 0.25$ for $L = 2 \times 10^4$ (1000 randomly generated states) and $L = 2 \times 10^5$ (100 randomly generated states). The leftmost vertical line coincides with $(k-1)^{-1}$ and the rightmost one with $\nu_c = (k-2)^{-1}$. (d) Spatial distribution for $k = 5$ of type-1 blockages in a single randomly drawn state with $L = 10^5$, $d = 2$, $\nu = 0.2 < \nu_c$. Here, $i = 1, \ldots, L$ labels the sites of the chain. The histogram shows the number of type-1 blockages that occurred in each bin, with bin width equal to 250. (e) Analogous histogram for $k = 5$, $L = 10^5$, $d = 4$, $\nu = 0.25 < \nu_c$.

Exceptions to this become rarer and rarer as we increase L at fixed $\nu > \nu_c$, or if at fixed L we increase ν. For example, in the case of $d = 3, k = 5$ from Fig. 3.7(b), if we set ν to a slightly higher value[23], say $\nu = 0.38$, already for $L = 10^3$ all the 1000 randomly sampled states have $n_1 = 0$ and $n_2 \leq 1$. For $d = \infty$, this represents direct numerical evidence of weak fragmentation according to the ratio $r_{N,X}^{(d,k)}$ in Eq. (3.7). Indeed, the fact that in S (identical to $\tilde{S}$ for $d = \infty$) typical states are all mapped to the unique blockage-free FES associated with their (N, X) sector implies that typical symmetry sectors at $\nu > \nu_c$ possess a dominant Krylov subspace (the one containing the blockage-free FES in question) and hence that $r_{N,X}^{(d,k)} \to 1$ for $L \to \infty$. It also implies weak fragmentation from the point of view of the density of frozen sites in Eq. (3.8): in $d = \infty$ systems frozen sites can only arise as a consequence of type-1 blockages[24], and hence $n_1 = 0$ implies absence of frozen sites. Note that while these results are also consistent with the onset of the weakly fragmented phase

---

[23] In Fig. 3.7(b) ν is set to 0.34, which is very close to the critical point $\nu_c = 1/3$ for $k = 5$.

[24] Provided gate-completeness is satisfied.

for d finite, they *do not* represent direct evidence for it. Indeed, for d finite $S \neq \tilde{S}$ and hence a state mapped by the FES picture (dynamics in $\tilde{S}$) to a blockage-free FES might not be actually connected to it by the real dynamics that satisfies the finite d constraint (hence we cannot directly deduce $r_{N,X}^{(d,k)} \to 1$). Similarly, from the point of view of the density of frozen sites, in finite-d systems there can be frozen sites beyond those due to type-1 blockages, as well as blockages invisible to the FES picture (*cf.* Section 3.3.2). These issues are resolved in [2], where proper numerical evidence of weak fragmentation for any $\nu > \nu_c$ and d finite is presented.

In Fig. 3.7(c), we fix L and study $\overline{\rho}_t^{(d,k)}$ as a function of ν. Below ν_c we find $\overline{\rho}_t^{(d,k)}$ to be a smooth positive function that tends to zero linearly as $\nu \to \nu_c$, in accordance with the critical scalings derived in Section 3.5.1. Given that above the critical filling the average density $\overline{\rho}_t^{(d,k)}$ is zero in the thermodynamic limit, the latter is seen to have a discontinuous first derivative with respect to ν at ν_c, signaling a phase transition. We also note that there is no evidence of a discontinuity at $\nu = (k-1)^{-1}$, supporting the claim that even if it becomes possible for densities $\nu > (k-1)^{-1}$ to generate states without type-1 blockages (*cf.* Section 3.4.3), these states are extremely rare and do not lead to an additional thermodynamic phase transition. Note also that $\overline{\rho}_t^{(d,k)}$ has a peak at some finite value of ν, and decreases both for fillings above and below it, as expected[25]. Note that in Section VIIC of [2], to further verify the existence of a universal d-independent strong-to-weak transition at the critical filling $\nu_c = (k-2)^{-1}$, I numerically verified the presence of a critical scaling for $r_{N,X}^{(d,k)}$ at $\nu = \nu_c$. Indeed, at $\nu = \nu_c$ the ratio is expected [226] to decay to zero (unlike the weakly fragmented phase), but only *polynomially* with L (unlike the strongly fragmented phase).

We conclude by stressing that the universality[26] of the critical point $\nu_c = (k-2)^{-1}$ for the strong-to-weak transition relies on the natural assumption of

---

[25] The decrease for fillings below the peak is due to the fact that, e.g., $\overline{\rho}_1^{(d,k)}$ probes only the *number of distinct* type-1 blockages, ignoring their length.

[26] With respect to the on-site dimension d and choice of the interactions couplings entering the dipole-conserving Hamiltonian that governs dynamics.

gate-completeness discussed in Section 3.2.1. It is in principle possible that specific models violating this assumption possess a critical filling higher[27] than $(k-2)^{-1}$, as a consequence of the reduction in connectivity that violations of gate-completeness entail.

3.6 Conclusions

We introduced a number of new approaches for characterising the strongly and weakly Hilbert-space-fragmented phases of charge- and dipole-conserving quantum chains. These allowed us to derive a number of new analytic results concerning these phases and the "freezing" transition between them. Our results lead to the interesting conclusion that dipole-conserving chains have the universal phase diagram depicted in Fig. 3.1, with a critical density of $\nu_c = (k-2)^{-1}$ irrespective of the on-site dimension d or the precise details of the dynamics, as long as the natural assumption of gate-completeness (see Section 3.2.1) holds. We remark that while in this thesis we focused solely on open boundary conditions (OBC), we expect that the main physical conclusions drawn here[28] would also characterize systems with periodic boundary conditions (PBC), see e.g. Ref. [226].

In future work, it would be valuable to generalize our results to lattices in higher spatial dimensions, obtain an analytic understanding of how EE scales in the strongly fragmented phase for states hosting only active blockages (relevant for our conjectured "inverse QMBS"), and uncover whether a strong-to-weak phase transition can be driven by tuning the intensive centre of mass ν_x instead of the filling ν, as briefly discussed in Appendix E of [2].

---

[27] For example, a system with $k=6$ interactions which is only gate-complete at the $k=5$ level may have a phase transition point somewhere in between $\nu = 1/4$ and $\nu = 1/3$ (extremes included, in principle).

[28] Like the location of the phase transition point or the existence of a finite density of blockages in the strongly fragmented phase.

4

Finite-temperature dynamical correlators in the Lieb-Liniger model

4.1 Introduction

In this chapter, we present finite-temperature results for one-body dynamical correlation functions in the one-dimensional Bose gas with point-like interactions [239, 240], known as the Lieb-Liniger model. This field-theory, governed by a single interaction strength c, describes one of the simplest interacting integrable systems solvable by Bethe ansatz [93, 94]. As such, it offers unique possibilities for the exploration of quantum many-body dynamics in an interacting yet (partially) solvable setup, providing both rare insights on the phenomenology of unitary evolution and important benchmarks for approximate methods that aim to tackle quantum chaotic regimes[1]. Approximate experimental realizations of the model have been achieved thanks to the major developments on the control of ultracold quantum gases [242–244], see also the reviews [4, 245]. For these reasons, in the past two decades significant efforts have been devoted to describing the dynamics of the model both in equilibrium [246–261] and during out-of-equilibrium protocols [262–276]. In the presence of interactions, calculating (dynamical) correlation functions is a very hard task even in integrable systems. Analytical results at

---

[1] See, e.g., [241].

finite temperatures, which allow connections to experiments via linear response theory, can be obtained only in a handful of limits: at very low temperatures, Luttinger Liquid (LL) theory (aka bosonization) [277–279] enables description of the low-frequency and long-distance asymptotics of correlation functions, which is governed by low-energy excitations around the edges of a Fermi sea[2] [245, 279, 283, 284] (see also [285]); (static) short-range expansions, valid for the ground state but also capturing low temperatures, can be obtained from integrability methods [286]; in the limit of large c, analytic $1/c$ expansions of dynamical correlation functions at arbitrary temperatures are available [258] (see also [248]); similarly, in the limit of small densities n, expansions in n at any c have been obtained [259]. We also note that some analytic results (like expressions for asymptotic correlation lengths) at arbitrary temperatures, densities and interaction strengths can be obtained for *static* correlators[3] via integrability methods [287].

Away from these asymptotic (or static) limits, i.e. in the experimentally relevant regimes of finite temperatures at arbitrary frequencies, momenta, densities and couplings c, numerical procedures are required. Numerical algorithms that reconstruct dynamical correlators by explicitly summing matrix elements (aka form factors[4]) that appear in Lehmann representations (Chapter 1) have been particularly successful in the context of the Lieb-Liniger gas. In particular, dynamical correlators of the density operator have been determined both at zero [246] and finite temperatures [251] by the ABACUS algorithm [288, 289] (for a fairly large number of particles $N \approx 50$–200, depending on the temperature). For the Bose field, i.e. for one-particle dynamical correlation functions, results have been obtained at zero temperature

---

[2] As we will see, a Fermi sea can arise in one-dimension even in bosonic systems. We notice that certain parameters entering the LL description can be analytically obtained in the repulsive weakly-interacting limit $c \ll 1$ by extending Bogoliubov theory to treat quasicondensates at small temperatures [280]. They are also known from integrability techniques [281, 282] both at $c \ll 1$ and in the hard-core limit $c \gg 1$.

[3] The static results of [287] for the correlation length can be used as an additional benchmark of the numerical scheme presented in this chapter (directly in the interacting regime). We have performed this benchmark and found excellent agreement, but given the focus of this thesis on dynamical correlators, we do not report it here.

[4] These form factors are analytically available in some integrable models, including the Lieb-Liniger gas, for some specific observables.

[249], and very recently extended to very low but nonzero temperatures (for $N \approx 40$–80) [260]. The success of these approaches is surprising at first, given that in general exponentially many (in system size) form factors enter Lehmann sums and hence summation over all of them is a computationally hopeless task. Indeed, the applicability of ABACUS relies on the fact that in the low-temperature limits[5] considered in these works only a significantly smaller number of matrix elements is relevant for the reconstruction of correlation functions.

In this chapter, we consider a regime of temperatures, interaction strengths and number of particles that lies beyond this paradigm, in that the number of relevant form factors for the reconstruction of correlation functions (of the Bose field) is orders of magnitude larger than what can be handled with classical computational resources. Therefore, *sampling* of relevant matrix elements becomes necessary. We present a Monte Carlo sampling scheme based on a probability distribution defined directly in terms of form factors. We note that the idea of sampling with respect to a form-factor (or an eigenstate-overlap) weight previously appeared in Refs. [262, 273, 290–292], in several contexts[6]. However, the evaluation of dynamical finite-temperature correlation functions and the systematic analysis of the accuracy and applicability of such Monte Carlo schemes have not been pursued to date. We obtain the full space and time dependence of the spectral function in the Lieb-Liniger model, and benchmark the method against some exact results available. This enables us to prove the power of the approach, and to explore some physically relevant regimes that cannot be addressed by other methods.

The chapter is organized as follows. In Section 4.2 we review the integrability of the Lieb-Liniger model. In Section 4.3 we describe our sampling method and present results for the one-body dynamical correlator for a wide range of couplings

---

[5] We note that in [251] some temperatures far from $T = 0$ have been addressed for $N \approx 50$–100. This is possible due to some special features of matrix elements of the density operator, as we discuss in depth in Section 4.4.

[6] We also note that other Monte Carlo approaches have been used in the context of integrability and coupled with the Bethe ansatz technology [293–297], but these do not involve sampling of form factors and so are intrinsically different.

and temperatures. In Section 4.4 we explore important consequences stemming from differences between the form factors of the Bose field and the density operator.

4.2 Integrability of the Lieb-Liniger gas

4.2.1 The model

The Lieb-Liniger Hamiltonian describes spinless bosons on a ring (PBC) of length L with contact repulsive interactions. For N bosons, the Hamiltonian $\mathcal{H}$ is given by (in first quantization language)

$$\mathcal{H} = -\sum_{i=1}^{N} \partial_{x_i}^2 + 2\,c \sum_{1\leq i<j\leq N} \delta(x_i - x_j) - h\,N \ , \tag{4.1}$$

where $c > 0$ is the interaction strength of the contact interactions and h is a chemical potential. This model corresponds to the following field theory Hamiltonian

$$H = \int_{-L/2}^{L/2} dx \Big[\phi(x)^\dagger(-\partial_x^2 - h)\phi(x) + c\,\phi^\dagger(x)\phi^\dagger(x)\phi(x)\phi(x)\Big] \ . \tag{4.2}$$

Here $\phi(x)$ is a complex bosonic field obeying the canonical commutation relations $[\phi(x), \phi^\dagger(y)] = \delta(x-y)$ and PBC $\phi(x+L) = \phi(x)$. As becomes evident in the language of the algebraic Bethe ansatz [94, 95], H possesses an extensive number of mutually commuting local charges $Q^{(m)}$, which as discussed in Section 1.3.1 is a hallmark of quantum integrability. These local symmetries include the total number of particles $Q = \int dx\,\phi^\dagger(x)\phi(x)$ and the momentum $P = -i\int dx\,\phi^\dagger(x)\partial_x\phi(x)$. The symmetric eigenfunctions $\chi_N(x_1, \dots, x_N)$ of (4.1) in the $Q = N$ sector can be determined exactly by the coordinate Bethe ansatz [94, 239], and are given by

$$\begin{aligned}\chi_N(x_1,\dots,x_N|\lambda_1,\dots,\lambda_N) &= \frac{\prod_{k<j}(\lambda_j-\lambda_k)}{\sqrt{N!\prod_{k<j}[(\lambda_j-\lambda_k)^2+c^2]}} \\ &\times \sum_{\mathcal{P}} \left\{ \exp\left[i\sum_{j=1}^{N} x_j\,\lambda_{\mathcal{P}_j}\right] \prod_{1\leq k<j\leq N}\left[1 - \frac{i\,c\,\mathrm{sgn}(x_j-x_k)}{\lambda_{\mathcal{P}_j}-\lambda_{\mathcal{P}_k}}\right]\right\} \ ,\end{aligned} \tag{4.3}$$

where sgn(x) is the sign function, $\mathcal{P}$ denotes all the permutations of the integers $1, \dots, N$ and a set of N real "rapidities" $\boldsymbol{\lambda} = (\lambda_1, \dots, \lambda_N)$ appears. The latter can be thought of as a generalization to the interacting integrable context of the momenta appearing in the wavefunction of free particles. We note that χ_N is two-particle reducible[7], which is a distinctive feature of all models solvable by Bethe ansatz. The fact that the rapidities are all real for $c > 0$ is a special simplifying feature of the Lieb-Liniger model, given that in more general integrable systems they take complex values as a consequence of the existence of bound states [95]. Crucially, the wavefunction (4.3) is antisymmetric in the rapidities λ_j, i.e. $\chi_N = 0$ if $\lambda_j = \lambda_k$ for any $j \neq k$. This gives rise to a generalized Pauli principle (despite the fact that we are describing bosons) and has important consequences for the structure of the ground state of the model. By imposing periodic boundary conditions in the positions x_i for the wavefunction χ_N, one obtains the Bethe equations for the Lieb-Liniger model, which in logarithmic form read

$$L\lambda_j + \sum_{k=1}^{N} \theta(\lambda_j - \lambda_k) = 2\pi I_j \qquad j = 1, \ldots, N \ . \tag{4.4}$$

Here $\theta(x) = 2\arctan(x/c)$ and $\{I_j\}$ is a set of *distinct* integers (half-odd integers) for N odd (even). For any given $\{I_j\}$ the solutions $\boldsymbol{\lambda}$ of the Bethe equations are unique, hence the sets $\{I_j\}$ are in one-to-one correspondence with the eigenstates of (4.1), which in Dirac notation we denote simply as $|\lambda\rangle$. The eigenvalues of H and P in the N-sector eigenstate $|\lambda\rangle$ are given by simple expressions in terms of the rapidities λ

$$E_\lambda = \sum_{i=1}^{N} (\lambda_i^2 - h) \qquad\qquad P_\lambda = \sum_{i=1}^{N} \lambda_i \ , \tag{4.5}$$

and similarly for the higher charges $Q^{(m)}$ which involve higher powers of the rapidities, i.e. $Q_\lambda^{(m)} = \sum_i \lambda_i^m$ for $m \geq 3$. We also note that as a consequence of the antisymmetry of $\theta(x)$ in (4.4), the following useful equality holds for the total momentum P_λ in (4.5) at any interaction coupling c

$$P_\lambda = \frac{2\pi}{L} \sum_{i=1}^{N} I_i \ . \tag{4.6}$$

The ground state of the model in the N sector is described by the rapidities $\boldsymbol{\lambda}$ that solve the Bethe equations (4.4) for the following set of (half-odd) integers [94, 239]

$$I_j = -\frac{N-1}{2} + j - 1 \qquad\qquad j = 1, \ldots, N \ . \tag{4.7}$$

---

[7] That is, it is expressed as a sum over permutations of products of terms that involve at most two particles. The origin of this reducibility is the famous Yang-Baxter equation from the algebraic Bethe ansatz.

This corresponds to a Fermi sea in the rapidities λ_j, and emerges as a consequence of the generalized Pauli principle.

We note that no closed-form solution $\boldsymbol{\lambda}$ of the Bethe equations is available given a generic set of (half-odd) integers. In the following, we solve Eq. (4.4) numerically using the Newton–Raphson method, which converges to the solution in very few iterations and is hence extremely efficient.

4.2.2 Macrostates

In the thermodynamic limit $L \to \infty$ ($n = N/L$ fixed) it is convenient to switch from a description in terms of "microstates", i.e. single eigenstates with fixed rapidities $\boldsymbol{\lambda}$, to one in terms of "macrostates" [298]. These represent families of eigenstates with identical coarse-grained distribution $\rho(\lambda)$ of rapidities. The function $\rho(\lambda)$ is known as "root density" and can be defined in the limit of asymptotically large L as

$$L\rho(\lambda)\Delta\lambda = \text{number of rapidities } \ \lambda_j \text{ in } [\lambda, \lambda + \Delta\lambda] \ . \tag{4.8}$$

We say that two eigenstates belong to the same macrostate (for $L \to \infty$) if they possess identical root density. Given that the rapidities λ_j need to satisfy the non-trivial Bethe equations, it is simpler to start by considering the distribution of the (half-odd) integers $\{I_j\}$ that appear in Eq. (4.4), given that these can be arbitrarily chosen. We define the distribution $\tilde{\rho}(z)$ of intensive (half-odd) integers $z_j = I_j/L$ as

$$L\tilde{\rho}(z)\Delta z = \text{number of } \ z_j = \frac{I_j}{L} \ \text{ in } [z, z + \Delta z] \qquad\qquad 0 \leq \tilde{\rho}(z) \leq 1 \ . \tag{4.9}$$

By means of the Bethe equations we can explicitly relate $\tilde{\rho}(z)$ to its associated root density $\rho(\lambda)$. We start by noticing that the rapidities λ_j solving the Bethe equations Eq. (4.4) with (half-odd) integers $\{I_j\}$ follow the same order as the latter, i.e. if $I_i > I_j$ then $\lambda_i > \lambda_j$. Furthermore, λ_i and λ_j cluster together if their associated intensive (half-odd) integers z_i and z_j do, as a consequence of the following inequalities [94]

$$\frac{2\pi}{(1 + 2n/c)}(z_i - z_j) \leq \lambda_i - \lambda_j \leq 2\pi(z_i - z_j) \qquad z_i > z_j \ . \tag{4.10}$$

On the basis of these relations, we see that $\tilde{\rho}(z)$ and $\rho(\lambda)$ are related in the thermodynamic limit by

$$\tilde{\rho}(z)dz = \rho(\lambda)d\lambda \ . \tag{4.11}$$

Noticing that for $L \to \infty$ we can substitute sums with integrals

$$\frac{1}{L}\sum_{i=1}^{N} f(\lambda_i) \quad \xrightarrow{L\to\infty} \quad \int_{-\infty}^{\infty} d\lambda\, \rho(\lambda) f(\lambda) \ , \tag{4.12}$$

the strictly monotonically increasing function $\lambda = \lambda(z)$ that implicitly appears in (4.11) is obtained by taking the thermodynamic limit of (4.4) after replacing I_j/L with a real variable z and λ_j with the real function $\lambda(z)$

$$z = \frac{\lambda(z)}{2\pi} + \frac{1}{2\pi}\int d\mu\, \rho(\mu)\, \theta(\lambda(z) - \mu) \ . \tag{4.13}$$

From the inverse function $z = z(\lambda)$ and (4.11) we get

$$\begin{gathered} \rho(\lambda) = \frac{dz}{d\lambda}\tilde{\rho}(z(\lambda)) = \frac{1}{2\pi}\left[1 + \int d\mu\, \rho(\mu) K(\lambda-\mu)\right]\tilde{\rho}(z(\lambda)) \ , \\ K(x) = \theta'(x) = \frac{2c}{c^2+x^2} \ . \end{gathered} \tag{4.14}$$

Given that $1 - \tilde{\rho}(z)$ represents the distribution of *unoccupied* (half-odd) integers, in light of (4.11) and (4.14) it is natural to interpret $\rho_h(\lambda)$ in

$$\rho(\lambda) + \rho_h(\lambda) = \frac{1}{2\pi}\left[1 + \int d\mu\, \rho(\mu) K(\lambda-\mu)\right] = \frac{dz}{d\lambda} \tag{4.15}$$

as the distribution of “holes” in rapidity space, associated with the distribution of “particles” $\rho(\lambda)$. Indeed, dz in (4.11) represents an infinitesimal interval in the space of both occupied and unoccupied (half-odd) integers, therefore $dz/d\lambda$ must be given the interpretation of a density of occupied and unoccupied rapidities.

From Eq. (4.8) we see that eigenstates $|\lambda\rangle$ belonging to the same macrostate $\rho(\lambda)$ possess identical intensive eigenvalues for all the charges $Q^{(m)}$ in the limit of large L, given that

$$q_\lambda^{(m)} = \frac{Q_\lambda^{(m)}}{L} = \frac{1}{L}\sum_{i=1}^{N}\lambda_i^m = \int d\lambda\, \rho(\lambda)\, \lambda^m + o(L^0) \qquad m \geq 0,\ m \neq 2. \tag{4.16}$$

Clearly an identical expression holds for $Q_\lambda^{(2)} = H$ once we add to it Nh, see (4.5). Given the local nature of the charges $Q^{(m)}$, Eq. (4.16) suggests that eigenstates in the same macrostate have identical local properties, that is, identical expectation values for *any* local operator, up to finite size corrections. As mentioned in Section 1.3.1, this is the direct generalization to the integrable setting of the diagonal ETH, which states that expectation values of local observables over eigenstates of quantum chaotic systems are smooth functions of the energy density alone[8].

Given a macrostate $\rho(\lambda)$, we can define its entropy density functional $s[\rho]$ as

$$s[\rho] = \lim_{L\to\infty} \frac{1}{L} S_L[\rho] \ , \tag{4.17}$$

where $S_L[\rho]$ indicates the logarithm of the total number of eigenstates in the macrostate $\rho(\lambda)$, at finite L. Clearly, associating a finite-L eigenstate with a macrostate $\rho(\lambda)$ (which is properly defined only in the thermodynamic limit) is in principle an ambiguous procedure, and some prescription for precisely performing the identification must be chosen. However, any such prescription works as long as it is compatible with the definition (4.8) for $L \to \infty$. In particular, in light of (4.9), we can say that there are

$$W_L = \binom{L\Delta z}{L\tilde{\rho}(z)\Delta z} \tag{4.18}$$

different ways compatible with the macrostate $\tilde{\rho}(z)$ of rearranging occupied and unoccupied (half-odd) integers in a given interval $[z, z+\Delta z]$. This gives the following contribution ΔS_L to the entropy $S_L[\rho]$ (using Stirling's asymptotic formula in the limit of large L)

$$\Delta S_L = \ln W_L = L\,\Delta z \Big[-\tilde{\rho}(z) \ln \tilde{\rho}(z) - \Big(1 - \tilde{\rho}(z)\Big) \ln \Big(1 - \tilde{\rho}(z)\Big)\Big] \ . \tag{4.19}$$

Different prescriptions for the counting result in negligible $o(L)$ corrections to the previous equation. Summing up contributions ΔS_L in every interval Δz yields in the thermodynamic limit

$$s[\rho] = \int d\lambda \Big[\Big(\rho(\lambda)+\rho_h(\lambda)\Big) \ln \Big(\rho(\lambda)+\rho_h(\lambda)\Big) - \rho(\lambda) \ln \rho(\lambda) - \rho_h(\lambda) \ln \rho_h(\lambda)\Big] \ , \tag{4.20}$$

where we have used Eqs. (4.14) and (4.15).

---

[8] Or, at most, of the density of a few mutually commuting charges.

Maximizing $s[\rho]$ with respect to the function $\rho(\lambda)$ under the constraints $\int d\lambda\, \rho(\lambda) = n$ and $\int d\lambda\, \rho(\lambda)(\lambda^2 - h) = e$ (i.e. minimizing the free energy) yields the "thermal" root density $\rho^{(T)}(\lambda)$ that characterizes *typical* eigenstates at particle density n and energy density e. It coincides with the solution of the following nonlinear integral equations [94, 298]

$$\frac{\rho^{(T)}(\lambda)}{\rho^{(T)}(\lambda) + \rho_h^{(T)}(\lambda)} = \frac{1}{1 + e^{\varepsilon(\lambda)/T}} \ , \tag{4.21}$$

$$\varepsilon(\lambda) = \lambda^2 - h - \frac{T}{2\pi} \int d\mu\, K(\lambda - \mu) \ln \left[1 + e^{-\varepsilon(\mu)/T}\right] \ , \tag{4.22}$$

where the temperature T and chemical potential h fix the particle and energy densities, and the hole distribution $\rho_h^{(T)}$ is defined as in Eq. (4.15). The appearance of a Fermi-Dirac functional form in (4.21) is a consequence of the single-occupancy constraint on the (half-odd) integers $\{I_j\}$ (generalized Pauli principle), which justifies the use of the binomial coefficient (4.18) in the calculation of the entropy.

By construction, typical (i.e. thermal) eigenstates dominate (exponentially with L) thermal expectation values of local observables O

$$\langle O \rangle_T = \frac{1}{Z_T} \mathrm{Tr} \left[e^{-H/T} O \right] \ , \tag{4.23}$$

where the trace can either be restricted to the $Q = N$ sector or be extended[9] over all particle-number sectors and the chemical potential h used to fix the average density $\langle Q \rangle_T / L = n$. We note that the exponential domination of thermal eigenstates can be formalized in the limit of large L by representing the trace in (4.23) as a functional integral over root densities and employing the saddle-point method to evaluate it [94], which leads exactly the constrained maximization we performed to obtain Eqs. (4.21) and (4.22). Crucially, given that eigenstates in the same macrostate have identical local properties, in the limit of large L the trace in (4.23) can be replaced, up to finite-size corrections (*cf.* Eq. (4.16)), by the expectation value on a single representative eigenstate $|\lambda^{(T)}\rangle$ of $\rho^{(T)}(\lambda)$, i.e.

$$\langle O \rangle_T = \langle \lambda^{(T)} | O | \lambda^{(T)} \rangle + o(L^0) \ . \tag{4.24}$$

---

[9] By equivalence of thermodynamic ensembles [23].

We remark that to obtain the thermal root density $\rho^{(T)}(\lambda)$ at temperature T and chemical potential h we need to determine the solution $\varepsilon(\lambda)$ of the Yang-Yang equation (4.22). This can be done iteratively: we start by evaluating the right-hand side of (4.22) after the substitution $\varepsilon(\lambda) \to \varepsilon_0(\lambda) = \lambda^2 - h$, and setting the result equal to $\varepsilon_1(\lambda)$; we then iterate this step in order to determine $\varepsilon_{m+1}(\lambda)$ from $\varepsilon_m(\lambda)$. This sequence is guaranteed to converge to the solution of the Yang-Yang equation for $m \to \infty$, see [94, 298]. In practice, we choose a sufficiently large cutoff $k_{\text{max}} > 0$ for the rapidities (it must be checked a posteriori that $\int_{k_{\text{max}}}^{\infty} d\lambda\, \rho^{(T)}(\lambda) \ll 1$), and set up a grid of M values λ_i in the finite interval $[-k_{\text{max}}, k_{\text{max}}]$, with associated weights w_i, according to the Gauss-Legendre quadrature rule. This allows us to approximate the integral in the Yang-Yang equation with a discrete sum, and convergence with M and n is achieved very quickly. Having obtained $\varepsilon(\lambda)$, we determine $\rho^{(T)}(\lambda)$ by solving Eqs. (4.15) and (4.21). Given the quadrature rule discretization, this simply amounts to computing the inverse of a matrix. The entropy density $s[\rho^{(T)}]$ can then be directly obtained from Eq. (4.20).

4.2.3 Impenetrable limit

The Hamiltonian (4.2) has two free limits: free bosons in the absence of interactions ($c = 0$) and free fermions in the impenetrable limit ($c = \infty$) [299]. The former corresponds to the standard, rather trivial, field theory of free scalar bosons in 1D. The impenetrable limit, on the other hand, although mappable to a non-interacting theory retains several non-trivial features which will be very useful in the following sections.

Due to the divergent coupling constant $c = \infty$, the wavefunctions $\chi_N(x_1, \dots, x_N)$ from Eq. (4.3) at any finite energy density, although symmetric (bosons), must vanish whenever $x_i = x_j$ for $i \neq j$, which is the characteristic feature of fermionic wavefunctions. Indeed, for $c = \infty$ the bosonic wavefunction χ_N can be exactly mapped to a fermionic one $\chi_N^{(F)}$ by the Girardeau formula [299]

$$\chi_N^{(F)}(x_1, \dots, x_N) = \prod_{1 \le i < j \le N} \operatorname{sgn}(x_j - x_i)\, \chi_N(x_1, \dots, x_N) \,. \tag{4.25}$$

The boson-fermion mapping leading to a free Hamiltonian is best illustrated in second quantization language at the level of the bosonic field $\phi(x)$. For $c=\infty$, within the physical part of the Hilbert space associated with a *finite* energy density, the boson field $\phi(x)$ can be mapped to a fermionic one $\psi_F(x)$ by a continuum generalization [300] of a Jordan-Wigner transformation [180, 301, 302], which in the thermodynamic limit reads

$$\phi(x) = \exp\left[i\pi \int_{-\infty}^{x} dy\, \psi_F^\dagger(y)\psi_F(y)\right] \psi_F(x) \ . \tag{4.26}$$

Here $\psi_F(x)$ obeys canonical anticommutation relations $\{\psi_F(x), \psi_F^\dagger(y)\} = \delta(x-y)$ and a non-local “string” operator appears in the argument of the exponential[10]. The generalization of (4.26) on a ring of size L, given the PBC on the bosons $\phi(x+L) = \phi(x)$, yields the following boundary conditions for the fermions[11] in the sector with N particles

$$\psi_F(x+L) = (-1)^{N-1}\psi_F(x) \ . \tag{4.27}$$

This is a consequence of the presence of the non-local string in (4.26). We note that the existence of two topologically distinct sectors associated with different boundary conditions is also a standard feature of the Jordan-Wigner mapping on 1D lattices. The representation (4.26) implies that $\phi^2(x)\left|\Psi\right\rangle = 0$ (from anticommutations of ψ_F) for any state $\left|\Psi\right\rangle$ of finite energy density relative to the $H\Big|_{c=\infty}$ Hamiltonian, and this represents the operatorial analogue of the hard-core constraint $\chi_N = 0$ for $x_i = x_j$ $(i \neq j)$. Using the boson-fermion mapping, the Hamiltonian (4.2) at $c=\infty$ becomes quadratic (separately in each sector with N even or odd, see (4.27))

$$H\Big|_{c=\infty} = \int_{-L/2}^{L/2} dx \Big[\psi_F(x)^\dagger(-\partial_x^2 - h)\psi_F(x)\Big] \ , \tag{4.28}$$

where we have used again $\psi_F^2(x) = 0$ when taking the derivatives ∂_x. This coincides with a standard free fermionic theory subject to the boundary conditions (4.27). We can diagonalize $H\Big|_{c=\infty}$ by introducing canonical Fourier-space fields $\tilde{\psi}_{p_j}$ of

---

[10] We note that the spectrum of the non-local string is composed only of integer numbers, hence the choice of the sign in front of $i\pi$ is irrelevant.

[11] Note that the total number of bosons N coincides with the total number of fermions, as a consequence of $\phi^\dagger(x)\phi(x) = \psi_F^\dagger(x)\psi_F(x)$.

discrete momenta $p_j = 2\pi I_j/L$, with I_j forced by (4.27) to be a half-odd integer (integer) for N even (odd)

$$\psi_F(x) = \frac{1}{\sqrt{L}} \sum_j e^{ip_j x}\, \tilde{\psi}_{p_j} \qquad H\Big|_{c=\infty} = \sum_j (p_j^2 - h)\tilde{\psi}^\dagger_{p_j}\tilde{\psi}_{p_j} \ . \tag{4.29}$$

These results are compatible with the fact that for $c \to \infty$ the logarithmic Bethe equations (4.4) simplify to

$$\lambda_j = \frac{2\pi}{L} I_j \qquad j = 1, \dots, N \ , \tag{4.30}$$

i.e. the rapidities coincide with the momenta p_j of free fermions. Given the simple form of the Hamiltonian in this limit, it is elementary to identify the set of extensively many mutually commuting local charges $Q^{(m)}$

$$Q^{(m)}\Big|_{c=\infty} = \sum_j p_j^m\, \tilde{\psi}^\dagger_{p_j}\tilde{\psi}_{p_j} = (-i)^m \int_{-L/2}^{L/2} dx\, \psi^\dagger_F(x)\, \partial_x^m\, \psi_F(x) \qquad m \geq 0, m \neq 2 \ . \tag{4.31}$$

In the following we will be interested in dynamical correlation functions for the Bose field $\phi(x)$ in the interacting regime $0 < c < \infty$. The fact that at $c = \infty$ the field $\phi(x)$ is not local relative to the free Fermi field $\psi_F(x)$, as clear from (4.26), already suggests that correlation functions of $\phi(x)$ in the impenetrable limit are rather difficult to obtain, compared to the trivial non-interacting case $c = 0$. This is related to the fact that matrix elements of $\phi(x)$ between eigenstates of H at $c = \infty$ are *non-sparse*[12], i.e. there is an exponential number (in L, fixed any arbitrarily large but $\mathcal{O}(L^0)$ momentum cutoff) of them with a nonzero value [98]. This is very different from more standard free theories, in which matrix elements of physical operators are sparse (only a polynomial number of them does not vanish). These observations will allow us to make use of the impenetrable limit $c = \infty$ as a benchmark for the numerical methods that we developed to address the interacting region $0 < c < \infty$.

---

[12] This non-sparseness is not unique to the impenetrable Lieb–Liniger model; it appears in any free theory where a local operator is non-local (Jordan-Wigner-like) with respect to the theory's local *free* variables.

4.3 Finite temperature single-particle Green's function via Monte Carlo sampling

4.3.1 Lehmann representation and form factor sampling

Consider the one-body dynamical correlation function

$$C(x,t) = \langle\lambda|\phi^\dagger(x,t)\phi(0,0)|\lambda\rangle \ , \tag{4.32}$$

where $|\lambda\rangle$ is an N-particle eigenstate representative of the thermal macrostate $\rho^{(T)}(\lambda)$ associated with a temperature T and chemical potential h, and $\phi(x,t)$ denotes the Heisenberg time evolution of $\phi(x)$ with the Lieb-Liniger Hamiltonian H in (4.2). Due to (4.24), the correlator $C(x,t)$ is equal, up to finite-size corrections, to

$$\langle\phi^\dagger(x,t)\phi(0,0)\rangle_T = \frac{1}{Z_T}\mathrm{Tr}\left[e^{-H/T}\phi^\dagger(x,t)\phi(0,0)\right] \ . \tag{4.33}$$

This coincides[13] with the finite-temperature single-particle Green's function of the Bose field [27, 303]. The validity of (4.24) even for the operator $\phi^\dagger(x,t)\phi(0,0)$, which is in principle non-local due to the Heisenberg time evolution, follows from the fact that for any finite t it retains a local nature in any finite-energy-density (guaranteed by T finite) state[14], as a consequence of the locality of interactions in (4.2).

In the thermodynamic limit $L \to \infty$ ($n = N/L$ fixed) thermal expectation values like (4.33) depend only on two dimensionless parameters

$$\gamma = c/n \qquad\qquad \tau = T/n^2 \ . \tag{4.34}$$

This can be seen by rescaling space variables with the density as $y = x/n$ in Eqs. (4.1), (4.2) and (4.33) and noticing that for $N \to \infty$ any dependence on n other than the one in (4.34) disappears[15].

The Lehmann representation of the correlation function $C(x,t)$ is obtained by inserting a resolution of the identity $\sum_\mu |\mu\rangle\langle\mu|$ between the two fields in (4.32)

$$C(x,t) = \sum_\mu g_{\lambda,\mu}(x,t)\,|F_{\lambda,\mu}|^2 \ , \tag{4.35}$$

---

[13] Up to the presence of a time-ordering operator.

[14] Employing an intuitive quasiparticle picture, the requirement of a finite energy density translates into an effective cutoff for the speed of the quasiparticles that govern the propagation of correlations and operator spreading. This gives rise to an effective state-dependent light cone.

[15] We are now interpreting (4.33) as the canonical ensemble expectation value.

where

$$\begin{aligned} F_{\lambda,\mu} &= \langle \mu | \phi(0,0) | \lambda \rangle \ , \\ g_{\lambda,\mu}(x,t) &= e^{i(E_\lambda - E_\mu)t - i(P_\lambda - P_\mu)x} \ . \end{aligned} \tag{4.36}$$

Here $|\lambda\rangle$ and $|\mu\rangle$ are normalized to 1. Crucially, closed-form expressions for the form factors $F_{\lambda,\mu}$ are known from the algebraic Bethe ansatz [94, 249, 304, 305]. These show that $F_{\lambda,\mu}$ is nonzero for any eigenstate $|\mu\rangle$ of $N-1$ particles[16], i.e. there are exponentially many in L (fixed any arbitrarily large but finite momentum cutoff for the rapidities) nonzero matrix elements involved in the Lehmann representation (4.35). While in systems that satisfy ETH matrix elements like $F_{\lambda,\mu}$ are all exponentially suppressed in L (*cf.* Section 1.2), their structure is richer in integrable systems, as a consequence of the existence of extensively many commuting charges. In particular, the scaling of

$$M_{\lambda,\mu} = -\ln(|F_{\lambda,\mu}|^2) \tag{4.37}$$

can be superextensive for $|\lambda\rangle$ and $|\mu\rangle$ that differ considerably in the distribution of their rapidities [98]. This implies that only a tiny (but still exponentially large) fraction of eigenstates $|\mu\rangle$, characterized by a "merely" extensive $M_{\lambda,\mu}$, can contribute a finite amount to the Lehmann sum (4.35) for $L \to \infty$.

As shown in Ref. [249], at zero temperature $T = 0$ and number of particles $N \lesssim 200$, the number of relevant $|\mu\rangle$ states for the reconstruction of $C(x,t)$ is not prohibitively large and an *explicit* sum over them can be carried out by the ABACUS algorithm [288, 289], which searches for relevant $|\mu\rangle$ states with sufficiently small $M_{\lambda,\mu}$ until a certain sum rule (see e.g. Eq. (4.39) below) is close to being fully saturated. Recently Ref. [260] addressed, using similar methods, very small but nonzero temperatures for number of particles $N \approx 40$–80. ABACUS has been successfully employed at finite temperatures also to reconstruct 2-point dynamical correlators of the density $\varrho(x) = \phi^\dagger(x)\phi(x)$, for fairly large values of $N \approx 50$–100 (depending on the specific choice of T) [251]. In Section 4.4 we will present numerical results which allow us to explore why ABACUS can, in certain regimes of T and N,

---

[16] Note that $F_{\lambda,\mu}$ trivially vanishes for $|\mu\rangle$ with more or less than $N-1$ particles, as a consequence the selection rule on the particle-number Q.

be successfully employed for reconstructing correlation functions of $\varrho(x)$, while it fundamentally struggles with correlators of the Bose field $\phi(x)$. Indeed, away from the low temperature limit, the number of $|\mu\rangle$ states that meaningfully contribute to (4.35) lies significantly beyond the capabilities of ABACUS already for systems with a few tens of particles.

We now show that it is possible to overcome this limitation by employing a simple yet very effective scheme (see also [273]), based on Markov chain Monte Carlo (MCMC) sampling [306–310]. We rewrite (4.35) as

$$C(x,t) = Z_\lambda \sum_\mu g_{\lambda,\mu}(x,t) \frac{e^{-M_{\lambda,\mu}}}{Z_\lambda} \ , \tag{4.38}$$

where the "partition function" Z_λ simply corresponds to the density of particles

$$Z_\lambda = \sum_\mu e^{-M_{\lambda,\mu}} = \langle\lambda|\phi^\dagger(0,0)\phi(0,0)|\lambda\rangle = n \ . \tag{4.39}$$

To draw a helpful analogy with classical statistical mechanics, we can interpret $\mathcal{P}_\lambda(\mu) \equiv \exp(-M_{\lambda,\mu})/Z_\lambda$ as a normalized Gibbs distribution, where $M_{\lambda,\mu}$ plays the role of an "energy". The key realization is that eigenstates $|\mu_\ell\rangle$ can be sampled according to $\mathcal{P}_\lambda(\mu)$ via MCMC, yielding the following estimate for $C(x,t)$

$$C(x,t) \ \rightarrow \ \frac{Z_\lambda}{\ell_{\max}} \sum_{\ell=1}^{\ell_{\max}} g_{\lambda,\mu_\ell}(x,t) \ . \tag{4.40}$$

The technical details of the MCMC sampling are discussed in Appendix C.1. Crucially, we find that the number of MCMC steps $\ell_{\max}$ needed to reconstruct $C(x,t)$ with high accuracy is *drastically lower* than the number of $|\mu\rangle$ states that meaningfully contribute to the sum in (4.38). This enables us to probe significantly higher temperatures and system sizes than those available by previous approaches.

In the following we always set the chemical potential h such that $n = N/L = 1$. Furthermore, we choose $|\lambda\rangle$ in Eq. (4.32), i.e. the N-particle eigenstate representative of the thermal macrostate chosen, to be a "smooth microstate" of $\rho^{(T)}(\lambda)$ [98]. In other words, we require that the finite-N distribution of its Bethe rapidities matches as smoothly as possible the thermodynamic root density $\rho^{(T)}(\lambda)$ chosen. For a simple construction of smooth microstates given an arbitrary root-density $\rho(\lambda)$, see [98].

4.3.2 Monte Carlo estimates for the number of relevant states

Let $m = M_{\lambda,\mu}/L$ denote the generalized "energy" density associated with the Gibbs expectation value in Eq. (4.38). In the limit of large L the product between the Gibbs weight $\mathcal{P}_\lambda(\mu) = \exp(-L\,m)/Z_\lambda$ and the density of $|\mu\rangle$ states at a given m, which we denote as $\exp(L\,s_\mu(m))$, is expected to give rise to a single sharp peak that dominates the sum in (4.38), as evident from the use of saddle-point methods. From the fact that $Z_\lambda = n = O(L^0)$, it follows that at the saddle point m^* the entropy density s_μ is $s_\mu(m^*) = m^* + o(L^0)$, i.e. the number of relevant $|\mu\rangle$ states for the reconstruction of $C(x,t)$ scales to leading order as $\exp(L\,m^*)$.

To show that our MCMC scheme is capable of probing this saddle-point behaviour, we plot in Fig. 4.1 the values of m sampled in single runs of MCMC, for several temperatures τ and couplings γ. As we increase $L = N$, the variance of the m values shrinks, compatible with the expected $L \to \infty$ limit in which all sampled m sit on a line that coincides with m^*. We also compare the MCMC output with the entropy density $s[\rho^{(T)}]$ associated with the thermal macrostate at γ and τ, see Eq. (4.20). The results show that $s[\rho^{(T)}] > m^* \approx s_\mu(m^*)$, i.e. the number of relevant $|\mu\rangle$ states for the computation of $C(x,t)$ represent an *exponentially small* fraction of all eigenstates in the thermal macrostate of $|\lambda\rangle$. The difference $s[\rho] - m^*$ is seen to increase with the dimensionless temperature τ, as shown more explicitly in Fig. 4.2, where we plot the average value of m over single MCMC runs at $\gamma = \infty$. We note that the inequality $s[\rho] > s_\mu(m^*)$ is compatible with the findings of Ref. [98], which numerically showed that typical $(N-1)$-particle eigenstates $|\mu\rangle$ in the same macrostate as the N-particle reference state $|\lambda\rangle$ feature matrix elements with scaling $M_{\lambda,\mu} \propto L \ln L$, and hence that these do not contribute to $C(x,t)$ in the thermodynamic limit.

The states $|\mu\rangle$ that matter are characterized by a distribution of rapidities $\{\mu_j\}$ which is *anomalously* close to the reference one $\{\lambda_j\}$ [98], as for these one finds $M_{\lambda,\mu} \propto L$. As an example of this, we show in the insets of Fig. 4.1(b) and (f) the linear scaling with L of the average $M_{\lambda,\mu}$ for 100 eigenstates $|\mu\rangle$ randomly generated

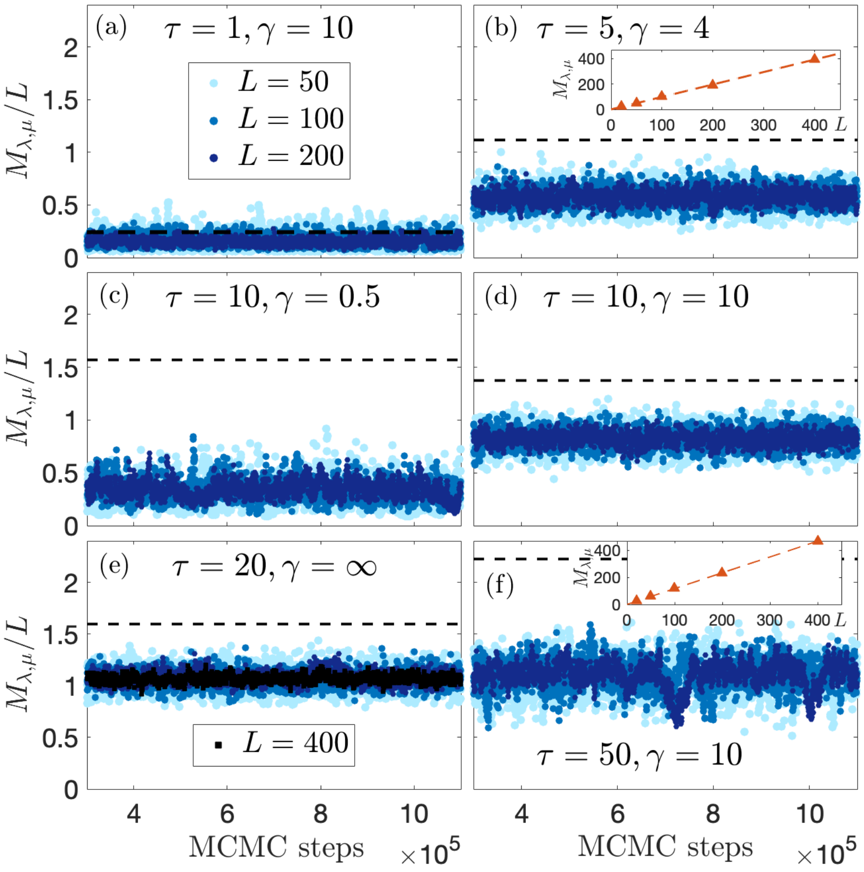

Figure 4.1: Values of $M_{\lambda,\mu}/L$ sampled in a single run of the MCMC sampling, at different strengths γ, temperatures τ and sizes L. We plot 1 value every 3000 MCMC steps. The dashed lines represent the entropy densities $s[\rho]$ (see Eq. (4.20)) associated with the thermal macrostates $\rho(\lambda) = \rho^{(T)}(\lambda)$ at couplings γ and temperatures $T = \tau\, n^2$. The insets in (b) and (f) show that $M_{\lambda,\mu}$ grows linearly with $L = N$ for a simple scalable family of $|\mu\rangle$ states (see main text).

by solving the Bethe equations (4.4) with integers $\{J_j^{(\mu)} = \tilde{I}_j^{(\lambda)} \pm 1/2\}_{j=1}^{N-1}$ (the signs $\pm$ are drawn at random), where $\{\tilde{I}_j^{(\lambda)}\}_{j=1}^{N-1}$ are $N-1$ of the N half-odd integers $\{I_j^{(\lambda)}\}_{j=1}^{N}$ that determine the rapidities $\{\lambda_j\}$. It is evident that the distribution of integers for this family of $|\mu\rangle$ states is anomalously close to that of the half-odd integers $\{I_j^{(\lambda)}\}_{j=1}^{N}$, and this extends at the level of their rapidities via the Bethe equations.

By estimating $m^* \approx s_\mu(m^*)$ from the data in Fig. 4.1 we realize that the number of MCMC steps employed in the sampling is drastically lower than the number of relevant $|\mu\rangle$ states $\exp(L s_\mu(m^*))$. For example, by considering the mean and standard deviation of the $M_{\lambda,\mu}$ values at $\tau = 10, \gamma = 10, L = 200$ in Fig. 4.1(d), we get $s_\mu(m^*) = 0.82 \pm 0.06$. This gives an order of magnitude of

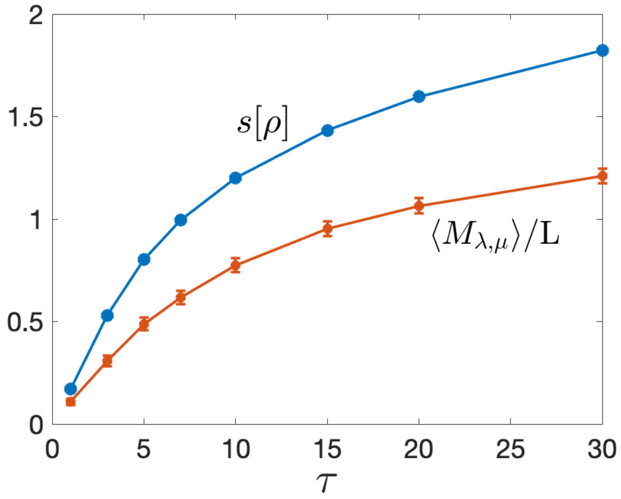

Figure 4.2: Average values of $M_{\lambda,\mu}/L$ as a function of the temperature τ over single MCMC runs at $\gamma = \infty$ and $L = 400$, *cf.* Fig. 4.1(e). We compare them with the entropy density $s[\rho]$ of the thermal macrostate $\rho(\lambda) = \rho^{(T)}(\lambda)$ at temperature τ and $\gamma = \infty$. The orange error bars indicate standard deviations.

10^{66}–10^{76} for the number of relevant states. On the other hand, we will show in the next subsection that very accurate results for $C(x,t)$ can be obtained using a total of only 10^8–10^9 MCMC sampled points.

4.3.3 Benchmarks and results

To benchmark the approach, we consider the impenetrable limit $\gamma = \infty$. As discussed in Section 4.2.3, despite the fact that here the model can be mapped to free fermions, unlike generic (not Jordan-Wigner-like) local operators in standard free theories the form factors $F_{\lambda,\mu}$ of the Bose field $\phi(x)$ are nonzero for any eigenstate $|\mu\rangle$ with $N-1$ particles [98], exactly as in the interacting case $\gamma < \infty$. Hence, from the perspective of reconstructing $C(x,t)$ by sampling states appearing in the Lehmann sum (4.38), the limit $\gamma = \infty$ poses challenges identical to the ones faced in the penetrable case. However, in the impenetrable limit analytical expressions for $\lim_{L\to\infty} C(x,t)$ exist [94, 311–313] and give us access to a direct comparison with exact results. These formulas involve Fredholm determinants [94, 304, 311, 314, 315] that can be numerically computed by standard methods [316]. In Fig. 4.3(a) we plot the MCMC results for $\mathrm{Re}[C(x,t)]$ at $\gamma = \infty$, $\tau = 5$ and $L = 200$. The

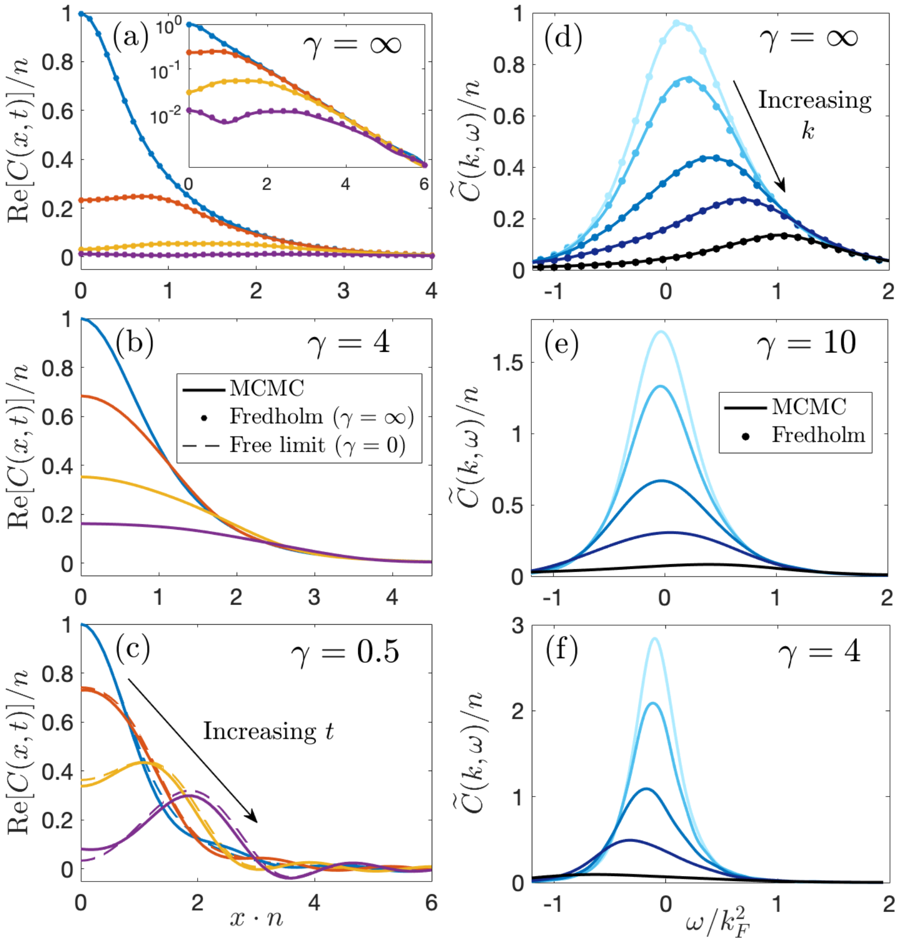

Figure 4.3: Values of $\mathrm{Re}[C(x,t)]$ (real space) and $\tilde{C}(k,\omega)$ (Fourier space) obtained running 100 Markov chains in parallel with $\ell_{\max} = 10^6$ MCMC steps each ($\ell_{\max} = 10^7$ for $\gamma = \infty$). All plots refer to $L = 200$ and $\tau = 5$, and probe different couplings γ. We rescale the frequencies in terms of the Fermi momentum $k_F = \pi n$ associated with the Fermi surface at $\gamma = \infty$ and $\tau = 0$. (a)-(c) Real space correlators as a function of the position at times $t = (0, 0.2, 0.4, 0.6)/n^2$ (respectively blue, red, yellow and purple curves). The dots and dashed lines are exact thermodynamic-limit results respectively at $\gamma = \infty$ (from Fredholm determinant representations [94, 311]) and in absence of interactions ($\gamma = 0$). The inset in (a) shows the same data in log-scale. (d)-(f) Fourier space correlators as a function of the frequency at momenta $k/k_F = (0, 0.16, 0.32, 0.48, 0.8)$ (respectively from lightest to darkest curves). The dots are obtained by Fourier transforming the exact real-space Fredholm results.

agreement with the Fredholm results is found to be excellent. The MCMC output also recovers the exponential decay with x expected from the finiteness of correlation lengths at finite temperatures, see inset of Fig. 4.3(a).

As an additional (qualitative) check, in Fig. 4.3(c) we perform a comparison between the MCMC data at $\gamma = 1/2$ and the exact thermodynamic-limit results in the absence of contact interactions ($\gamma = 0$). The curves appear to be very similar, as expected from the fact that low values of γ should tend towards the free limit $\gamma = 0$. Fig. 4.3(b) shows results for the intermediate value of $\gamma = 4$, where the curves visually interpolate between those in Fig. 4.3(a) and (c).

To extract information on the spectrum of physical excitations created by the action of $\phi(x)$ at finite T it is convenient to consider the Fourier transform of $C(x,t)$ [249]

$$\begin{aligned}\widetilde{C}(k,\omega) &= \int_{-L/2}^{L/2} dx \int_{-\infty}^{\infty} dt\, e^{i\omega t - ikx} C(x,t) \\ &= 2\pi L \sum_{\mu} \delta(\omega - E_\mu + E_\lambda)\, \delta_{k,P_\mu - P_\lambda}\, |\, \langle \mu | \phi(0,0) | \lambda \rangle\, |^2 \ .\end{aligned} \tag{4.41}$$

This is proportional to the bosonic spectral function up to a factor of $(1 + n_B(\omega))$ [27], where $n_B(\omega)$ denotes the Bose-Einstein distribution function. While it is in principle possible to compute $\widetilde{C}(k,\omega)$ by Fourier transforming the MCMC data for $C(x,t)$, it is more convenient to sample directly in Fourier space. Furthermore, given that at any finite L the function $\widetilde{C}(k,\omega)$ consists of a sum of Dirac delta peaks, we implement a smoothing procedure appropriate for comparison with $L \to \infty$. Details of the sampling in Fourier space and the smoothing procedure are presented in Appendix C.2.

In Fig. 4.3(d) we compare the $\gamma = \infty$ MCMC curves for $\widetilde{C}(k,\omega)$ with the exact Fredholm results in Fourier space, finding perfect agreement. In Fig. 4.3(e) and (f) we plot results for the finite couplings $\gamma = 4$ and 10. We see that, fixed $\tau > 0$, a decrease in γ causes the curves to become more sharply peaked and to drift towards negative values of ω. The former behaviour is consistent with the emergence, at low interaction couplings, of well-defined quasiparticles that couple to $\phi(x)$ and whose damping rate vanishes as the non-interacting limit $\gamma = 0$ is approached. Similarly, the drift towards negative energies can be understood from the fact that at $\gamma = 0$ the Fourier correlator is a sum of Dirac deltas lying on the free dispersion $\omega(k) = -k^2 + h$ at minus the occupied momenta of the reference eigenstate $|\lambda\rangle$, i.e. at $k_i = -\lambda_i$.

To check the magnitude of finite-size deviations from the thermodynamic limit behaviour in Fig. 4.4 we plot $\widetilde{C}(k,\omega)$ at distinct sizes L. We see that in the range of k and ω values of interest, where the signal is significant, finite size effects are very weak already at $L \gtrsim 50$, given the good agreement of all the curves.

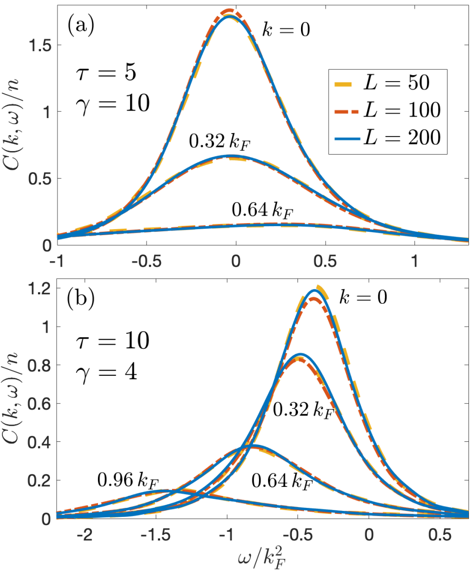

Figure 4.4: Finite size effects in the values of the Fourier-space correlator $\widetilde{C}(k,\omega)$, at different temperatures τ and couplings γ. The frequency and momenta are rescaled with $k_F = \pi\, n$.

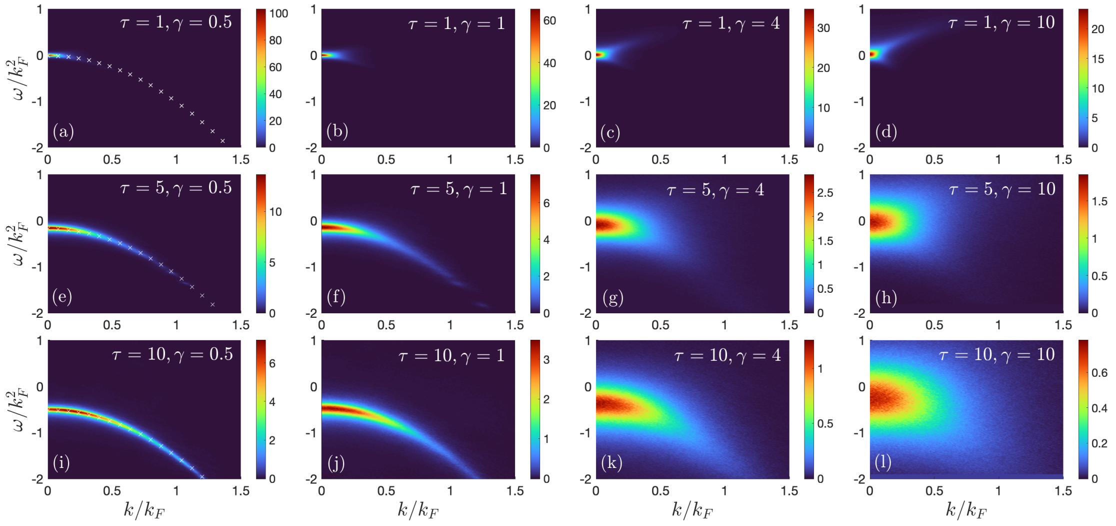

Figure 4.5: Density plots for $\widetilde{C}(k,\omega)/n$ at different temperatures τ and couplings γ. Data obtained for $L=200$ by running 100 parallel Markov chains with $\ell_{\max} = 10^6$ steps each. The white 'x' markers in (a), (e), (i) denote the free dispersion $\omega = -k^2 + h_{\gamma=0}$, where $h_{\gamma=0}$ is the chemical potential that sets $n=1$ at $\gamma=0$ (for each given τ). Note the different scales of colours for each subplot.

In Fig. 4.5 we show full density plots for $\widetilde{C}(k, \omega)$ at several temperatures τ and couplings γ. For $\gamma = 0.5$ the spectral weight closely follows the free dispersion $\omega = -k^2 + h$ of the non-interacting limit $\gamma = 0$. In fact, for $\gamma \leq 1$ the results uncover the presence of a fairly sharp single-particle mode whose peak is slightly broadened by the temperature and finiteness of interactions. At higher γ (especially for $\tau \geq 5$) the weight significantly spreads out into a continuum. We note that the plots at $\tau = 1$ and high γ appear to correctly approach the zero and very-low-temperature results of Refs. [249, 260], with the beginning of a broadened "type II" dispersion [240] clearly visible for $\omega > 0$ (see also log-scale plots below). In the context of matrix elements of the Bose field $\phi(x)$, the zero-temperature type II dispersion $\omega_2(k)$ is associated with energies $\omega_2 = E_\mu - E_\lambda$ and momenta $k = P_\mu - P_\lambda$ where $|\lambda\rangle$ is the ground state of N particles (see Eq. (4.7)) and $|\mu\rangle$ is constructed by starting from the ground state with $N - 1$ particles and implementing a particle-hole excitation that creates a hole in the Fermi sea and adds a particle at the positive boundary of the latter, i.e. just to the right of the Fermi momentum. For any interaction coupling $c > 0$ the dispersion $\omega_2(k)$ vanishes at $k = 0$ and $k = 2k_F$, and is maximal at $k = k_F$, where $k_F = n\pi$ denotes the Fermi momentum of the impenetrable $c = \infty$ model[17]. Given that at $\tau = 0$ the type II dispersion $\omega_2(k)$ represents a *sharp lower threshold* for $\widetilde{C}(k, \omega)$, at small but nonzero τ this feature is expected to remain visible (although it can be broadened by the finite temperature). This is verified more explicitly in Fig. 4.6(a) and (c), which present log-scale density plots of $\widetilde{C}(k, \omega)$ from MCMC at $\tau = 1$ and $\gamma = 10, \infty$.

The data in Fig. 4.6(c)-(f) also provide additional benchmarks at temperatures $\tau = 1$ and $\tau = 5$ for the impenetrable case ($\gamma = \infty$), by comparing MCMC log-scale density plots for $\widetilde{C}(k, \omega)$ ($L = 200$) with the exact Fredholm-representation ones ($L \to \infty$). Again, we find excellent agreement. In Fig. 4.6(b) we show a log-scale density plot for MCMC results at $\gamma = 10$ and $\tau = 5$. Together with Fig. 4.6(d), this clearly highlights that the fairly sharp type II threshold disappears at the higher dimensionless temperature $\tau = 5$.

---

[17] The fact that $k_F = n\pi$ characterizes the boundaries of $\omega_2(k)$ at any c is a consequence of Eqs. (4.6) and (4.30).

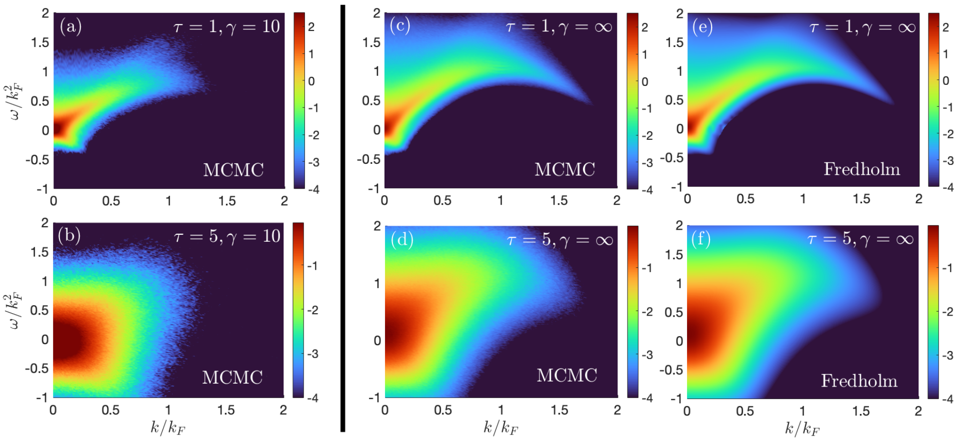

Figure 4.6: Density plots for $\ln[\widetilde{C}(k,\omega)]$ at $L = 200$ and temperatures $\tau = 1$ and 5. MCMC data obtained by running 100 parallel Markov chains with $\ell_{\max} = 10^6$–10^7 steps each. (a)-(b) MCMC results for large but finite couplings $\gamma = 10$. (c)-(d) MCMC results for the impenetrable limit $\gamma = \infty$. (e)-(f) Exact results for $\gamma = \infty$ and $L \to \infty$ from Fredholm representation. The weak non-smooth feature visible in (e) around $k/k_F \approx 0.3$ and $\omega \approx 0$ is due to small noise generated by computing Fredholm determinants for the real space correlators $C(x,t)$ and Fourier transforming to (k,ω) space.

In Fig. 4.7 we plot again the MCMC data from Fig. 4.6(c) and (d) but down to values of $\ln[\widetilde{C}(k,\omega)]$ of -8. We see that the MCMC data appear to capture the signal well even down to these low values (*cf.* log-scale results at $\tau = 0$ from Ref. [249] for a direct comparison). In particular, the $\tau = 1, \gamma = \infty$ plot in Fig. 4.7(a) clearly shows the slightly broadened $\omega_2(k)$ dispersion stretching up to $2k_F$.

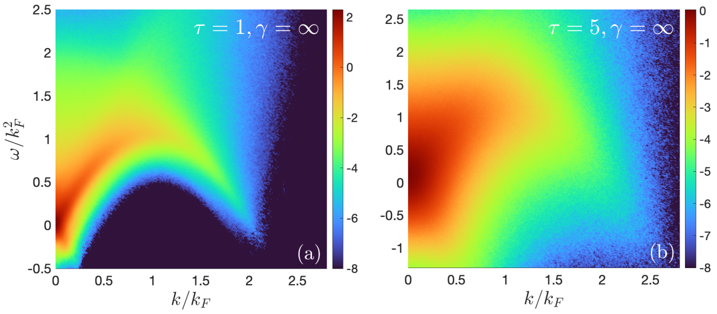

Figure 4.7: Density plots for $\ln[\widetilde{C}(k,\omega)]$ for the same MCMC data as Fig. 4.6(c) and (d) but on a colour scale down to -8.

We stress that although we have presented here results only for thermal macrostates $\rho^{(T)}(\lambda)$ due to their obvious physical importance, our methods can be applied equally well to *atypical* macrostates, as shown in [3].

4.4 Comparing Bose field and density operator

Interacting integrable theories possess exponentially many (in system size) nonzero off-diagonal matrix elements of *any* local operator between eigenstates [43, 94, 98, 100, 249, 304, 305, 317–322]. The vast majority of them[18] is expected to be *at least* exponentially suppressed in L [98, 100]. On the contrary, in free theories only a few sparse matrix elements generally do not vanish, and their magnitudes decay to zero at most polynomially with L.

Exactly as for the Bose field $\phi(x)$, in the interacting regime ($0 < c < \infty$) of the Lieb-Liniger model the exponential (or superexponential) suppression of the matrix elements of the density $\varrho(x) = \phi^\dagger(x)\phi(x)$ can be easily checked numerically starting from known expression for its form factors [317, 318], or analytically by employing expansions of the form factors in $1/c$ (for c large but finite) [98]. This suppression implies that, as we increase L, the use of sampling schemes for the reconstruction of correlation functions becomes eventually *necessary* for both $\phi(x)$ and $\varrho(x)$, given that the number of relevant terms becomes prohibitively large at sufficiently large L. Despite this similarity, we highlight here important differences in the structure of off-diagonal matrix elements of $\phi(x)$ and $\varrho(x)$. The existence of such differences is perhaps not surprising in light of the fact that form factors of $\varrho(x)$ are sparse both at $c = 0$ and $c = \infty$ [98], while those of $\phi(x)$ correspond to a standard free theory only at $c = 0$. These dissimilarities shed light on why correlation functions of $\varrho(x)$, unlike those of $\phi(x)$, can be efficiently reconstructed at finite temperatures and up to fairly large system sizes ($N \approx 50$–100) without the use of sampling [251], although sampling becomes necessary at larger N. En passant, we uncover the existence of some matrix elements of $\varrho(x)$ that are merely polynomially suppressed in L (as in free theories) even in the interacting regime $0 < c < \infty$. This is an interesting fact by itself.

---

[18] Below we uncover an exception to the exponential suppression behaviour, which rules out the applicability of this statement to *all* off-diagonal matrix elements.

Given a reference eigenstate $|\lambda\rangle$ of N particles, the squared form factors

$$|F^{(\varrho)}_{\lambda,\tilde{\lambda}}|^2 = |\,\langle\tilde{\lambda}|\varrho(0)|\lambda\rangle\,|^2 = \exp(-M^{(\varrho)}_{\lambda,\tilde{\lambda}}) \tag{4.42}$$

of the density are nonzero for any N-particle eigenstate $|\tilde{\lambda}\rangle$ with $P_\lambda \neq P_{\tilde{\lambda}}$ [317, 318] (we are restricting to off-diagonal matrix elements, i.e. we require $|\tilde{\lambda}\rangle \neq |\lambda\rangle$). Similarly to the case of $M_{\lambda,\mu}$ for $\phi(x)$, $M^{(\varrho)}_{\lambda,\tilde{\lambda}}$ scales superextensively with L for typical eigenstates $|\tilde{\lambda}\rangle$ in the same macrostate as $|\lambda\rangle$ and eigenstates in a different macrostate [98]. Hence, for large L only atypically large rare form factors in the same macrostate as $|\lambda\rangle$ contribute a finite amount to correlation functions. Below we focus on these.

We fix for both $\varrho(x)$ and $\phi(x)$ an N-particle smooth microstate $|\lambda\rangle$ of a thermal macrostate at some given values of τ and γ (see Section 4.3.1). To meaningfully compare off-diagonal matrix elements of the two different operators we draw a parallelism between the N-particle (with N even) eigenstates $|\tilde{\lambda}\rangle$ for the density (characterized by half-odd integer quantum numbers $\{J^{(\tilde{\lambda})}_j\}$) and the $(N-1)$-particle eigenstates $|\mu\rangle$ for the Bose field (characterized by integers $\{J^{(\mu)}_j\}$). We start by considering the limit of large τ, which corresponds to high temperatures T or low densities of particles n. Here, each half-odd integer in the set of quantum numbers $\{I^{(\lambda)}_j\}$ that fix $|\lambda\rangle$ is well separated from its nearest neighbours. This allows us to construct a reference $(N-1)$-particle eigenstate $|\mu_{\mathrm{ref}}\rangle$ by removing an element from $\{I^{(\lambda)}_j\}$ (we always choose this among the two half-odd integers of lowest absolute value) and shifting all the remaining $I^{(\lambda)}_j$ by $\pm 1/2$, where each sign is chosen at random (similarly to the construction used for the insets of Fig. 4.1). Note that in the limit of large τ (and large γ) it is easy to check that the family of states $|\mu_{\mathrm{ref}}\rangle$ is associated with the lowest possible factors $M_{\lambda,\mu}$, i.e. the largest matrix elements of the Bose field. We can generate arbitrary eigenstates $|\tilde{\lambda}\rangle$ and $|\mu\rangle$ by adding an arbitrary number n_{ph} of particle-hole excitations[19] on top of, respectively, $|\lambda\rangle$ and $|\mu_{\mathrm{ref}}\rangle$. This construction allows us to compare $M_{\lambda,\mu}$ and $M^{(\varrho)}_{\lambda,\tilde{\lambda}}$ for eigenstates $|\mu\rangle$ and $|\tilde{\lambda}\rangle$ arising from an equal number n_{ph} of particle-hole excitations.

---

[19] By a particle-hole excitation we mean the replacement of a (half-odd) integer from a set of quantum numbers $\{J_j\}$ with another *unoccupied* (half-odd) integer.

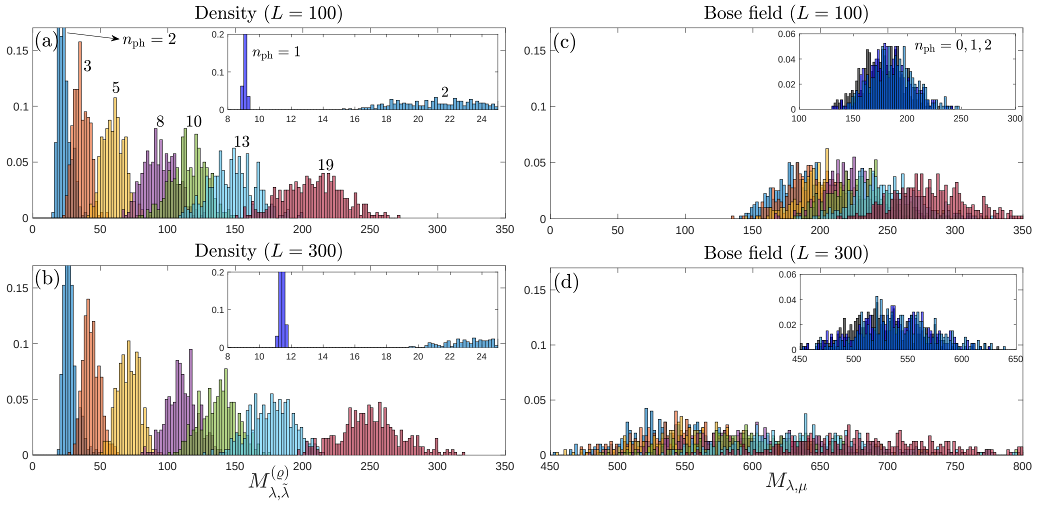

Figure 4.8: Histograms for $M^{(\varrho)}_{\lambda,\tilde\lambda}$ (density) and $M_{\lambda,\mu}$ (Bose field) from randomly drawn eigenstates $|\tilde\lambda\rangle$, $|\mu\rangle$ at $\tau = 500$, $\gamma = 7$ (as in the main text $n = N/L = 1$) and sizes $L = 100, 300$. Each $|\tilde\lambda\rangle$ and $|\mu\rangle$ is generated by applying $n_{\rm ph}$ random particle-hole excitations on top of, respectively, $|\lambda\rangle$ and $|\mu_{\rm ref}\rangle$ (see text for the construction of $|\mu_{\rm ref}\rangle$). Histograms display the relative frequency over the 400 eigenstates drawn for each $n_{\rm ph}$. Each particle-hole excitation is constrained to have momentum transfer $|\Delta P_{\rm ph}| \leq 1$. Colours from blue to red are associated with $n_{\rm ph} = 2, 3, 5, 8, 10, 13, 19$, see (a). Insets show a zoom-in on the region with the lowest number of particle-hole excitations: $n_{\rm ph} = 1, 2$ for the density in (a)-(b) and $n_{\rm ph} = 0, 1, 2$ for the Bose field in (c)-(d) (the value $n_{\rm ph} = 0$ indicates the reference state $|\mu_{\rm ref}\rangle$).

In Fig. 4.8 we show histograms for 400 randomly drawn eigenstates $|\tilde\lambda\rangle$, $|\mu\rangle$ for different values of $n_{\rm ph}$ at $\tau = 500$ and $\gamma = 7$. We find that the results for the density display a considerable degree of "lumpiness" (multimodality of the underlying distribution) compared to the ones for the Bose field. Indeed, for $\varrho(x)$ the peaks associated with different values of $n_{\rm ph}$ are well separated from each other, and the lumpiness appears to become more significant as L is increased. The mode separation is most apparent for low values of $n_{\rm ph}$, see insets in Fig. 4.8(a)-(b). On the other hand, it is significantly more difficult to resolve different peaks in the case of the Bose field, and the degree of multimodality decreases as we increase L. The key (striking) difference between the two operators is the *magnitude* of the $M^{(\varrho)}_{\lambda,\tilde\lambda}$ and $M_{\lambda,\mu}$ sampled. Indeed, $M_{\lambda,\mu}$ is associated with values significantly larger than $M^{(\varrho)}_{\lambda,\tilde\lambda}$, both with respect to a given $n_{\rm ph}$ and overall (in this regard, notice the different x-axis scale in Fig. 4.8(d)). Furthermore, $M^{(\varrho)}_{\lambda,\tilde\lambda}$ appears to vary very slowly with L, unlike $M_{\lambda,\mu}$ which is subject to changes of order L. This dependence on system size already suggests that, fixed L, the number of relevant states for the reconstruction of correlation functions of $\phi(x)$ (see Section 4.3.2) is significantly higher than for the case of $\varrho(x)$. In [3] we also report an analogous plot for the higher coupling $\gamma = 70$ (still at $\tau = 500$), for which identical conclusions hold.

To address a region of the τ-γ parameter space closer to the one that, for the density $\varrho(x)$, has been probed by the ABACUS algorithm [251], we want to perform similar comparisons at lower values of τ (corresponding to lower temperatures or higher density of particles). In this case, constructing $|\mu_{\text{ref}}\rangle$ by the previous method based on the $\pm 1/2$ perturbations is not as meaningful as in the high-τ regime. Indeed, at lower τ most half-odd integers in $\{I_j^{(\lambda)}\}$ lie very close to their nearest neighbours and random choices of the signs ± typically lead to double occupancies (which must be discarded). Instead of focusing on $\pm 1/2$ perturbations that avoid the previous issue (by more carefully selecting the signs ±), here we choose $|\mu_{\text{ref}}\rangle$ to be the smooth microstate of $(N-1)$ particles associated with the thermal root density $\rho^{(T)}(\lambda)$ that specifies the macrostate of $|\lambda\rangle$. Note that unlike before, we now have a single $|\mu_{\text{ref}}\rangle$ at each L instead of a family of them. In Fig. 4.9 we plot the histograms of $M^{(\varrho)}_{\lambda,\bar{\lambda}}$ and $M_{\lambda,\mu}$ at $\tau = 5$ and $\gamma = 7$. We see that the features highlighted in the high-τ regime, and in particular the striking difference in the

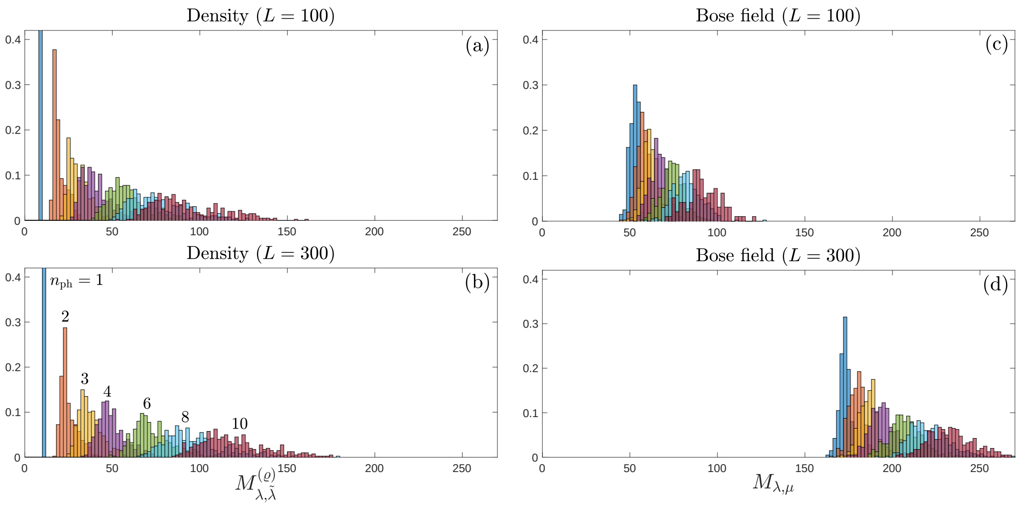

Figure 4.9: Same as Fig. 4.8 but for the lower dimensionless temperature $\tau = 5$, at coupling strength $\gamma = 7$. Colours from blue to red are associated with values $n_{\text{ph}} = 1, 2, 3, 4, 6, 8, 10$, see (b).

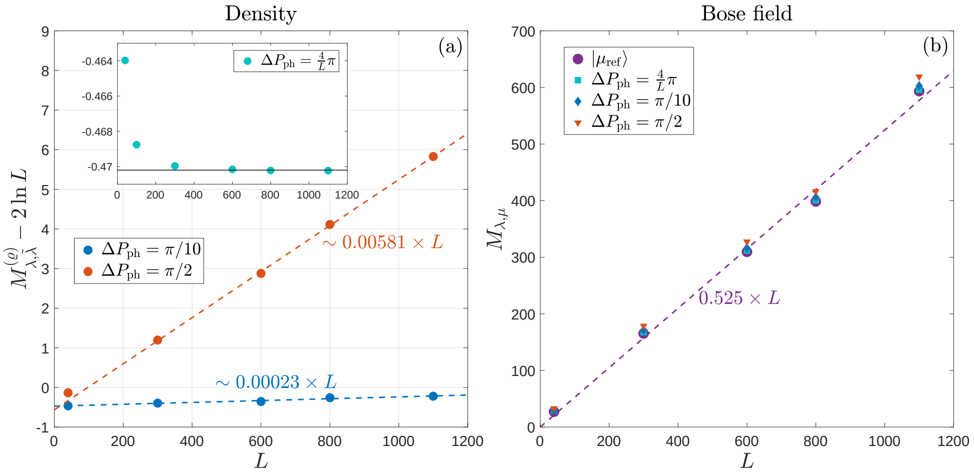

Figure 4.10: Scaling of $M^{(\varrho)}_{\lambda,\tilde\lambda}$ and $M_{\lambda,\mu}$ with L at $\tau = 5, \gamma = 7$. The eigenstates $|\tilde\lambda\rangle$ and $|\mu\rangle$ are constructed by implementing a single particle-hole excitation of momentum $\Delta P_{\rm ph}$ on top of, respectively, $|\lambda\rangle$ and $|\mu_{\rm ref}\rangle$. (a) $M^{(\varrho)}_{\lambda,\tilde\lambda} - 2\ln L$ as a function of L, following the functional form conjectured in [98]. Dashed lines represent 2-parameter linear fits $a\,L + b$ (performed on the 4 data points of largest L). The inset shows analogous data for the vanishing momentum $\Delta P_{\rm ph} = 4\pi/L$, with the horizontal black line denoting the constant asymptotic value. (b) $M_{\lambda,\mu}$ as a function of L for the same momenta $\Delta P_{\rm ph}$ of (a) and for the reference $(N-1)$-particle state $|\mu_{\rm ref}\rangle$ (see text). The dashed line indicate a 1-parameter linear fit $a\,L$ on the $|\mu_{\rm ref}\rangle$ data (performed on the 4 data points of largest L), for which we obtain $a \approx 0.525$. Linear fits for the $\Delta P_{\rm ph} > 0$ data (not reported) feature a parameter a that grows with $\Delta P_{\rm ph}$, e.g. we find $a \approx 0.550$ for $\Delta P_{\rm ph} = \pi/2$.

magnitudes of $M^{(\varrho)}_{\lambda,\tilde\lambda}$ and $M_{\lambda,\mu}$, remain true also here.

To explore more explicitly the different scaling with L of $M^{(\varrho)}_{\lambda,\tilde\lambda}$ and $M_{\lambda,\mu}$ we focus on single particle-hole excitations, i.e. we fix $n_{\rm ph} = 1$. We consider again $\tau = 5$, hence $|\mu_{\rm ref}\rangle$ is the smooth microstate with $(N-1)$ particles (note that $P_{\mu_{\rm ref}} = P_\lambda = 0$). For the density (Bose field) we implement a particle-hole excitation on top of the reference state $|\lambda\rangle$ ($|\mu_{\rm ref}\rangle$) by removing one among a few half-odd integers (integers) of lowest absolute value and inserting an unoccupied positive one, such to create a positive momentum transfer $\Delta P_{\rm ph} > 0$.

In Fig. 4.10(a) we present the scaling of $M^{(\varrho)}_{\lambda,\tilde\lambda}$ with L for $\Delta P_{\rm ph} = \frac{4\pi}{L}, \pi/10, \pi/2$. On the basis of analytic expansions in $1/c$ of matrix elements of $\varrho(x)$, Ref. [98] conjectured the following form for the squared form factors (4.42) associated with $n_{\rm ph} = 1$

$$|F^{(\varrho)}_{\lambda,\tilde\lambda}|^2\Big|_{n_{\rm ph}=1} = \frac{\beta}{L^2}e^{-\alpha L} \qquad \to \qquad M^{(\varrho)}_{\lambda,\tilde\lambda}\Big|_{n_{\rm ph}=1} = \alpha L + 2\ln L - \ln\beta \ , \tag{4.43}$$

where α and β are positive $\mathcal{O}(L^0)$ scalars that depend on details of the distribution of rapidities in $|\lambda\rangle$ and on the particle-hole excitation that leads to $|\tilde\lambda\rangle$. To verify this functional form we plot $M^{(\varrho)}_{\lambda,\tilde\lambda} - 2\ln L$ as a function of L and find the data to be accurately described by a 2-parameter linear fit $a\,L + b$. For finite momentum transfers $\Delta P_{\rm ph} = \pi/10, \pi/2$ we obtain finite but extremely small (order 10^{-4}–10^{-3}) values of a, which estimate the scalar α in Eq. (4.43). This shows that, for system sizes L on the order of a few hundred, *the exponential suppression of these form factors of $\varrho(x)$ is negligible*. In the inset of Fig. 4.10(a) we show an analogous plot for the momentum transfer $\Delta P_{\rm ph} = 4\pi/L$, which vanishes in the thermodynamic limit. Surprisingly, in this case the data are compatible with $\alpha = 0$, i.e. absence of exponential suppression with L. This suggests that in integrable models it is possible to have matrix elements of local operators that are merely polynomially suppressed in L (as in free theories) also in the presence of interactions ($0 < c < \infty$), see also [323]. In Fig. 4.10(b) we present the scaling of $M_{\lambda,\mu}$ with L for the same momentum transfers of Fig. 4.10(a), and for the reference state $|\mu_{\rm ref}\rangle$. The data are well described by 1-parameter linear fits $a\,L$, with a of the order of 10^{-1}–10^{0}, i.e. significantly higher than in the case of $M^{(\varrho)}_{\lambda,\tilde\lambda}$. This is consistent with the L-dependence found in Figs. 4.8 and 4.9, and shows that the exponential decay of off-diagonal matrix elements is significantly faster for the Bose field than for the density. Furthermore, it is compatible with the claim that, unlike for the density $\varrho(x)$, *all* matrix elements of the Bose field are at least exponentially suppressed in L.

Overall, the numerical results presented in this section yield insights on why it is possible to reconstruct finite-T correlation functions of $\varrho(x)$ by the ABACUS algorithm up to fairly large values of N, of the order of 50–100 (depending on the specific temperature chosen) [251]. By construction, ABACUS can only take into account eigenstates with a few particle-hole excitations on top of $|\lambda\rangle$, i.e. $n_{\rm ph} \leq n_{\rm max}$

with $n_{\max}$ finite and not very large. The total number of such eigenstates (given a physical momentum cutoff for their rapidities) scales polynomially with L, hence they become eventually irrelevant for the reconstruction of correlation functions at large enough L, due to the (slow) exponential decay[20] of the density form factors shown in Fig. 4.10(a). However, given the smallness of the coefficient α in their exponential decay $\exp(-\alpha\, N)$, these finite-$n_{\rm ph}$ states remain relevant for the reconstruction of correlation functions at $N \approx 50$–100, where $\alpha\, N \ll 1$ and the exponential suppression is negligible. This is ultimately the reason why ABACUS manages to saturate sum rules for the density $\varrho(x)$ by employing an explicit sum over these types of states. However, similar strategies applied to $\phi(x)$ correlators are limited to significantly smaller temperatures or system sizes [260], and further progress requires the use of sampling schemes like the one presented in the previous sections. Indeed, already at $\tau > 1$ and $N \lesssim 100$, the total number of eigenstates constructed by applying a small number of particle-hole excitations on top of a reference state is very far from counterbalancing the smallness of their matrix elements, *cf.* Fig. 4.10(b).

We conclude by remarking that while at larger values of N than those probed in [251], or at larger temperatures, the use of sampling schemes becomes necessary also for $\varrho(x)$, we find that one cannot directly employ the MCMC strategy described in Appendix C.1 for the Bose field. There, we show that a simple proposal update that implements a single particle-hole excitation, coupled with the Metropolis acceptance step, is very successful in exploring the manifold of relevant states. However, due to the lumpiness that characterizes the matrix elements of $\varrho(x)$ (see Figs. 4.8 and 4.9), these type of Markov updates are associated with extremely small acceptance rates, which lead to very limited explorations of the landscape of relevant eigenstates. It is an interesting problem for future work to identify an *efficient* strategy for sampling relevant matrix elements for the reconstruction of correlation functions of $\varrho(x)$.

---

[20] Note that also the form factors that decay only polynomially with L, e.g. those associated with a $\Delta P_{\rm ph} \propto 1/L$, become irrelevant at large L because their total number does not grow with L.

4.5 Conclusions

We have shown that the MCMC method introduced is capable of reconstructing with high accuracy 2-point dynamical correlation functions of the Bose field, directly from their Lehmann representation. It does so by efficiently sampling relevant form factors, in regimes in which their number is so high that full sums cannot be carried out with classical computational resources.

It would be interesting to extend the form-factor-sampling method to other dynamical scenarios and to other interacting integrable models, although in the latter case the presence of strings of complex rapidities makes accurate solutions of Bethe equations much harder to obtain. Finally, we remark that in the attempt to generalize the current method, implemented here for 2-point functions, to higher-point dynamical correlators, one encounters difficulties analogous to the famous "sign problem" that plagues MCMC simulations in fermionic systems. This is due to the oscillatory phases that appear in the products of (more than 2) form factors in the Lehmann sum. Indeed, unlike in Eq. (4.35), these products do not square to a positive real weight ($|F_{\lambda,\mu}|^2$ in the 2-point case) for higher-point functions. The presence of a "sign problem" in these cases is easily detected by performing saddle-point-like estimates on the Lehmann representation modified by inserting an absolute value inside the sum (see also [77]).

Appendices

A

Appendices for Chapter 2

A.1 Self-consistent time-dependent mean-field theory (SCTDMFT)

Consider a generic many-body Hamiltonian H written in terms of bosonic creation and annihilation operators $\boldsymbol{a}^\dagger = (a_1^\dagger, \ldots, a_n^\dagger, a_1, \ldots, a_n)$. We are interested in studying the time evolution of a Gaussian bosonic state $|\psi(0)\rangle$ under H. In general, the presence of interacting terms in the Hamiltonian turn $|\psi(t)\rangle$ into an entangled non-Gaussian state at any $t > 0$, and no exact solution for the dynamics can be determined. To approximately derive the time evolution we employ a self-consistent time-dependent mean-field theory (SCTDMFT) approach [102, 103, 149, 169–179], where H is replaced with a quadratic time-dependent Hamiltonian $H_{\mathrm{MF}}(t)$ that preserves the Gaussianity of the state

$$|\psi_{\mathrm{MF}}(t)\rangle = U_{\mathrm{MF}}(t)|\psi(0)\rangle = \mathcal{T}\left[\exp\left(-i\int_0^t dt' H_{\mathrm{MF}}(t')\right)\right]|\psi(0)\rangle \ . \tag{A.1}$$

Given the Gaussian nature of $|\psi(t)\rangle_{\mathrm{MF}}$ it can be written in the form

$$|\psi_{\mathrm{MF}}(t)\rangle = Q(t)|0\rangle \qquad Q(t) = C\exp\left[\frac{1}{2}\boldsymbol{a}^\dagger\Lambda(t)\boldsymbol{a} + \boldsymbol{\lambda}(t)\cdot\boldsymbol{a}\right] \ , \tag{A.2}$$

where $|0\rangle$ is the boson vacuum. This shows that $|\psi_{\mathrm{MF}}(t)\rangle$ is a "vacuum" for the operators

$$d_i(t) = Q(t)\, a_i\, Q(t)^{-1} \ . \tag{A.3}$$

Given the form of $Q(t)$, $d_i(t)$ is a linear combination of operators a, $a^\dagger$, plus a constant. This also implies $[d_i(t), d_j(t)] = 0$, $[d_i(t), d_j^\dagger(t)] \in \mathbb{C}$. Inverting (A.3) we get

$$a_i = M_{ij}(t)\, d_j(t) + N_{ij}(t)\, d_j^\dagger(t) + \langle \psi_{\mathrm{MF}}(t)|\, a_i\, |\psi_{\mathrm{MF}}(t)\rangle \ , \tag{A.4}$$

where M, N are matrices. We can now express H as a function of the $d(t)$ bosons and apply Wick's theorem to efficiently write H only in terms of normal ordered operators with respect to $|\psi_{\mathrm{MF}}(t)\rangle$. We split the result of this operation in the two contributions

$$H = N[H_{\geq 3}(t)] + H_{\mathrm{MF}}(t) \ , \tag{A.5}$$

where $H_{\geq 3}(t)$ indicates terms in H that contain 3 or more $d(t)$, $d^\dagger(t)$ and N is the normal ordering operator. Equations (A.1) and (A.5) self-consistently define $H_{\mathrm{MF}}(t)$, which generally takes a simple form when re-expressed back in terms of a, $a^\dagger$ and their 1 and 2-point functions. Using normal ordering arguments, it is easy to see from (A.5) that

1. Energy is conserved in the sense that

$$\frac{d}{dt}\langle \psi_{\mathrm{MF}}(t)|\, H\, |\psi_{\mathrm{MF}}(t)\rangle = i\langle \psi_{\mathrm{MF}}(t)|\, [H_{\mathrm{MF}}(t), H]\, |\psi_{\mathrm{MF}}(t)\rangle = 0 \ . \tag{A.6}$$

2. The equations of motion (EOMs) of 1 and 2-point functions of bosons, from which every expectation value can be obtained by Wick's contractions, are given by

$$\begin{aligned}\frac{d}{dt}\langle \psi_{\mathrm{MF}}(t)|\, O\, |\psi_{\mathrm{MF}}(t)\rangle &= i\langle \psi_{\mathrm{MF}}(t)|[H_{\mathrm{MF}}(t), O]|\psi_{\mathrm{MF}}(t)\rangle \\ &= i\langle \psi_{\mathrm{MF}}(t)|[H, O]|\psi_{\mathrm{MF}}(t)\rangle \ ,\end{aligned} \tag{A.7}$$

where O contains one or two a, $a^\dagger$ operators. The last equality makes apparent that the SCTDMFT truncates the infinite BBGKY hierarchy of EOMs [102, 103, 172] by considering the expectation value of the exact term $[H, O]$ over a Gaussian state. This allows to express the result only in terms of Wick's contractions, thus closing the otherwise infinite set of coupled differential equations in the hierarchy.

Importantly, there always is an early time window in which the SCTDMFT is expected to be quantitatively accurate. This follows from the fact that the EOMs in (A.7) neglect the contribution of connected n-point functions of bosons for $n > 2$, which however vanish at $t = 0$ because $|\psi(0)\rangle$ is Gaussian. In many cases of interest, for example when interaction strengths are small, the growth of the connected n-point functions is expected to be slow and the SCTDMFT is quantitatively accurate up to parametrically large times.

A.2 Derivation of the characteristic function formula

In this appendix we derive equation (2.13) for the characteristic function

$$\chi(\lambda) = \mathrm{Tr}\left[\rho \exp\left(i\lambda\, R\right)\right] \ , \tag{A.8}$$

where ρ is a Gaussian density matrix

$$\rho = \frac{1}{Z}\exp\left[\frac{1}{2}\boldsymbol{a}^\dagger W \boldsymbol{a} + \boldsymbol{w}^\dagger\cdot\boldsymbol{a}\right], \quad W = W^\dagger, \quad \boldsymbol{w}^\dagger = \boldsymbol{w}^T\Sigma^x \ . \tag{A.9}$$

Here the normalization Z enforces $\mathrm{Tr}[\rho] = 1$ and W is restricted to be negative definite. The definition (2.7) of the vector $\boldsymbol{a}$ always allows to choose W such that

$$\Sigma^x W \Sigma^x = W^T \ . \tag{A.10}$$

The 1-point functions and the correlation matrix Δ in this Gaussian state are [161, 162] (or see Appendix D of [1])

$$\begin{aligned} \boldsymbol{\omega} &= \mathrm{Tr}\left[\rho\, \boldsymbol{a}\right] = -W^{-1}\boldsymbol{w} \ , \\ \Delta &= \mathrm{Tr}\left[\rho\,(\boldsymbol{a}-\boldsymbol{\omega})(\boldsymbol{a}^\dagger-\boldsymbol{\omega}^\dagger)\right] - \frac{1}{2}\Sigma^z = -\frac{1}{2}\coth\left(\frac{1}{2}\Sigma^z W\right)\Sigma^z \ , \end{aligned} \tag{A.11}$$

where $\Delta = \Delta^\dagger$ is positive definite. For the quadratic observable R we consider the general class

$$R = \frac{1}{2}\boldsymbol{a}^\dagger G \boldsymbol{a} + \boldsymbol{g}^\dagger\cdot\boldsymbol{a}, \quad G = G^\dagger, \quad \boldsymbol{g}^\dagger = \boldsymbol{g}^T\Sigma^x, \quad \mathrm{Det}(G) \neq 0 \ . \tag{A.12}$$

Similarly to (A.10) we choose without loss of generality $\Sigma^x G \Sigma^x = G^T$. We will consider the special case $\mathrm{Det}(G) = 0$ at the end of this appendix.

We start by defining displacement operators D_β associated with vectors of complex constants $\boldsymbol{\beta}$

$$D_\beta \equiv \exp\left[\boldsymbol{a}^\dagger \Sigma^z \boldsymbol{\beta}\right] , \qquad D_\beta^{-1} = D_\beta^\dagger , \tag{A.13}$$

which have the following properties

$$D_\beta^{-1} \boldsymbol{a}_i \, D_\beta = \boldsymbol{a}_i + \boldsymbol{\beta}_i , \quad D_\beta D_\tau = D_{\beta+\tau} \exp\left[-\frac{1}{2}\boldsymbol{\beta}^\dagger \Sigma^z \boldsymbol{\tau}\right] . \tag{A.14}$$

The displacement operators are a complete orthogonal set on the space of bounded operators [161]. For operators O such that $\mathrm{Tr}\left[O \, D_\beta\right]$ is well defined this translates into

$$O = \frac{1}{\pi^\ell} \int d^2\boldsymbol{\beta} \, \mathrm{Tr}\left[O \, D_\beta\right] \, D_\beta^\dagger \qquad \mathrm{Tr}\left[D_\tau \, D_\beta\right] = \pi^\ell \delta^{2\ell}\left(\boldsymbol{\tau} + \boldsymbol{\beta}\right) , \tag{A.15}$$

where $d^2\boldsymbol{\beta} = \prod_{i=1}^{\ell} d\mathrm{Re}(\beta_i) \, d\mathrm{Im}(\beta_i)$. We can use this to express the characteristic function in the form

$$\begin{aligned} \chi(\lambda) &= \left(\frac{1}{\pi^\ell}\right)^2 \int d^2\boldsymbol{\beta} \int d^2\boldsymbol{\tau} \; \mathrm{Tr}\Big[\rho \, D_\beta\Big] \, \mathrm{Tr}\Big[\exp\left(i\lambda R\right) \, D_\tau\Big] \, \mathrm{Tr}\left[D_\beta^\dagger D_\tau^\dagger\right] \\ &= \frac{1}{\pi^\ell} \int d^2\boldsymbol{\beta} \; \mathrm{Tr}\Big[\rho \, D_\beta\Big] \, \mathrm{Tr}\Big[\exp\left(i\lambda R\right) D_{-\beta}\Big] . \end{aligned} \tag{A.16}$$

The first factor is known, see e.g. [161],

$$\mathrm{Tr}\left[\rho \, D_\beta\right] = \exp\left[-\frac{1}{2}\boldsymbol{\beta}^\dagger \Sigma^z \Delta \Sigma^z \boldsymbol{\beta} + \boldsymbol{\omega}^\dagger \Sigma^z \boldsymbol{\beta}\right] , \tag{A.17}$$

where Δ and $\boldsymbol{\omega}$ are defined in (A.11). This reduces the problem to determining the second factor, which is of the form

$$f(\boldsymbol{\beta}, H, \boldsymbol{h}) = \mathrm{Tr}\left[e^{i\left(\frac{1}{2}\boldsymbol{a}^\dagger H \boldsymbol{a} + \boldsymbol{h}^\dagger \cdot \boldsymbol{a}\right)} \, D_\beta\right] , \tag{A.18}$$

where H, $\boldsymbol{h}$ have absorbed the λ factor in front of G, $\boldsymbol{g}$. Shifting the boson operators by a constant $\boldsymbol{s} = -H^{-1}\boldsymbol{h}$ gives

$$f(\boldsymbol{\beta}, H, \boldsymbol{h}) = \exp\left(-i\frac{1}{2}\boldsymbol{h}^\dagger \, H^{-1}\boldsymbol{h} - \boldsymbol{h}^\dagger \, H^{-1}\Sigma^z \boldsymbol{\beta}\right) f(\boldsymbol{\beta}, H, 0) . \tag{A.19}$$

We can now use a splitting formula derived in Appendix D of [1] to write the second factor as

$$\begin{aligned} f(\boldsymbol{\beta}, H, 0) &= \mathrm{Tr}\Big[e^{i\left(\frac{1}{2}\boldsymbol{a}^\dagger H \boldsymbol{a} + \boldsymbol{A}^\dagger \cdot \boldsymbol{a}\right)}\Big] \exp\left(iB\right) \ , \\ \boldsymbol{A}^\dagger &= \left(-\boldsymbol{\beta}^\dagger \Sigma^z\right) \left[\exp\left(i\,\Sigma^z H\right) - \mathbb{I}\right]^{-1} \left(\Sigma^z H\right) \ , \\ B &= \frac{1}{2}\left(\boldsymbol{A}^\dagger H^{-1}\right) \left[H - \Sigma^z \sin\left(\Sigma^z H\right)\right] \left(H^{-1} \boldsymbol{A}\right) \ . \end{aligned} \tag{A.20}$$

Noting that $\boldsymbol{A}$ retains the symmetry $\boldsymbol{A}^\dagger = \boldsymbol{A}^T \Sigma^x$ of $\boldsymbol{\beta}$ we can perform a final shift to a new set of canonical bosons $\boldsymbol{b}$

$$\mathrm{Tr}\Big[e^{i\left(\frac{1}{2}\boldsymbol{a}^\dagger H \boldsymbol{a} + \boldsymbol{A}^\dagger \cdot \boldsymbol{a}\right)}\Big] = e^{-\frac{i}{2}\boldsymbol{A}^\dagger H^{-1} \boldsymbol{A}}\ \mathrm{Tr}\Big[e^{\frac{i}{2}\boldsymbol{b}^\dagger H \boldsymbol{b}}\Big] \ . \tag{A.21}$$

Putting everything together we obtain

$$f(\boldsymbol{\beta}, H, \boldsymbol{h}) = Z_G \exp\left[-\frac{1}{2}\boldsymbol{\beta}^\dagger \Sigma^z \Delta_G \Sigma^z \boldsymbol{\beta} + \boldsymbol{\omega}_G^\dagger \Sigma^z \boldsymbol{\beta}\right] \ , \tag{A.22}$$

where

$$\begin{aligned} \boldsymbol{\omega}_G = -G^{-1}\boldsymbol{g} \ , \qquad \Delta_G(\lambda) &= -\frac{1}{2}\coth\left(i\lambda\frac{1}{2}\Sigma^z G\right)\Sigma^z \ , \\ Z_G(\lambda) = \exp\left(-i\lambda\frac{1}{2}\boldsymbol{g}^\dagger\, G^{-1}\boldsymbol{g}\right) &\mathrm{Tr}\Big[e^{i\lambda\frac{1}{2}\boldsymbol{b}^\dagger\, G\, \boldsymbol{b}}\Big] \ . \end{aligned} \tag{A.23}$$

The first complication in evaluating the trace in $Z_G(\lambda)$ is that in general $\boldsymbol{b}^\dagger\, G\, \boldsymbol{b}$ cannot be diagonalized by a transformation to canonical bosons. It is however possible to diagonalize these generic quadratic forms by introducing a set of "almost canonical" bosons, which provide us with a generic formula to calculate the trace needed, see Appendix D of [1]. The second complication is that the trace in $Z_G(\lambda)$ is in general not well defined. However, we know from Section 2.2.1 that $\chi(\lambda)$ is bounded and well-defined for any R, given the presence of the physical density matrix ρ. This allows one to introduce an infinitesimal regularization when evaluating $Z_G(\lambda)$. Hence, the final result for $Z_G(\lambda)$ follows directly from the trace formula derived in Appendix D of [1], and is given by

$$Z_G(\lambda) = \exp\left(-i\lambda\frac{1}{2}\boldsymbol{g}^\dagger\, G^{-1}\boldsymbol{g}\right) \mathrm{Det}\left[2\,\Sigma^z \sinh\left(-i\lambda\frac{1}{2}\Sigma^z G\right)\right]^{-1/2} \ . \tag{A.24}$$

Substituting (A.17) and the expression (A.22) for $f(-\boldsymbol{\beta}, \lambda G, \lambda \boldsymbol{g})$ back into (A.16) we obtain

$$\begin{aligned}\chi(\lambda) &= Z_G \frac{1}{\pi^\ell} \int d^2\boldsymbol{\beta} \, \exp\left[-\frac{1}{2}\boldsymbol{\beta}^\dagger \Sigma^z \left(\Delta + \Delta_G\right) \Sigma^z \boldsymbol{\beta} + \left(\boldsymbol{\omega}^\dagger - \boldsymbol{\omega}_G^\dagger\right) \Sigma^z \boldsymbol{\beta}\right] = \\ &= \frac{Z_G}{\sqrt{\mathrm{Det}\left(\Delta + \Delta_G\right)}} \exp\left[-\frac{1}{2}\left(\boldsymbol{\omega}^\dagger - \boldsymbol{\omega}_G^\dagger\right)\left(\Delta + \Delta_G\right)^{-1}\left(\boldsymbol{\omega} - \boldsymbol{\omega}_G\right)\right] ,\end{aligned} \tag{A.25}$$

which is the result (2.13) stated in the main text. The last equality follows from standard Gaussian integrals [161] when we transform the integration from complex to real variables $\mathbf{z}$ by

$$\boldsymbol{\beta} = S\,\mathbf{z} \qquad S \equiv \frac{1}{\sqrt{2}}\begin{pmatrix} \mathbb{I}_{\ell\times\ell} & i\,\mathbb{I}_{\ell\times\ell} \\ \mathbb{I}_{\ell\times\ell} & -i\,\mathbb{I}_{\ell\times\ell}\end{pmatrix} = \left(S^\dagger\right)^{-1} . \tag{A.26}$$

The convergence of the integral for any choice of the Hermitian matrix G in (A.12) is a consequence of the fact that $S^\dagger\left(\Delta + \Delta_G\right) S$ is a complex symmetric matrix with positive-definite real part[1].

So far we have assumed that G is invertible. If G is singular we introduce a regulator ε such that $\det(G_\varepsilon) \neq 0$. We then replace

$$\left(\Delta + \Delta_{G_\varepsilon}\right)^{-1} = -i\lambda\, G_\varepsilon + G_\varepsilon\, M_{G_\varepsilon}\, G_\varepsilon\ , \tag{A.27}$$

where M_{G_ε} is non-singular in the limit $\varepsilon \to 0$. Given that

$$\Sigma^z \sinh\left(-i\lambda\frac{1}{2}\,\Sigma^z G_\varepsilon\right) = G_\varepsilon\, L_{G_\varepsilon} \qquad L_{G_\varepsilon} \text{ non-singular for } \varepsilon \to 0\ , \tag{A.28}$$

one can easily verify that all terms formally ill-defined in (A.25) for $\varepsilon \to 0$ exactly cancel.

---

[1] The positive-definiteness of the real part ensures convergence and the formula can be proved for complex matrices by analytic continuation from the real matrices formula [324].

B

Appendices for Chapter 3

B.1 Proof of 2-colour connectivity

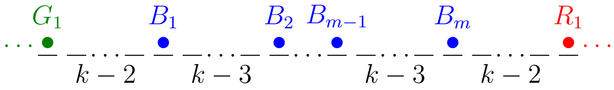

Figure B.1: Configuration of particles in an FES from Fig. 3.3(b)-(c), which leads to the formation of a type-2 blockage. Regions separated by a type-2 edge (i.e. a sequences of $k-2$ holes in an FES) host particles of different colour. We name the m particles in the blue region $B_1, \ldots, B_m$, while the right-most green particle and left-most red particle are respectively $G1$ and $R1$.

It is enough to prove the statement for a subregion of the chain containing 3 colours, as the result trivially generalises to the whole system. We can thus refer to the particle configurations, colours, and labels from Fig. B.1. We start by noticing that because of uniqueness of the FES, any given configuration in a Krylov sector can be reached starting from the FES and performing only inward hops. Call "central" region the one consisting of the two type-2 edges (sequences of $k-2$ holes) and all the sites between them. Assume that there is a configuration of particles $\mathcal{C}$ in the Krylov sector that violates the 2-colour connectivity. This means that wherever in the central region we place a cut between two sites, during the series of inward hops from the FES to $\mathcal{C}$ there must be at least one inward hop that involves a particle on the left and one on the right of the cut. This implies that at least one inward hop involving G_1 and B_1 from Fig. B.1 must occur before these interact with any other particle, otherwise a sequence of $k-1$ holes is created between them, preventing any future inward hop between the two. Thus, at some point during the series of inward hops, B_1 is moved for the first time and goes at least one site to its left. This necessarily creates a separation of $k-2$ or more holes between B_1 and B_2. Given the assumption about $\mathcal{C}$, this separation must necessarily be of $k-2$ holes. We can now repeat the same reasoning used for G_1 and B_1, for B_1 and B_2. In this way we keep propagating to the right a sequence of $k-2$ holes[1]. Thus, at some point two sequences of $k-2$ holes must be next to each other, with a single particle in the middle that has not been part of any inward hop yet. By the assumption about $\mathcal{C}$, the particle in the middle must perform an inward hop, and this necessarily creates a sequence of $k-1$ holes. By placing a cut anywhere between two sites that are part of this sequence of $k-1$ holes, we contradict the assumption about $\mathcal{C}$. This concludes the proof.

B.2 Details of the full proof

To conclude the proof from Section 3.4.3 we present here technical details that properly address "Case 3". We start by generalizing the inequality between $\eta_d(\nu)$ and $g_{d,\nu}(p,s)$ of Eq. (3.13) to the case in which we take into account the dipole moment. Consider a symmetry sector of the chain characterized by $N=\nu L$ and $X=\nu_x \nu L^2$ and create a bipartition into two subregions of size sL and $(1-s)L$. Say that the first of the two subregions has $N_1 = pL$ particles and dipole moment $X_1 = x\,p\,s\,L^2$. The second subregion has N_2, X_2 such that $N_1+N_2=N$ and $X_1+X_2=X$. Define $\tilde{g}_{d,\nu,\nu_x}(p,x,s)$ as

$$\tilde{g}_{d,\nu,\nu_x}(p,x,s) = \lim_{L\to\infty}\frac{1}{L}\ln \widetilde{W}_d \qquad \widetilde{W}_d = D^{(d)}_{N_1,X_1}(sL)\,D^{(d)}_{N_2,X_2}(L-sL)\ , \tag{B.1}$$

where $\widetilde{W}_d$ is the total number of particle configurations compatible with the bipartition. Given that everyone of these $\widetilde{W}_d$ configurations is also a configuration

---

[1] Clearly, by analogous reasoning the sequence of $k-2$ holes that originally separate B_m from R_1 must propagate to the left.

of the global (N, X) sector chosen, using Eq. (3.10) and taking the thermodynamic limit one arrives to

$$\eta_d(\nu) - \Lambda_d(\nu, \nu_x) \geq \tilde{g}_{d,\nu,\nu_x}(p, x, s) \ , \tag{B.2}$$

for any p, x and s in their respective domains. The inequality (B.2) trivially generalises to the case in which we partition the system into more than 2 subregions.

As we have seen in Section 3.4.3, Case 3 implies, in addition to having a zero fraction f of frozen sites being part of type-1 blockages, that any extensive subregion of the chain has local filling approaching the global ν for large L values. We now exploit a trivial property of the FES picture starting from any state of the system S with on-site dimension d: *if an extensive subregion of the chain is enclosed by two blockages of either type-1 or type-2 of $o(L)$ size, then for asymptotically large L values this region has identical local filling in the FES of the auxiliary system $\tilde{S}$ and in the chosen state of the system S.*

This provides us with an algorithm to partition the system as in Fig. 3.5, i.e. into G subregions $\mathcal{A}_i$ that are separated by type-2 blockages $\mathcal{B}_i$ of L-independent size. The first subregion $\mathcal{A}_1$ must necessarily have size ℓ_1 scaling as $\mathcal{O}(L^{\gamma_1})$, with $0 \leq \gamma_1 < 1$. Indeed, assume for the sake of contradiction that the first L-independent in size type-2 blockage is encountered only extensively far away from from the left boundary, and so $\ell_1 = \mathcal{O}(L)$. This means that either $\mathcal{A}_1$ does not possess type-2 edges at all or that the ones present are at least an $\mathcal{O}(h(L))$ apart from each other, with $h(L)$ a function that diverges for $L \to \infty$. This would however imply that for large L the local filling in $\mathcal{A}_1$ is greater or equal to ν_c, which is not possible given the condition of having local filling equal to ν, i.e. lower than ν_c, in any extensive subregion of the chain. Exactly the same reasoning can be applied to all the remaining $\mathcal{A}_i$ regions. In particular, after each blockage $\mathcal{B}_{i-1}$ we try to look for the next type-2 blockage of L-independent size at a fixed distance $\ell = \mathcal{O}(L^0)$ to the right of $\mathcal{B}_{i-1}$, with $\ell \gg 1$. If no such blockage is found at such ℓ distance, we keep scanning to the right, until we find $\mathcal{B}_i$ at a distance ℓ_i from $\mathcal{B}_{i-1}$. From the argument above we are guaranteed that for any subregion $\mathcal{A}_i$ the size $\ell_i \geq \ell$

is subextensive, i.e. it scales as $\ell_i = \mathcal{O}(L^{\gamma_i})$ for some $0 \leq \gamma_i < 1$. We can now generalize Eq. (3.20) from Section 3.4.3 to the multipartite case as

$$\mathcal{D}_{\max}^{(d,k)} < D_{\mathcal{A}_1+\mathcal{B}_1}^{(d)} \left[\prod_{i=2}^{G-1} D_{\mathcal{B}_{i-1}+\mathcal{A}_i+\mathcal{B}_i}^{(d)} \right] D_{\mathcal{B}_{G-1}+\mathcal{A}_G}^{(d)} \, . \tag{B.3}$$

Using the analogue of (3.21) in the multipartite case we get

$$\mathcal{D}_{\max}^{(d,k)} < Q^{G-1} \left[\prod_{i=1}^{G-1} D_{\mathcal{A}_i+\mathcal{B}_i}^{(d)} \right] D_{\mathcal{A}_G}^{(d)} \, , \tag{B.4}$$

where Q is again an L-independent positive constant. The right-hand side of the previous inequality involves the total number of configurations in a partition of the chain into G regions that cannot exchange particles and dipole moment with each other. Using Eq. (3.10) together with the generalization of Eq. (B.2) to the multipartite case, we obtain

$$r_{N,X}^{(d,k)} < L^2 \prod_{i=1}^{G} \frac{\widetilde{Q}}{\ell_i^2} \, . \tag{B.5}$$

Here $\widetilde{Q}$ is an L-indepdendent positive constant that has absorbed the Q factors from (B.4) and the $\mathcal{O}(L^0)$ constants arising from the use of (3.10) on every $D_{\mathcal{A}_i+\mathcal{B}_i}^{(d)}$ and on $D_{N,X}^{(d)}$ from (3.6). Importantly, we choose the L-independent distance ℓ to be much larger than the size of any $\mathcal{B}_i$. In this way we can always guarantee that $\ell_i^2 \geq \ell^2 > \widetilde{Q}$. We see that if G is extensively large, i.e. if after applying the subdivision algorithm we find among the set of all $\mathcal{A}_i$ regions a subset of extensively many sizes $\ell_i = \mathcal{O}(L^0)$, then $r_{N,X}^{(d,k)}$ in Eq. (B.5) decays to zero exponentially with L. The fact that $G = \mathcal{O}(L)$ is guaranteed by our requirement of having an extensive number of type-2 edges in the system (given that Case 3 requires a zero fraction of type-1 blockages). Indeed, assume by contradiction that $G = \mathcal{O}(L^{\gamma_g})$, with $\gamma_g < 1$. The total number of type-2 edges in the system are obtained by summing the following contributions: (i) two edges per $\mathcal{B}_i$ blockage and at most $\mathcal{O}(L^0)$ edges per each $\mathcal{A}_i$ region with size $\ell_i = \mathcal{O}(L^0)$; (ii) at most $\ell_i/h(L)$ edges in each $\mathcal{A}_i$ region of size $\ell_i = \mathcal{O}(L^{\gamma_i})$ with $0 < \gamma_i < 1$. Here $h(L)$ is again a function that diverges for $L \to \infty$. Summing these contributions under the assumption of a subextensive G yields a subextensive number of type-2 edges in the chain, which contradicts our requirements of having an extensive number of them. Hence $G = \mathcal{O}(L)$ and $r_{N,X}^{(d,k)}$ decays exponentially with L.

C

Appendices for Chapter 4

C.1 Details of Markov Chain Monte Carlo sampling

Given that $|\mu\rangle$ eigenstates with $N-1$ particles (N even) are in one-to-one correspondence with the sets of $N-1$ distinct integers $\{J_j\}_{j=1}^{N-1}$ that enter the Bethe equations Eq. (4.4), we can directly perform sampling over the space of integers. In particular, we can implement a Markov process with stationary distribution that coincides with $\mathcal{P}_\lambda(\mu) = \exp(-M_{\lambda,\mu})/Z_\lambda$ from Eq. (4.38).

We start by recollecting a few elementary results from the theory of Markov processes [308, 310]. Consider a finite set $\mathcal{E} = (x_1, x_2, \dots, x_R)$ and a stochastic variable $X^{(\ell)}$ that takes values in $\mathcal{E}$ at discrete steps ℓ. In our case, each x_i denotes a set of $N-1$ distinct integers $\{J_j\}$, and we guarantee finiteness of $\mathcal{E}$ by imposing any arbitrarily-large cutoff $J_{\max}$ on $\max|J_j|$. Consider a Markov chain on $\mathcal{E}$ with transition matrix T_{ij} defined as the probability of transitioning from x_i to x_j in one time step, that is, $\mathbb{P}(X^{(\ell+1)} = x_j | X^{(\ell)} = x_i) = T_{ij}$, where $\mathbb{P}(\cdot|\cdot)$ indicates conditional probability. If we call $\pi_i^{(\ell)}$ the probability associated with $X^{(\ell)} = x_i$, we have

$$\pi^{(\ell)} = \pi^{(0)} T^\ell \qquad \pi^{(\ell)} = (\pi_1^{(\ell)}, \pi_2^{(\ell)}, \dots, \pi_R^{(\ell)}) \,, \tag{C.1}$$

where by construction $\sum_{i=1}^R \pi_i^{(\ell)} = 1$. Consider transitions matrices T that are irreducible and aperiodic [310]. Then, there exists a limiting distribution $\lim_{\ell\to\infty} \pi^{(\ell)} \equiv$

π given by the unique solution of $\pi = \pi T$. A simple way of constructing a Markov chain with stationary distribution π is to require that T satisfies the detailed balance condition

$$\pi_i T_{ij} = \pi_j T_{ji} \; . \tag{C.2}$$

In our context, π represents the target distribution $\mathcal{P}_\lambda(\mu)$. To construct a T that satisfies detailed balance one can employ the Metropolis-Hastings algorithm [306–308]. This allows to (approximately) generate samples $X^{(\ell)}$ from the target distribution π, by letting ℓ run up to large values. The Metropolis-Hastings construction is based on a proposal matrix w_{ij}, which denotes the probability of proposing the move $X^{(\ell)} = x_i \to X^{(\ell+1)} = x_j$, and on accepting or refusing it with probability, respectively, α_{ij} and $1 - \alpha_{ij}$. This is defined as

$$\alpha_{ij} = \min\left[\frac{\pi_j\, w_{ji}}{\pi_i\, w_{ij}}, 1\right] \; . \tag{C.3}$$

It is easy to see that the overall transition matrix T for this Markov process, given by

$$T_{ij} = w_{ij}\,\alpha_{ij} \quad i \neq j \qquad\qquad T_{ii} = 1 - \sum_{\substack{j \\ (j\neq i)}} w_{ij}\alpha_{ij} \; , \tag{C.4}$$

satisfies the detailed balance of Eq. (C.2). This implies that, if we choose w_{ij} in such a way that T is irreducible and aperiodic, then at large steps ℓ the stochastic variable $X^{(\ell)}$ will be sampled according to π, irrespective of the initial value $X^{(0)}$.

Given that each $X^{(\ell)}$ represents a set of integers $\{J_j^{(\ell)}\}$, we can construct a proposal matrix w_{ij} for single-integer updates (i.e. single particle-hole excitations). In particular, for the step $\ell \to \ell + 1$ we select at random one among the $N - 1$ integers $J_j^{(\ell)}$, say $j = s$. We then consider the nearest $Q/2$ *unoccupied* integers both to its right and left (Q even), and select one at random, call it J^* (if we hit the boundaries defined by the cutoff $J_{\max}$ we wrap around, but in practice $J_{\max}$ can be chosen large enough that this never happens). It is clear that the proposal matrix w_{ij} associated with the move $J_s^{(\ell)} \to J^*$ is symmetric, i.e. $w_{ij} = w_{ji}$, and hence it cancels out from the expression (C.3) for the acceptance probability, which only depends on $\pi = \mathcal{P}_\lambda(\mu)$ (this is the original algorithm of [306]). If the move is accepted we update $J_s^{(\ell+1)} = J^*$, otherwise $J_s^{(\ell+1)} = J_s^{(\ell)}$. We note that our choice of w_{ij} yields an overall T which is irreducible and aperiodic, as we required.

For the data presented in the main text, we have: (i) tuned the value of Q such to always have an average acceptance rate of around 10% or higher; (ii) verified that irrespective of the initial set $\{J_j^{(0)}\}$ chosen, the Markov chain always ends up sampling from the same distribution (which appears stationary) at large-enough times[1]; (iii) discarded a "burn-in" number of initial steps, where we set $\ell_{\text{burn}-\text{in}}$ to be 1/11 of the total number of MCMC steps $\ell_{\text{burn}-\text{in}} + \ell_{\max}$; (iv) extracted the statistical uncertainty on the final MCMC data by computing the standard error on the mean associated with the output of C Markov chains run in parallel (where usually we set $C = 100$), and found that the uncertainties obtained were negligible in all regimes of physical interest.

C.2 Reconstructing $\widetilde{C}(k, \omega)$

The correlation function $\widetilde{C}(k, \omega)$ in Fourier space is given by Eq. (4.41). At any finite L it consists of a sum of Dirac delta peaks centred around the energy difference $E_\mu - E_\lambda$. Due to this, it is more convenient to sample an integral of $\widetilde{C}(k, \omega)$ over the frequency

$$\widetilde{C}_{\text{int}}(k, \omega) = \int_{-\infty}^{\omega} dy\, \widetilde{C}(k, y) = 2\pi L \sum_{\mu} \theta_H(\omega - E_\mu + E_\lambda)\, \delta_{k, P_\mu - P_\lambda}\, |\, \langle \mu | \phi(0,0) | \lambda \rangle\, |^2 \,, \tag{C.5}$$

where θ_H is the Heaviside step function. Fixed k, the curve $\widetilde{C}_{\text{int}}(k, \omega)$ as a function of ω consists of many discrete steps of height $\propto |\, \langle \mu | \phi(0,0) | \lambda \rangle\, |^2 = e^{-M_{\lambda,\mu}}$ separated by a distance $\delta\omega \sim D_\mu(E)^{-1}$, where $D_\mu(E)$ indicates the density of $|\mu\rangle$ states in energy (which grows exponentially with L at any finite energy density). However, if one resolves the curve $\widetilde{C}_{\text{int}}(k, \omega)$ (k fixed) only on a finite grid of ω values with $\Delta\omega_{\text{grid}} \gg \delta\omega$, it appears to be smooth, enabling a direct comparison with the smooth function $\lim_{L\to\infty} \widetilde{C}_{\text{int}}(k, \omega)$ in the thermodynamic limit.

---

[1] This was achieved by monitoring the values of $M_{\lambda,\mu}$ as in Fig. 4.1, as well as those for the energies E_μ and momenta P_μ.

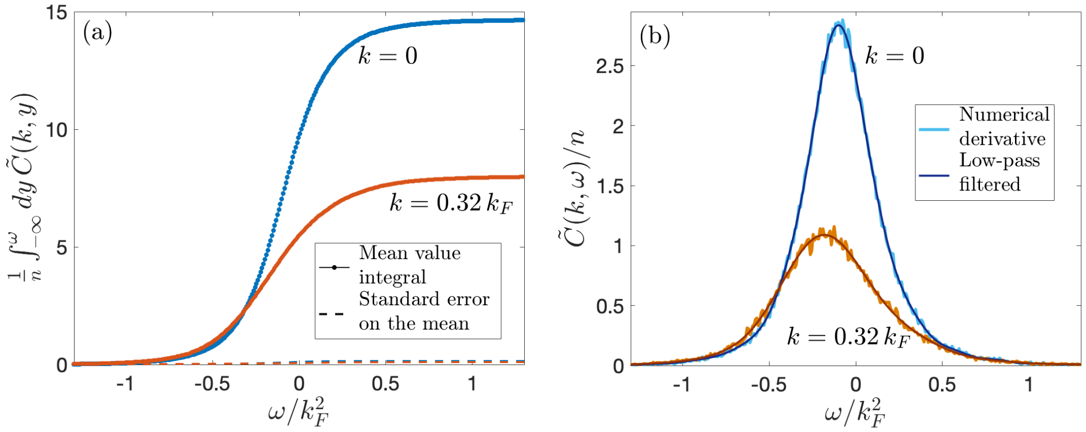

Figure C.1: (a) $\widetilde{C}_{\text{int}}(k,\omega) = \int_{-\infty}^{\omega} dy\, \widetilde{C}(k,y)$ obtained by running 100 parallel Markov chains with $\ell_{\max} = 10^6$ MCMC steps each at $\tau = 5, \gamma = 4, L = 200$. The dots represent the average of each (k,ω) point over the 100 runs, while the dashed lines indicate the standard error on the mean. (b) $\widetilde{C}(k,\omega)$ obtained by performing a spline interpolation of $\widetilde{C}_{\text{int}}(k,\omega)$ (k fixed) and computing its ω derivative (bright lines). The noise in the curves can be removed by using a simple low-pass filter (dark lines).

Similarly to Eq. (4.40), $\widetilde{C}_{\text{int}}(k,\omega)$ can be estimated on the k and ω grids via MCMC. In Fig. C.1 we plot $\widetilde{C}_{\text{int}}(k,\omega)$ for $\tau = 5, \gamma = 4$ and $L = 200$. At each k value, the curve as a function of ω appears to be smooth, and the statistical fluctuations around the average are negligible. To obtain $\widetilde{C}(k,\omega) = d\widetilde{C}_{\text{int}}(k,\omega)/d\omega$ we compute a numerical derivative by first performing a spline interpolation of $\widetilde{C}_{\text{int}}(k,\omega)$ at each k, and then taking the derivative of the smooth spline function $f_k(\omega)$. In Fig. C.1(b) we plot $df_k(\omega)/d\omega$ (bright lines) obtained in this way from the curves in (a). On top of the smooth profile it is evident the presence of some noise[2] arising from the small but nonzero statistical fluctuations in the MCMC values for $\widetilde{C}_{\text{int}}(k,\omega)$. To obtain a smooth Fourier correlator $\widetilde{C}(k,\omega)$ (appropriate for comparisons with $L \to \infty$ limit) we filter out the high-“frequency” components characteristic of the noise (where here “frequency” refers to the Fourier conjugate of ω, i.e. time). As evident from Fig. C.1(b) the filtered curves (dark lines) perfectly capture the smooth profile of the original derivatives $df_k(\omega)/d\omega$.

---

[2] This is a consequence of the fact that, by construction, spline interpolations are designed to pass directly through each given data point.

Bibliography

[1] R. Senese, J. H. Robertson, and F. H. L. Essler, Out-of-equilibrium full counting statistics in Gaussian theories of quantum magnets, *SciPost Phys.* 17, 139 (2024).

[2] J. Classen-Howes, R. Senese, and A. Prakash, Universal freezing transitions of dipole-conserving chains, *Phys. Rev. B* 112, 125148 (2025).

[3] R. Senese and F. H. Essler, Finite temperature single-particle Green's function in the Lieb-Liniger model, *arXiv preprint arXiv:2508.17908* (2025).

[4] I. Bloch, J. Dalibard, and W. Zwerger, Many-body physics with ultracold gases, *Rev. Mod. Phys.* 80, 885–964 (2008).

[5] R. Blatt and C. F. Roos, Quantum simulations with trapped ions, *Nature Physics* 8(4), 277–284 (2012).

[6] A. A. Houck, H. E. Türeci, and J. Koch, On-chip quantum simulation with superconducting circuits, *Nature Physics* 8(4), 292–299 (2012).

[7] I. Bloch, J. Dalibard, and S. Nascimbène, Quantum simulations with ultracold quantum gases, *Nature Physics* 8(4), 267–276 (2012).

[8] I. M. Georgescu, S. Ashhab, and F. Nori, Quantum simulation, *Rev. Mod. Phys.* 86, 153–185 (2014).

[9] T. Langen, R. Geiger, and J. Schmiedmayer, Ultracold Atoms Out of Equilibrium, *Annual Review of Condensed Matter Physics* 6(Volume 6, 2015), 201–217 (2015).

[10] C. D. Bruzewicz et al., Trapped-ion quantum computing: Progress and challenges, *Applied Physics Reviews* 6(2), 021314 (2019).

[11] A. Browaeys and T. Lahaye, Many-body physics with individually controlled Rydberg atoms, *Nature Physics* 16(2), 132–142 (2020).

[12] E. Altman et al., Quantum Simulators: Architectures and Opportunities, *PRX Quantum* 2, 017003 (2021).

[13] S. Weinberg, *Lectures on Quantum Mechanics*, 2nd ed., Cambridge University Press, 2015.

[14] P. Calabrese and J. Cardy, Evolution of entanglement entropy in one-dimensional systems, *J. Stat. Mech.* 2005(04), P04010 (2005).

[15] P. Calabrese and J. Cardy, Time Dependence of Correlation Functions Following a Quantum Quench, *Phys. Rev. Lett.* 96, 136801 (2006).

[16] M. A. Nielsen and I. L. Chuang, *Quantum Computation and Quantum Information*, Cambridge University Press, 2010.

[17] J. Eisert, M. Cramer, and M. B. Plenio, Colloquium: Area laws for the entanglement entropy, *Rev. Mod. Phys.* 82, 277–306 (2010).

[18] S. Weinberg, *The Quantum Theory of Fields*, Cambridge University Press, 1995.

[19] L. D'Alessio et al., From quantum chaos and eigenstate thermalization to statistical mechanics and thermodynamics, *Advances in Physics* 65(3), 239–362 (2016).

[20] J. M. Deutsch, Thermodynamic entropy of a many-body energy eigenstate, *New Journal of Physics* 12(7), 075021 (2010).

[21] L. F. Santos, A. Polkovnikov, and M. Rigol, Weak and strong typicality in quantum systems, *Phys. Rev. E* 86, 010102 (2012).

[22] J. M. Deutsch, H. Li, and A. Sharma, Microscopic origin of thermodynamic entropy in isolated systems, *Phys. Rev. E* 87, 042135 (2013).

[23] K. Huang, *Statistical mechanics*, John Wiley & Sons, 2008.

[24] E. H. Lieb and D. W. Robinson, The finite group velocity of quantum spin systems, *Communications in mathematical physics* 28(3), 251–257 (1972).

[25] S. Bravyi, M. B. Hastings, and F. Verstraete, Lieb-Robinson Bounds and the Generation of Correlations and Topological Quantum Order, *Phys. Rev. Lett.* 97, 050401 (2006).

[26] R. Kubo, Statistical-Mechanical Theory of Irreversible Processes. I. General Theory and Simple Applications to Magnetic and Conduction Problems, *Journal of the Physical Society of Japan* 12(6), 570–586 (1957).

[27] G. D. Mahan, *Many-Particle Physics*, Springer Science & Business Media, 2000.

[28] E. Ott, *Chaos in Dynamical Systems*, 2nd ed., Cambridge University Press, 2002.

[29] A. J. Lichtenberg and M. A. Lieberman, *Regular and chaotic dynamics*, vol. 38, Springer Science & Business Media, 2013.

[30] F. Haake, *Quantum signatures of chaos*, Springer, 1991.

[31] E. P. Wigner, Characteristic Vectors of Bordered Matrices With Infinite Dimensions, *Annals of Mathematics* 62(3), 548–564 (1955).

[32] E. P. Wigner, On the Distribution of the Roots of Certain Symmetric Matrices, *Annals of Mathematics* 67(2), 325–327 (1958).

[33] F. J. Dyson, Statistical Theory of the Energy Levels of Complex Systems. I, *Journal of Mathematical Physics* 3(1), 140–156 (1962).

[34] O. Bohigas, M. J. Giannoni, and C. Schmit, Characterization of Chaotic Quantum Spectra and Universality of Level Fluctuation Laws, *Phys. Rev. Lett.* 52, 1–4 (1984).

[35] G. Casati, F. Valz-Gris, and I. Guarnieri, On the connection between quantization of nonintegrable systems and statistical theory of spectra, *Lettere al Nuovo Cimento (1971-1985)* 28(8), 279–282 (1980).

[36] G. Casati et al., "Stochastic behavior of a quantum pendulum under a periodic perturbation", *Stochastic Behavior in Classical and Quantum Hamiltonian Systems*, ed. by G. Casati and J. Ford, Berlin, Heidelberg: Springer Berlin Heidelberg, 1979, 334–352.

[37] M. V. Berry and M. Tabor, Level clustering in the regular spectrum, *Proceedings of the Royal Society of London. A. Mathematical and Physical Sciences* 356(1686), 375–394 (1977).

[38] M. C. Gutzwiller, Periodic Orbits and Classical Quantization Conditions, *Journal of Mathematical Physics* 12(3), 343–358 (1971).

[39] M. L. Mehta, *Random matrices*, Elsevier, 2004.

[40] V. Zelevinsky et al., The nuclear shell model as a testing ground for many-body quantum chaos, *Physics Reports* 276(2), 85–176 (1996).

[41] L. F. Santos and M. Rigol, Onset of quantum chaos in one-dimensional bosonic and fermionic systems and its relation to thermalization, *Phys. Rev. E* 81, 036206 (2010).

[42] L. Vidmar and M. Rigol, Entanglement Entropy of Eigenstates of Quantum Chaotic Hamiltonians, *Phys. Rev. Lett.* 119, 220603 (2017).

[43] T. LeBlond et al., Entanglement and matrix elements of observables in interacting integrable systems, *Phys. Rev. E* 100, 062134 (2019).

[44] E. Bianchi et al., Volume-Law Entanglement Entropy of Typical Pure Quantum States, *PRX Quantum* 3, 030201 (2022).

[45] J. M. Deutsch, Quantum statistical mechanics in a closed system, *Phys. Rev. A* 43, 2046–2049 (1991).

[46] M. Srednicki, Chaos and quantum thermalization, *Phys. Rev. E* 50, 888–901 (1994).

[47] M. Srednicki, The approach to thermal equilibrium in quantized chaotic systems, *J. Phys. A: Math. Gen.* 32(7), 1163 (1999).

[48] J. M. Deutsch, Eigenstate thermalization hypothesis, *Reports on Progress in Physics* 81(8), 082001 (2018).

[49] M. Rigol, V. Dunjko, and M. Olshanii, Thermalization and its mechanism for generic isolated quantum systems, *Nature* 452(7189), 854–858 (2008).

[50] F. H. L. Essler and M. Fagotti, Quench dynamics and relaxation in isolated integrable quantum spin chains, *Journal of Statistical Mechanics: Theory and Experiment* 2016(6), 064002 (2016).

[51] C. Gogolin and J. Eisert, Equilibration, thermalisation, and the emergence of statistical mechanics in closed quantum systems, *Reports on Progress in Physics* 79(5), 056001 (2016).

[52] J. M. Deutsch, Eigenstate thermalization hypothesis, *Reports on Progress in Physics* 81(8), 082001 (2018).

[53] M. Ueda, Quantum equilibration, thermalization and prethermalization in ultracold atoms, *Nature Reviews Physics* 2(12), 669–681 (2020).

[54] J. R. Garrison and T. Grover, Does a Single Eigenstate Encode the Full Hamiltonian?, *Phys. Rev. X* 8, 021026 (2018).

[55] A. Dymarsky, N. Lashkari, and H. Liu, Subsystem eigenstate thermalization hypothesis, *Phys. Rev. E* 97, 012140 (2018).

[56] A. M. Läuchli and C. Kollath, Spreading of correlations and entanglement after a quench in the one-dimensional Bose–Hubbard model, *J. Stat. Mech.* 2008(05), P05018 (2008).

[57] M. Fagotti and P. Calabrese, Evolution of entanglement entropy following a quantum quench: Analytic results for the XY chain in a transverse magnetic field, *Phys. Rev. A* 78, 010306 (2008).

[58] N. Schuch et al., On entropy growth and the hardness of simulating time evolution, *New Journal of Physics* 10(3), 033032 (2008).

[59] P. Calabrese and J. Cardy, Entanglement entropy and conformal field theory, *J. Phys. A: Math. Theor.* 42(50), 504005 (2009).

[60] H. Kim and D. A. Huse, Ballistic Spreading of Entanglement in a Diffusive Nonintegrable System, *Phys. Rev. Lett.* 111, 127205 (2013).

[61] P. Hauke and L. Tagliacozzo, Spread of Correlations in Long-Range Interacting Quantum Systems, *Phys. Rev. Lett.* 111, 207202 (2013).

[62] J. Schachenmayer et al., Entanglement Growth in Quench Dynamics with Variable Range Interactions, *Phys. Rev. X* 3, 031015 (2013).

[63] A. S. Buyskikh et al., Entanglement growth and correlation spreading with variable-range interactions in spin and fermionic tunneling models, *Phys. Rev. A* 93, 053620 (2016).

[64] V. Alba and P. Calabrese, Entanglement and thermodynamics after a quantum quench in integrable systems, *Proceedings of the National Academy of Sciences* 114(30), 7947–7951 (2017).

[65] W. W. Ho and D. A. Abanin, Entanglement dynamics in quantum many-body systems, *Phys. Rev. B* 95, 094302 (2017).

[66] F. Verstraete, V. Murg, and J. I. Cirac, Matrix product states, projected entangled pair states, and variational renormalization group methods for quantum spin systems, *Advances in Physics* 57(2), 143–224 (2008).

[67] U. Schollwöck, The density-matrix renormalization group in the age of matrix product states, *Annals of Physics* 326(1), 96–192 (2011).

[68] J. I. Cirac et al., Matrix product states and projected entangled pair states: Concepts, symmetries, theorems, *Rev. Mod. Phys.* 93, 045003 (2021).

[69] R. Mondaini et al., Comment on "Systematic Construction of Counterexamples to the Eigenstate Thermalization Hypothesis", *Phys. Rev. Lett.* 121, 038901 (2018).

[70] N. Yunger Halpern et al., Microcanonical and resource-theoretic derivations of the thermal state of a quantum system with noncommuting charges, *Nature Communications* 7(1), 12051 (2016).

[71] N. Yunger Halpern, M. E. Beverland, and A. Kalev, Noncommuting conserved charges in quantum many-body thermalization, *Phys. Rev. E* 101, 042117 (2020).

[72] S. Majidy et al., Noncommuting conserved charges in quantum thermodynamics and beyond, *Nature Reviews Physics* 5(11), 689–698 (2023).

[73] C. Murthy et al., Non-Abelian Eigenstate Thermalization Hypothesis, *Phys. Rev. Lett.* 130, 140402 (2023).

[74] J. D. Noh, Eigenstate thermalization hypothesis in two-dimensional XXZ model with or without SU(2) symmetry, *Phys. Rev. E* 107, 014130 (2023).

[75] A. Lasek et al., Numerical evidence for the non-Abelian eigenstate thermalization hypothesis, *arXiv preprint arXiv:2412.07838* (2024).

[76] R. Patil and M. Rigol, Eigenstate thermalization in spin-$\frac{1}{2}$ systems with SU(2) symmetry, *Phys. Rev. B* 111, 205126 (2025).

[77] L. Foini and J. Kurchan, Eigenstate thermalization hypothesis and out of time order correlators, *Phys. Rev. E* 99, 042139 (2019).

[78] S. Pappalardi, L. Foini, and J. Kurchan, Eigenstate Thermalization Hypothesis and Free Probability, *Phys. Rev. Lett.* 129, 170603 (2022).

[79] A. Chan, A. De Luca, and J. T. Chalker, Eigenstate Correlations, Thermalization, and the Butterfly Effect, *Phys. Rev. Lett.* 122, 220601 (2019).

[80] S. Pappalardi, F. Fritzsch, and T. Prosen, Full Eigenstate Thermalization via Free Cumulants in Quantum Lattice Systems, *Phys. Rev. Lett.* 134, 140404 (2025).

[81] D. Hahn, D. J. Luitz, and J. T. Chalker, Eigenstate Correlations, the Eigenstate Thermalization Hypothesis, and Quantum Information Dynamics in Chaotic Many-Body Quantum Systems, *Phys. Rev. X* 14, 031029 (2024).

[82] R. Nandkishore and D. A. Huse, Many-Body Localization and Thermalization in Quantum Statistical Mechanics, *Annual Review of Condensed Matter Physics* 6(1), 15–38 (2015).

[83] D. A. Abanin et al., Colloquium: Many-body localization, thermalization, and entanglement, *Rev. Mod. Phys.* 91, 021001 (2019).

[84] M. Serbyn, D. A. Abanin, and Z. Papić, Quantum many-body scars and weak breaking of ergodicity, *Nature Physics* 17(6), 675–685 (2021).

[85] S. Moudgalya, B. A. Bernevig, and N. Regnault, Quantum many-body scars and Hilbert space fragmentation: a review of exact results, *Reports on Progress in Physics* 85(8), 086501 (2022).

[86] N. Shiraishi and T. Mori, Systematic Construction of Counterexamples to the Eigenstate Thermalization Hypothesis, *Phys. Rev. Lett.* 119, 030601 (2017).

[87] S. Moudgalya, N. Regnault, and B. A. Bernevig, Entanglement of exact excited states of Affleck-Kennedy-Lieb-Tasaki models: Exact results, many-body scars, and violation of the strong eigenstate thermalization hypothesis, *Phys. Rev. B* 98, 235156 (2018).

[88] W. De Roeck et al., Absence of normal heat conduction in strongly disordered interacting quantum chains, *arXiv preprint arXiv:2408.04338* (2024).

[89] J. Z. Imbrie, On Many-Body Localization for Quantum Spin Chains, *Journal of Statistical Physics* 163(5), 998–1048 (2016).

[90] J. Šuntajs et al., Quantum chaos challenges many-body localization, *Phys. Rev. E* 102, 062144 (2020).

[91] D. Abanin et al., Distinguishing localization from chaos: Challenges in finite-size systems, *Annals of Physics* 427, 168415 (2021).

[92] P. Sierant et al., Many-body localization in the age of classical computing*, *Reports on Progress in Physics* 88(2), 026502 (2025).

[93] H. Bethe, Zur theorie der metalle: I. Eigenwerte und eigenfunktionen der linearen atomkette, *Zeitschrift für Physik* 71(3), 205–226 (1931).

[94] V. E. Korepin, N. M. Bogoliubov, and A. G. Izergin, *Quantum Inverse Scattering Method and Correlation Functions*, Cambridge Monographs on Mathematical Physics, Cambridge University Press, 1993.

[95] F. H. L. Essler et al., *The One-Dimensional Hubbard Model*, Cambridge University Press, 2005.

[96] E. Ilievski, M. Medenjak, and T. Prosen, Quasilocal Conserved Operators in the Isotropic Heisenberg Spin-1/2 Chain, *Phys. Rev. Lett.* 115, 120601 (2015).

[97] E. Ilievski et al., Complete Generalized Gibbs Ensembles in an Interacting Theory, *Phys. Rev. Lett.* 115, 157201 (2015).

[98] F. H. L. Essler and A. J. J. M. de Klerk, Statistics of Matrix Elements of Local Operators in Integrable Models, *Phys. Rev. X* 14, 031048 (2024).

[99] V. Alba, Eigenstate thermalization hypothesis and integrability in quantum spin chains, *Phys. Rev. B* 91, 155123 (2015).

[100] F. Rottoli and V. Alba, Eigenstate Thermalization Hypothesis (ETH) for off-diagonal matrix elements in integrable spin chains, *arXiv preprint arXiv:2505.23602* (2025).

[101] M. Rigol et al., Relaxation in a Completely Integrable Many-Body Quantum System: An Ab Initio Study of the Dynamics of the Highly Excited States of 1D Lattice Hard-Core Bosons, *Phys. Rev. Lett.* 98, 050405 (2007).

[102] B. Bertini et al., Prethermalization and Thermalization in Models with Weak Integrability Breaking, *Phys. Rev. Lett.* 115, 180601 (2015).

[103] B. Bertini et al., Thermalization and light cones in a model with weak integrability breaking, *Phys. Rev. B* 94, 245117 (2016).

[104] M. Pandey et al., Adiabatic Eigenstate Deformations as a Sensitive Probe for Quantum Chaos, *Phys. Rev. X* 10, 041017 (2020).

[105] T. LeBlond et al., Universality in the onset of quantum chaos in many-body systems, *Phys. Rev. B* 104, L201117 (2021).

[106] M. Brenes et al., Eigenstate Thermalization in a Locally Perturbed Integrable System, *Phys. Rev. Lett.* 125, 070605 (2020).

[107] S. Moudgalya and O. I. Motrunich, Hilbert Space Fragmentation and Commutant Algebras, *Phys. Rev. X* 12, 011050 (2022).

[108] P. Sala et al., Ergodicity Breaking Arising from Hilbert Space Fragmentation in Dipole-Conserving Hamiltonians, *Phys. Rev. X* 10, 011047 (2020).

[109] V. Khemani, M. Hermele, and R. Nandkishore, Localization from Hilbert space shattering: From theory to physical realizations, *Phys. Rev. B* 101, 174204 (2020).

[110] R. M. Nandkishore and M. Hermele, Fractons, *Annual Review of Condensed Matter Physics* 10(Volume 10, 2019), 295–313 (2019).

[111] M. Pretko, X. Chen, and Y. You, Fracton phases of matter, *International Journal of Modern Physics A* 35(06), 2030003 (2020).

[112] T. Rakovszky et al., Statistical localization: From strong fragmentation to strong edge modes, *Phys. Rev. B* 101, 125126 (2020).

[113] S. Pai, M. Pretko, and R. M. Nandkishore, Localization in Fractonic Random Circuits, *Phys. Rev. X* 9, 021003 (2019).

[114] Y. V. Nazarov, *Quantum noise in mesoscopic physics*, vol. 97, Springer Science & Business Media, 2012.

[115] Y. Blanter and M. Büttiker, Shot noise in mesoscopic conductors, *Physics Reports* 336(1–2), 1–166 (2000).

[116] S. Hofferberth et al., Probing quantum and thermal noise in an interacting many-body system, *Nature Physics* 4(6), 489–495 (2008).

[117] J. Armijo et al., Probing Three-Body Correlations in a Quantum Gas Using the Measurement of the Third Moment of Density Fluctuations, *Phys. Rev. Lett.* 105, 230402 (2010).

[118] T. Kitagawa et al., Ramsey Interference in One-Dimensional Systems: the Full Distribution Function of Fringe Contrast as a Probe of Many-Body Dynamics, *Phys. Rev. Lett.* 104, 255302 (2010).

[119] T. Jacqmin et al., Sub-Poissonian Fluctuations in a 1D Bose Gas: from the Quantum Quasicondensate to the Strongly Interacting Regime, *Phys. Rev. Lett.* 106, 230405 (2011).

[120] T. Kitagawa et al., The dynamics and prethermalization of one-dimensional quantum systems probed through the full distributions of quantum noise, *New Journal of Physics* 13(7), 073018 (2011).

[121] M. Gring et al., Relaxation and Prethermalization in an Isolated Quantum System, *Science* 337(6100), 1318–1322 (2012).

[122] A. Mazurenko et al., A cold-atom Fermi–Hubbard antiferromagnet, *Nature* 545(7655), 462–466 (2017).

[123] J. G. Bohnet et al., Quantum spin dynamics and entanglement generation with hundreds of trapped ions, *Science* 352(6291), 1297–1301 (2016).

[124] M. Rispoli et al., Quantum critical behaviour at the many-body localization transition, *Nature* 573(7774), 385–389 (2019).

[125] R. W. Cherng and E. Demler, Quantum noise analysis of spin systems realized with cold atoms, *New Journal of Physics* 9(1), 7 (2007).

[126] A. Lamacraft and P. Fendley, Order Parameter Statistics in the Critical Quantum Ising Chain, *Phys. Rev. Lett.* 100, 165706 (2008).

[127] S. P. Rath and W. Zwerger, Full counting statistics of the interference contrast from independent Bose–Einstein condensates, *Phys. Rev. A* 82, 053622 (2010).

[128] D. A. Ivanov and A. G. Abanov, Characterizing correlations with full counting statistics: classical Ising and quantum XY spin chains, *Physical Review E* 87, 022114 (2013).

[129] Y. Shi and I. Klich, Full counting statistics and the Edgeworth series for matrix product states, *Journal of Statistical Mechanics: Theory and Experiment* 2013(05), P05001 (2013).

[130] V. Eisler, Universality in the Full Counting Statistics of Trapped Fermions, *Phys. Rev. Lett.* 111, 080402 (2013).

[131] I. Klich, A note on the full counting statistics of paired fermions, *Journal of Statistical Mechanics: Theory and Experiment* 2014(11), P11006 (2014).

[132] M. Collura, F. H. L. Essler, and S. Groha, Full counting statistics in the spin-1/2 Heisenberg XXZ chain, *Journal of Physics A: Mathematical and Theoretical* 50(41), 414002 (2017).

[133] J.-M. Stéphan and F. Pollmann, Full counting statistics in the Haldane-Shastry chain, *Physical Review B* 95(3), 035119 (2017).

[134] K. Najafi and M. A. Rajabpour, Full counting statistics of the subsystem energy for free fermions and quantum spin chains, *Physical Review B* 96, 235109 (2017).

[135] S. Humeniuk and H. P. Büchler, Full Counting Statistics for Interacting Fermions with Determinantal Quantum Monte Carlo Simulations, *Phys. Rev. Lett.* 119, 236401 (2017).

[136] A. Bastianello, L. Piroli, and P. Calabrese, Exact local correlations and full counting statistics for arbitrary states of the one-dimensional interacting Bose gas, *Phys. Rev. Lett.* 120(19), 190601 (2018).

[137] M. Arzamasovs and D. M. Gangardt, Full Counting Statistics and Large Deviations in a Thermal 1D Bose Gas, *Phys. Rev. Lett.* 122, 120401 (2019).

[138] P. Calabrese et al., Full counting statistics in the gapped XXZ spin chain, *Europhysics Letters* 129(6), 60007 (2020).

[139] F. Ares, M. A. Rajabpour, and J. Viti, Exact full counting statistics for the staggered magnetization and the domain walls in the XY spin chain, *Phys. Rev. E* 103, 042107 (2021).

[140] L. Capizzi, S. Murciano, and P. Calabrese, Full counting statistics and symmetry resolved entanglement for free conformal theories with interface defects, *Journal of Statistical Mechanics: Theory and Experiment* 2023(7), 073102 (2023).

[141] K.-L. Cai and M. Cheng, Universal contributions to charge fluctuations in spin chains at finite temperature, *Phys. Rev. B* 111, 205104 (2025).

[142] V. Gritsev et al., Full quantum distribution of contrast in interference experiments between interacting one-dimensional Bose liquids, *Nature Physics* 2(10), 705–709 (2006).

[143] A. Imambekov, V. Gritsev, and E. Demler, *Fundamental noise in matter interferometers*, 2007.

[144] V. Eisler and Z. Rácz, Full counting statistics in a propagating quantum front and random matrix spectra, *Phys. Rev. Lett.* 110(6), 060602 (2013).

[145] S. Groha, F. H. L. Essler, and P. Calabrese, Full counting statistics in the transverse field Ising chain, *SciPost Phys.* 4, 043 (2018).

[146] N. Ranabhat and M. Collura, Dynamics of the order parameter statistics in the long range Ising model, *SciPost Phys.* 12, 126 (2022).

[147] I. Lovas et al., Full counting statistics of time-of-flight images, *Physical Review A* 95(5), 053621 (2017).

[148] M. Collura, Relaxation of the order-parameter statistics in the Ising quantum chain, *SciPost Phys.* 7, 072 (2019).

[149] M. Collura and F. H. L. Essler, How order melts after quantum quenches, *Phys. Rev. B* 101, 041110 (2020).

[150] O. Gamayun, O. Lychkovskiy, and J.-S. Caux, Fredholm determinants, full counting statistics and Loschmidt echo for domain wall profiles in one-dimensional free fermionic chains, *SciPost Phys.* 8, 036 (2020).

[151] B. Bertini et al., Nonequilibrium Full Counting Statistics and Symmetry-Resolved Entanglement from Space-Time Duality, *Phys. Rev. Lett.* 131, 140401 (2023).

[152] D. X. Horváth and C. Rylands, Full counting statistics of charge in quenched quantum gases, *Phys. Rev. A* 109, 043302 (2024).

[153] B. Bertini et al., Dynamics of charge fluctuations from asymmetric initial states, *Phys. Rev. B* 109, 184312 (2024).

[154] D. X. Horvath, B. Doyon, and P. Ruggiero, Full counting statistics after quantum quenches as hydrodynamic fluctuations, *arXiv preprint arXiv:2411.14406* (2024).

[155] N. Ranabhat and M. Collura, Thermalization of long range Ising model in different dynamical regimes: A full counting statistics approach, *SciPost Phys. Core* 7, 017 (2024).

[156] T. Ishiyama, K. Fujimoto, and T. Sasamoto, Exact Current Fluctuations in a Tight-Binding Chain with Dephasing Noise, *arXiv preprint arXiv:2504.06989* (2025).

[157] D. X. Horvath, B. Doyon, and P. Ruggiero, A Hydrodynamic Theory for Non-Equilibrium Full Counting Statistics in One-Dimensional Quantum Systems, *arXiv preprint arXiv:2507.05954* (2025).

[158] J. F. Wienand et al., Emergence of fluctuating hydrodynamics in chaotic quantum systems, *Nature Physics* 20(11), 1732–1737 (2024).

[159] E. Rosenberg et al., Dynamics of magnetization at infinite temperature in a Heisenberg spin chain, *Science* 384(6691), 48–53 (2024).

[160] L. K. Joshi et al., Measuring full counting statistics in a quantum simulator, *arXiv preprint arXiv:2501.14424* (2025).

[161] A. Serafini, *Quantum continuous variables: a primer of theoretical methods*, CRC press, 2017.

[162] C. Weedbrook et al., Gaussian quantum information, *Rev. Mod. Phys.* 84, 621–669 (2012).

[163] T. Shi, E. Demler, and J. Ignacio Cirac, Variational study of fermionic and bosonic systems with non-Gaussian states: Theory and applications, *Annals of Physics* 390, 245–302 (2018).

[164] R. Kruse et al., Detailed study of Gaussian boson sampling, *Phys. Rev. A* 100, 032326 (2019).

[165] G.-S. Paraoanu and H. Scutaru, Fidelity for multimode thermal squeezed states, *Phys. Rev. A* 61, 022306 (2000).

[166] P. Marian and T. A. Marian, Uhlmann fidelity between two-mode Gaussian states, *Phys. Rev. A* 86, 022340 (2012).

[167] V. Link and W. T. Strunz, Geometry of Gaussian quantum states, *Journal of Physics A: Mathematical and Theoretical* 48(27), 275301 (2015).

[168] M. Takahashi, Modified spin-wave theory of a square-lattice antiferromagnet, *Phys. Rev. B* 40, 2494–2501 (1989).

[169] S.-J. Chang, Quantum fluctuations in a φ^4 field theory. I. Stability of the vacuum, *Phys. Rev. D* 12, 1071–1088 (1975).

[170] S. Sotiriadis and J. Cardy, Quantum quench in interacting field theory: a self-consistent approximation, *Phys. Rev. B* 81, 134305 (2010).

[171] D. Boyanovsky et al., Evolution of inhomogeneous condensates: self-consistent variational approach, *Phys. Rev. D* 58, 025007 (1998).

[172] Y. D. van Nieuwkerk and F. H. L. Essler, Self-consistent time-dependent harmonic approximation for the sine-Gordon model out of equilibrium, *Journal of Statistical Mechanics: Theory and Experiment* 2019(8), 084012 (2019).

[173] Y. D. van Nieuwkerk and F. H. L. Essler, On the low-energy description for tunnel-coupled one-dimensional Bose gases, *SciPost Physics* 9(2) (2020).

[174] Y. D. van Nieuwkerk, J. Schmiedmayer, and F. H. L. Essler, Josephson oscillations in split one-dimensional Bose gases, *SciPost Physics* 10(4) (2021).

[175] M. Moeckel and S. Kehrein, Crossover from adiabatic to sudden interaction quenches in the Hubbard model: prethermalization and non-equilibrium dynamics, *New Journal of Physics* 12(5), 055016 (2010).

[176] M. Moeckel and S. Kehrein, Real-time evolution for weak interaction quenches in quantum systems, *Annals of Physics* 324(10), 2146–2178 (2009).

[177] F. H. L. Essler et al., Quench dynamics in a model with tuneable integrability breaking, *Physical Review B* 89(16), 165104 (2014).

[178] J. Robertson, R. Senese, and F. H. L. Essler, A simple theory for quantum quenches in the ANNNI model, *SciPost Physics* 15(1), 032 (2023).

[179] J. H. Robertson, R. Senese, and F. H. L. Essler, Decay of long-lived oscillations after quantum quenches in gapped interacting quantum systems, *Phys. Rev. A* 109, 032208 (2024).

[180] E. Lieb, T. Schultz, and D. Mattis, Two soluble models of an antiferromagnetic chain, *Annals of Physics* 16(3), 407–466 (1961).

[181] W. Marshall, Antiferromagnetism, *Proceedings of the Royal Society of London. Series A. Mathematical and Physical Sciences* 232(1188), 48–68 (1955).

[182] M. B. Hastings, Lieb-Schultz-Mattis in higher dimensions, *Phys. Rev. B* 69, 104431 (2004).

[183] B. Nachtergaele and R. Sims, A Multi-Dimensional Lieb-Schultz-Mattis Theorem, *Communications in Mathematical Physics* 276, 437 (2007).

[184] F. Haldane, Continuum dynamics of the 1-D Heisenberg antiferromagnet: Identification with the O(3) nonlinear sigma model, *Physics Letters A* 93(9), 464–468 (1983).

[185] F. D. M. Haldane, Nonlinear Field Theory of Large-Spin Heisenberg Antiferromagnets: Semiclassically Quantized Solitons of the One-Dimensional Easy-Axis Néel State, *Phys. Rev. Lett.* 50, 1153–1156 (1983).

[186] I. Affleck, Quantum spin chains and the Haldane gap, *Journal of Physics: Condensed Matter* 1(19), 3047 (1989).

[187] E. Manousakis, The spin-1/2 Heisenberg antiferromagnet on a square lattice and its application to the cuprous oxides, *Rev. Mod. Phys.* 63, 1–62 (1991).

[188] M. E. Lines, Green Functions in the Theory of Antiferromagnetism, *Phys. Rev.* 135, A1336–A1346 (1964).

[189] L. Bang-Gui, Magnetic properties of a quasi-two-dimensional Heisenberg antiferromagnetic model, *Journal of Physics: Condensed Matter* 2(27), 6007 (1990).

[190] V. Irkhin, A. Katanin, and M. Katsnelson, Short-range order above TN in quasi-two-dimensional Heisenberg antiferromagnets, *Physics Letters A* 157(4), 295–298 (1991).

[191] A. Barabanov and E. Zhasinas, The spherical-symmetric approach for the 3D S = 1/2 Heisenberg antiferromagnet, *Physics Letters A* 193(2), 191–194 (1994).

[192] A. W. Sandvik, Critical Temperature and the Transition from Quantum to Classical Order Parameter Fluctuations in the Three-Dimensional Heisenberg Antiferromagnet, *Phys. Rev. Lett.* 80, 5196–5199 (1998).

[193] T. Holstein and H. Primakoff, Field Dependence of the Intrinsic Domain Magnetization of a Ferromagnet, *Phys. Rev.* 58, 1098–1113 (1940).

[194] R. Kubo, The Spin-Wave Theory of Antiferromagnetics, *Phys. Rev.* 87, 568–580 (1952).

[195] Z. Weihong, J. Oitmaa, and C. J. Hamer, Square-lattice Heisenberg antiferromagnet at T=0, *Phys. Rev. B* 43, 8321–8330 (1991).

[196] P. W. Anderson, An Approximate Quantum Theory of the Antiferromagnetic Ground State, *Phys. Rev.* 86, 694–701 (1952).

[197] A. Singh and Z. Te šanovi ć, Quantum spin fluctuations in an itinerant antiferromagnet, *Phys. Rev. B* 41, 11457–11465 (1990).

[198] B.-G. Liu, A nonlinear spin-wave theory of quasi-2D quantum Heisenberg antiferromagnets, *Journal of Physics: Condensed Matter* 4(43), 8339 (1992).

[199] J. An, C.-D. Gong, and H.-Q. Lin, Softened spin-wave dispersion and sublattice magnetization at finite temperature for a three-dimensional anisotropic Heisenberg antiferromagnet, *Journal of Physics: Condensed Matter* 13(1), 115 (2001).

[200] M. Vogl et al., Resummation of the Holstein-Primakoff expansion and differential equation approach to operator square roots, *Phys. Rev. Res.* 2, 043243 (2020).

[201] J. König and A. Hucht, Newton series expansion of bosonic operator functions, *SciPost Phys.* 10, 007 (2021).

[202] A. Lerose et al., Chaotic Dynamical Ferromagnetic Phase Induced by Nonequilibrium Quantum Fluctuations, *Phys. Rev. Lett.* 120, 130603 (2018).

[203] A. Lerose et al., Impact of nonequilibrium fluctuations on prethermal dynamical phase transitions in long-range interacting spin chains, *Phys. Rev. B* 99, 045128 (2019).

[204] S. Pappalardi et al., Scrambling and entanglement spreading in long-range spin chains, *Phys. Rev. B* 98, 134303 (2018).

[205] A. Lerose and S. Pappalardi, Origin of the slow growth of entanglement entropy in long-range interacting spin systems, *Phys. Rev. Res.* 2, 012041 (2020).

[206] A. Polkovnikov et al., Colloquium: Nonequilibrium dynamics of closed interacting quantum systems, *Rev. Mod. Phys.* 83, 863–883 (2011).

[207] D. P. Arovas and A. Auerbach, Functional integral theories of low-dimensional quantum Heisenberg models, *Phys. Rev. B* 38, 316–332 (1988).

[208] M. Takahashi, Quantum Heisenberg Ferromagnets in One and Two Dimensions at Low Temperature, *Progress of Theoretical Physics Supplement* 87, 233–246 (1986).

[209] D. Yoshioka, Boson Mean Field Theory of the Square Lattice Heisenberg Model, *Journal of the Physical Society of Japan* 58(10), 3733–3745 (1989).

[210] S. Chakravarty, B. I. Halperin, and D. R. Nelson, Two-dimensional quantum Heisenberg antiferromagnet at low temperatures, *Phys. Rev. B* 39, 2344–2371 (1989).

[211] S. Maleev, Scattering of slow neutrons in ferromagnets, *Sov. Phys. JETP* 6(4), 776 (1958).

[212] F. J. Dyson, General Theory of Spin-Wave Interactions, *Phys. Rev.* 102, 1217–1230 (1956).

[213] A. Auerbach, *Interacting electrons and quantum magnetism*, Springer Science & Business Media, 1998.

[214] A. B. Harris et al., Dynamics of an Antiferromagnet at Low Temperatures: Spin-Wave Damping and Hydrodynamics, *Phys. Rev. B* 3, 961–1024 (1971).

[215] M. Moeckel and S. Kehrein, Interaction quench in the Hubbard model, *Phys. Rev. Lett.* 100(17), 175702 (2008).

[216] Z.-Y. Wang, S. Takayoshi, and M. Nakamura, Spin-chain description of fractional quantum Hall states in the Jain series, *Phys. Rev. B* 86, 155104 (2012).

[217] E. J. Bergholtz, M. Nakamura, and J. Suorsa, Effective spin chains for fractional quantum Hall states, *Physica E: Low-dimensional Systems and Nanostructures* 43(3), 755–760 (2011).

[218] W. Morong et al., Observation of Stark many-body localization without disorder, *Nature* 599(7885), 393–398 (2021).

[219] E. van Nieuwenburg, Y. Baum, and G. Refael, From Bloch oscillations to many-body localization in clean interacting systems, *Proceedings of the National Academy of Sciences* 116(19), 9269–9274 (2019).

[220] S. Scherg et al., Observing non-ergodicity due to kinetic constraints in tilted Fermi-Hubbard chains, *Nature Communications* 12(1), 4490 (2021).

[221] T. Kohlert et al., Exploring the Regime of Fragmentation in Strongly Tilted Fermi-Hubbard Chains, *Phys. Rev. Lett.* 130, 010201 (2023).

[222] Q. Guo et al., Stark Many-Body Localization on a Superconducting Quantum Processor, *Phys. Rev. Lett.* 127, 240502 (2021).

[223] Y.-Y. Wang et al., Exploring Hilbert-Space Fragmentation on a Superconducting Processor, *arXiv preprint arXiv:2403.09095* (2024).

[224] S. Ghosh et al., Destructive Interference induced constraints in Floquet systems, *arXiv preprint arXiv:2508.18368* (2025).

[225] A. Morningstar, V. Khemani, and D. A. Huse, Kinetically constrained freezing transition in a dipole-conserving system, *Phys. Rev. B* 101, 214205 (2020).

[226] C. Pozderac et al., Exact solution for the filling-induced thermalization transition in a one-dimensional fracton system, *Phys. Rev. B* 107, 045137 (2023).

[227] C. Wang and Z.-C. Yang, Freezing transition in the particle-conserving East model, *Phys. Rev. B* 108, 144308 (2023).

[228] O. Hart and R. Nandkishore, Hilbert space shattering and dynamical freezing in the quantum Ising model, *Phys. Rev. B* 106, 214426 (2022).

[229] S. Melczer, G. Panova, and R. Pemantle, Counting Partitions inside a Rectangle, *SIAM Journal on Discrete Mathematics* 34(4), 2388–2410 (2020).

[230] Z.-C. Yang et al., Hilbert-Space Fragmentation from Strict Confinement, *Phys. Rev. Lett.* 124, 207602 (2020).

[231] D. N. Page, Average entropy of a subsystem, *Phys. Rev. Lett.* 71, 1291–1294 (1993).

[232] S. Sen, Average Entropy of a Quantum Subsystem, *Phys. Rev. Lett.* 77, 1–3 (1996).

[233] E. Bianchi and P. Donà, Typical entanglement entropy in the presence of a center: Page curve and its variance, *Phys. Rev. D* 100, 105010 (2019).

[234] M. Fishman, S. R. White, and E. M. Stoudenmire, The ITensor Software Library for Tensor Network Calculations, *SciPost Phys. Codebases* 4 (2022).

[235] N. S. Srivatsa et al., Mobility edges through inverted quantum many-body scarring, *Phys. Rev. B* 108, L100202 (2023).

[236] Q. Chen and Z. Zhu, Inverting multiple quantum many-body scars via disorder, *Phys. Rev. B* 109, 014212 (2024).

[237] N. S. Srivatsa, R. Moessner, and A. E. B. Nielsen, Many-Body Delocalization via Emergent Symmetry, *Phys. Rev. Lett.* 125, 240401 (2020).

[238] M. Iversen, N. S. Srivatsa, and A. E. B. Nielsen, Escaping many-body localization in an exact eigenstate, *Phys. Rev. B* 106, 214201 (2022).

[239] E. H. Lieb and W. Liniger, Exact Analysis of an Interacting Bose Gas. I. The General Solution and the Ground State, *Phys. Rev.* 130, 1605–1616 (1963).

[240] E. H. Lieb, Exact Analysis of an Interacting Bose Gas. II. The Excitation Spectrum, *Phys. Rev.* 130, 1616–1624 (1963).

[241] G. Carleo et al., Unitary Dynamics of Strongly Interacting Bose Gases with the Time-Dependent Variational Monte Carlo Method in Continuous Space, *Phys. Rev. X* 7, 031026 (2017).

[242] T. Kinoshita, T. Wenger, and D. S. Weiss, Observation of a One-Dimensional Tonks-Girardeau Gas, *Science* 305(5687), 1125–1128 (2004).

[243] B. Paredes et al., Tonks–Girardeau gas of ultracold atoms in an optical lattice, *Nature* 429(6989), 277–281 (2004).

[244] T. Kinoshita, T. Wenger, and D. S. Weiss, A quantum Newton's cradle, *Nature* 440(7086), 900–903 (2006).

[245] M. A. Cazalilla et al., One dimensional bosons: From condensed matter systems to ultracold gases, *Rev. Mod. Phys.* 83, 1405–1466 (2011).

[246] J.-S. Caux and P. Calabrese, Dynamical density-density correlations in the one-dimensional Bose gas, *Phys. Rev. A* 74, 031605 (2006).

[247] J. Brand and A. Y. Cherny, Dynamic structure factor of the one-dimensional Bose gas near the Tonks-Girardeau limit, *Phys. Rev. A* 72, 033619 (2005).

[248] A. Y. Cherny and J. Brand, Polarizability and dynamic structure factor of the one-dimensional Bose gas near the Tonks-Girardeau limit at finite temperatures, *Phys. Rev. A* 73, 023612 (2006).

[249] J.-S. Caux, P. Calabrese, and N. A. Slavnov, One-particle dynamical correlations in the one-dimensional Bose gas, *Journal of Statistical Mechanics: Theory and Experiment* 2007(01), P01008 (2007).

[250] N. Kitanine et al., Form factor approach to dynamical correlation functions in critical models, *Journal of Statistical Mechanics: Theory and Experiment* 2012(09), P09001 (2012).

[251] M. Panfil and J.-S. Caux, Finite-temperature correlations in the Lieb-Liniger one-dimensional Bose gas, *Phys. Rev. A* 89, 033605 (2014).

[252] N. Fabbri et al., Dynamical structure factor of one-dimensional Bose gases: Experimental signatures of beyond-Luttinger-liquid physics, *Phys. Rev. A* 91, 043617 (2015).

[253] F. Meinert et al., Probing the Excitations of a Lieb-Liniger Gas from Weak to Strong Coupling, *Phys. Rev. Lett.* 115, 085301 (2015).

[254] K. K. Kozlowski, Large-Distance and Long-Time Asymptotic Behavior of the Reduced Density Matrix in the Non-Linear Schrödinger Model, *Annales Henri Poincaré* 16(2), 437–534 (2015).

[255] J. D. Nardis and M. Panfil, Exact correlations in the Lieb-Liniger model and detailed balance out-of-equilibrium, *SciPost Phys.* 1, 015 (2016).

[256] B. Doyon and H. Spohn, Drude Weight for the Lieb-Liniger Bose Gas, *SciPost Phys.* 3, 039 (2017).

[257] B. Doyon, Exact large-scale correlations in integrable systems out of equilibrium, *SciPost Phys.* 5, 054 (2018).

[258] E. Granet and F. H. L. Essler, A systematic $1/c$-expansion of form factor sums for dynamical correlations in the Lieb-Liniger model, *SciPost Phys.* 9, 082 (2020).

[259] E. Granet, Low-density limit of dynamical correlations in the Lieb–Liniger model, *Journal of Physics A: Mathematical and Theoretical* 54(15), 154001 (2021).

[260] S. Cheng et al., One-body dynamical correlation function of the Lieb-Liniger model at finite temperature, *Phys. Rev. A* 111, L010802 (2025).

[261] R.-T. Li et al., Exact results of dynamical structure factor of Lieb–Liniger model, *Journal of Physics A: Mathematical and Theoretical* 56(33), 335204 (2023).

[262] V. Gritsev, T. Rostunov, and E. Demler, Exact methods in the analysis of the non-equilibrium dynamics of integrable models: application to the study of correlation functions for non-equilibrium 1D Bose gas, *Journal of Statistical Mechanics: Theory and Experiment* 2010(05), P05012 (2010).

[263] J. Mossel and J.-S. Caux, Exact time evolution of space- and time-dependent correlation functions after an interaction quench in the one-dimensional Bose gas, *New Journal of Physics* 14(7), 075006 (2012).

[264] J.-S. Caux and F. H. L. Essler, Time Evolution of Local Observables After Quenching to an Integrable Model, *Phys. Rev. Lett.* 110, 257203 (2013).

[265] M. Kormos et al., Interaction quenches in the one-dimensional Bose gas, *Phys. Rev. B* 88, 205131 (2013).

[266] J. De Nardis et al., Solution for an interaction quench in the Lieb-Liniger Bose gas, *Phys. Rev. A* 89, 033601 (2014).

[267] M. Kormos, M. Collura, and P. Calabrese, Analytic results for a quantum quench from free to hard-core one-dimensional bosons, *Phys. Rev. A* 89, 013609 (2014).

[268] J. De Nardis and M. Panfil, Density form factors of the 1D Bose gas for finite entropy states, *Journal of Statistical Mechanics: Theory and Experiment* 2015(2), P02019 (2015).

[269] J. D. Nardis, L. Piroli, and J.-S. Caux, Relaxation dynamics of local observables in integrable systems, *Journal of Physics A: Mathematical and Theoretical* 48(43), 43FT01 (2015).

[270] J. C. Zill et al., Relaxation dynamics of the Lieb-Liniger gas following an interaction quench: A coordinate Bethe-ansatz analysis, *Phys. Rev. A* 91, 023611 (2015).

[271] J. C. Zill et al., A coordinate Bethe ansatz approach to the calculation of equilibrium and nonequilibrium correlations of the one-dimensional Bose gas, *New Journal of Physics* 18(4), 045010 (2016).

[272] L. Piroli, P. Calabrese, and F. H. L. Essler, Multiparticle Bound-State Formation following a Quantum Quench to the One-Dimensional Bose Gas with Attractive Interactions, *Phys. Rev. Lett.* 116, 070408 (2016).

[273] I. Bouchoule, B. Doyon, and J. Dubail, The effect of atom losses on the distribution of rapidities in the one-dimensional Bose gas, *SciPost Phys.* 9, 044 (2020).

[274] I. Bouchoule and J. Dubail, Generalized hydrodynamics in the one-dimensional Bose gas: theory and experiments, *Journal of Statistical Mechanics: Theory and Experiment* 2022(1), 014003 (2022).

[275] N. J. Robinson, A. J. J. M. de Klerk, and J.-S. Caux, On computing non-equilibrium dynamics following a quench, *SciPost Phys.* 11, 104 (2021).

[276] E. Granet and F. H. L. Essler, Systematic strong coupling expansion for out-of-equilibrium dynamics in the Lieb-Liniger model, *SciPost Phys.* 11, 068 (2021).

[277] F. D. M. Haldane, 'Luttinger liquid theory' of one-dimensional quantum fluids. I. Properties of the Luttinger model and their extension to the general 1D interacting spinless Fermi gas, *Journal of Physics C: Solid State Physics* 14(19), 2585 (1981).

[278] F. D. M. Haldane, Effective Harmonic-Fluid Approach to Low-Energy Properties of One-Dimensional Quantum Fluids, *Phys. Rev. Lett.* 47, 1840–1843 (1981).

[279] T. Giamarchi, *Quantum physics in one dimension*, vol. 121, Clarendon press, 2003.

[280] C. Mora and Y. Castin, Extension of Bogoliubov theory to quasicondensates, *Phys. Rev. A* 67, 053615 (2003).

[281] Z. Ristivojevic, Excitation Spectrum of the Lieb-Liniger Model, *Phys. Rev. Lett.* 113, 015301 (2014).

[282] Z. Ristivojevic, Conjectures about the ground-state energy of the Lieb-Liniger model at weak repulsion, *Phys. Rev. B* 100, 081110 (2019).

[283] M. A. Cazalilla, Bosonizing one-dimensional cold atomic gases, *Journal of Physics B: Atomic, Molecular and Optical Physics* 37(7), S1 (2004).

[284] A. Imambekov, T. L. Schmidt, and L. I. Glazman, One-dimensional quantum liquids: Beyond the Luttinger liquid paradigm, *Rev. Mod. Phys.* 84, 1253–1306 (2012).

[285] A. Takács et al., One-body correlations and momentum distributions of trapped one-dimensional Bose gases at finite temperature, *Phys. Rev. A* 111, 033317 (2025).

[286] M. Olshanii and V. Dunjko, Short-Distance Correlation Properties of the Lieb-Liniger System and Momentum Distributions of Trapped One-Dimensional Atomic Gases, *Phys. Rev. Lett.* 91, 090401 (2003).

[287] O. I. Pâ ţu and A. Klümper, Correlation lengths of the repulsive one-dimensional Bose gas, *Phys. Rev. A* 88, 033623 (2013).

[288] J.-S. Caux, Correlation functions of integrable models: A description of the ABACUS algorithm, *Journal of Mathematical Physics* 50(9), 095214 (2009).

[289] A. J. J. M. de Klerk and J.-S. Caux, Improved Hilbert space exploration algorithms for finite temperature calculations, *SciPost Phys. Core* 6, 039 (2023).

[290] F. Buccheri, A. De Luca, and A. Scardicchio, Structure of typical states of a disordered Richardson model and many-body localization, *Phys. Rev. B* 84, 094203 (2011).

[291] A. Faribault and D. Schuricht, Integrability-Based Analysis of the Hyperfine-Interaction-Induced Decoherence in Quantum Dots, *Phys. Rev. Lett.* 110, 040405 (2013).

[292] A. Faribault and D. Schuricht, Spin decoherence due to a randomly fluctuating spin bath, *Phys. Rev. B* 88, 085323 (2013).

[293] S.-J. Gu, N. M. R. Peres, and Y.-Q. Li, Numerical and Monte Carlo Bethe ansatz method: 1D Heisenberg model, *The European Physical Journal B - Condensed Matter and Complex Systems* 48(2), 157–165 (2005).

[294] V. Alba, Simulating the generalized Gibbs ensemble (GGE): a Hilbert space Monte Carlo approach, *arXiv preprint arXiv:1507.06994* (2015).

[295] Z.-H. Zhang et al., Monte Carlo Bethe-ansatz approach for the study of the Lieb-Liniger model, *Phys. Rev. A* 109, 033320 (2024).

[296] G. De Rosi et al., Hole-induced anomaly in the thermodynamic behavior of a one-dimensional Bose gas, *SciPost Phys.* 13, 035 (2022).

[297] G. De Rosi et al., Correlation properties of a one-dimensional repulsive Bose gas at finite temperature, *New Journal of Physics* 25(4), 043002 (2023).

[298] C. N. Yang and C. P. Yang, Thermodynamics of a One-Dimensional System of Bosons with Repulsive Delta-Function Interaction, *Journal of Mathematical Physics* 10(7), 1115–1122 (1969).

[299] M. Girardeau, Relationship between Systems of Impenetrable Bosons and Fermions in One Dimension, *Journal of Mathematical Physics* 1(6), 516–523 (1960).

[300] D. B. Creamer, H. Thacker, and D. Wilkinson, Quantum Gel'fand-Levitan method as a generalized Jordan-Wigner transformation, *Physics Letters B* 92(1), 144–148 (1980).

[301] P. Jordan and E. Wigner, Über das Paulische Äquivalenzverbot, *Zeitschrift für Physik* 47(9), 631–651 (1928).

[302] S. Sachdev, *Quantum Phase Transitions*, 2nd ed., Cambridge University Press, 2011.

[303] A. L. Fetter and J. D. Walecka, *Quantum theory of many-particle systems*, Dover, 2003.

[304] T. Kojima, V. E. Korepin, and N. A. Slavnov, Determinant Representation for Dynamical Correlation Functions of the Quantum Nonlinear Schrödinger Equation, *Communications in Mathematical Physics* 188(3), 657–689 (1997).

[305] L. Piroli and P. Calabrese, Exact formulas for the form factors of local operators in the Lieb–Liniger model, *Journal of Physics A: Mathematical and Theoretical* 48(45), 454002 (2015).

[306] N. Metropolis et al., Equation of state calculations by fast computing machines, *The journal of chemical physics* 21(6), 1087–1092 (1953).

[307] W. K. Hastings, Monte Carlo sampling methods using Markov chains and their applications, *Biometrika* 57(1), 97–109 (1970).

[308] R. Y. Rubinstein and D. P. Kroese, *Simulation and the Monte Carlo method*, John Wiley & Sons, 2016.

[309] W. Gilks, S. Richardson, and D. Spiegelhalter, *Markov Chain Monte Carlo in Practice*, CRC Press, 1995.

[310] W. Feller, *An introduction to probability theory and its applications, Vol. 1*, John Wiley & Sons, 1957.

[311] V. E. Korepin and N. A. Slavnov, The time dependent correlation function of an Impenetrable Bose gas as a Fredholm minor.I, *Communications in Mathematical Physics* 129(1), 103–113 (1990).

[312] A. Lenard, Momentum Distribution in the Ground State of the One-Dimensional System of Impenetrable Bosons, *Journal of Mathematical Physics* 5(7), 930–943 (1964).

[313] A. Lenard, One-Dimensional Impenetrable Bosons in Thermal Equilibrium, *Journal of Mathematical Physics* 7(7), 1268–1272 (1966).

[314] O. I. Pâţu, V. E. Korepin, and D. V. Averin, One-dimensional impenetrable anyons in thermal equilibrium: II. Determinant representation for the dynamic correlation functions, *Journal of Physics A: Mathematical and Theoretical* 41(25), 255205 (2008).

[315] O. I. Pâţu, Exact spectral function of the Tonks-Girardeau gas at finite temperature, *Phys. Rev. A* 106, 053306 (2022).

[316] F. Bornemann, On the numerical evaluation of Fredholm determinants, *Mathematics of Computation* 79(270), 871–915 (2010).

[317] N. A. Slavnov, Calculation of scalar products of wave functions and form factors in the framework of the alcebraic Bethe ansatz, *Theoretical and Mathematical Physics* 79(2), 502–508 (1989).

[318] N. A. Slavnov, Nonequal-time current correlation function in a one-dimensional Bose gas, *Theoretical and Mathematical Physics* 82(3), 273–282 (1990).

[319] F. A. Smirnov, *Form factors in completely integrable models of quantum field theory*, vol. 14, World Scientific, 1992.

[320] M. Brenes, J. Goold, and M. Rigol, Low-frequency behavior of off-diagonal matrix elements in the integrable XXZ chain and in a locally perturbed quantum-chaotic XXZ chain, *Phys. Rev. B* 102, 075127 (2020).

[321] Y. Zhang, L. Vidmar, and M. Rigol, Statistical properties of the off-diagonal matrix elements of observables in eigenstates of integrable systems, *Phys. Rev. E* 106, 014132 (2022).

[322] T. LeBlond and M. Rigol, Eigenstate thermalization for observables that break Hamiltonian symmetries and its counterpart in interacting integrable systems, *Phys. Rev. E* 102, 062113 (2020).

[323] J. D. Nardis, D. Bernard, and B. Doyon, Diffusion in generalized hydrodynamics and quasiparticle scattering, *SciPost Phys.* 6, 049 (2019).

[324] E. H. Lieb and M. Loss, *Analysis*, vol. 14, American Mathematical Soc., 2001.